

DOTTORATO DI RICERCA IN GEOFISICA - XXVIII ciclo

Settore concorsuale di afferenza: 04/A4

Settore scientifico disciplinare: GEO/10

Ellipticity of Rayleigh waves and shallow crustal structure

Presentata da

Dott. ANDREA BERBELLINI

**Relatore:
Prof. ANDREA MORELLI**

**Coordinatrice didattica:
Prof.ssa NADIA PINARDI**

**Correlatore
Dott. ANTONELLO PIOMBO**

Esame finale anno 2016

Abstract

The axes ratio of elliptically-polarised Rayleigh-wave particle motion may provide information about shallow crustal structure beneath a seismographic station. This seldom-used parameter, often called ellipticity, or H/V, is different from the popular horizontal to vertical amplitude ratio of ambient seismic noise used for microzonation and similar studies, as we refer to deterministic measurements on Rayleigh-wave, fundamental-mode, wave groups originated by distant earthquakes. This measure is not influenced either by the source, or the propagation, and may yield robust information on crustal structure at shallower depth than group or phase velocity at the same frequency. Ellipticity is a potentially excellent tool to retrieve seismic parameters in sedimentary basins. We intend to examine feasibility and robustness of ellipticity measurements, and their application to retrieval of shallow crustal structure in northern Italy. The most striking structural element is the Po Plain sedimentary basin, but also sedimentary and crystalline rocks in the Northern Apennines and Alps. The Po Plain hides a complex system of active thrusts and folds that caused the 2012 seismic sequence. Our aim is to set a reliable system to measure and use H/V ratio to study the shallow crustal structure of this region. We implement and test automatic measurements for 95 seismic stations in northern Italy. Comparison between observations and predictions from a reference crustal model show substantial fit, particularly for $T \approx 38s$ data. Discrepancy for shorter periods suggests that slight modifications of the model are needed. Analysis of synthetic and real data indicates the possibility of prograde (inverse) particle motion, but the influence of ambient noise at the predicted, short, transition periods, makes such observations less reliable. We further invert ellipticity curves to retrieve v_S profiles beneath each station, and finally build a high-resolution crustal model of the Po Plain.

Contents

List of figures	13
Introduction	17
1 Po Plain region	21
1.1 Geological settings	21
1.2 Seismicity	22
1.3 Basin-effects	25
1.4 Seismological models	26
2 Rayleigh Waves Ellipticity	33
2.1 Introduction	33
2.2 Previous studies	35
2.3 Theoretical approach	38
3 Ellipticity of Rayleigh waves in basin and hard-rock sites in Northern Italy	41
3.1 Introduction	42
3.2 Data	45
3.3 Measurement scheme and results	49
3.4 Rayleigh wave ellipticity predictions from 3-D synthetics	60
3.5 Prograde Rayleigh wave motion	63
3.6 Discussion and Conclusions	69
4 Inversion for shear-wave velocity	73
4.1 Inversion technique	73
4.1.1 Forward problem	73
4.1.2 Cost function	74
4.2 Parameterisation	74
4.3 Synthetic test	75
4.4 Inversion results	76

4.5	Discussion and conclusions	83
5	Calibrating MAMBo with Rayleigh ellipticity: inversion with shape constraints	85
5.1	Introduction	85
5.2	MAMBo model	86
5.3	Inversion	87
5.4	Results	87
5.5	MAMBo-E	89
5.5.1	Vertical cross-sections	91
5.5.2	Depth sections	94
5.5.3	Ellipticity maps	95
5.5.4	Cross correlation	100
5.5.5	Phase and group velocities	100
5.6	Discussion	105
	References	109

List of Figures

1.1	Main structural elements of the Po Plain (Cavaliere, A., 2016, personal communication)	21
1.2	Historical seismicity in the Northern Italy from year 1000 to present day from the CPTI11 catalogue (http://emidius.mi.ingv.it/CPTI11/) and ISIDE catalogue (http://iside.rm.ingv.it). Historical seismicity before 1985 ($M > 5.0$) is plotted with squares. Instrumental seismicity from 1985 to present day ($M > 4.0$) is shown with circles. Instrumental earthquakes with magnitude $M > 5.5$ are shown with red stars.	23
1.3	Focal mechanisms available for events with magnitude $M_w > 5.0$ from 2006 to present day (Pondrelli et al 2002, Pondrelli et al 2004, Pondrelli et al 2006, Pondrelli et al 2007, Pondrelli et al 2011; Pondrelli et al 2015; RCMT database: http://www.bo.ingv.it/RCMT/)	24
1.4	a) EPcrust: sediment layer thickness (km). b) EPcrust: v_S of the sedimentary layer (km/s). c) EPcrust: v_S of the upper crust layer (km/s). d) EPcrust: v_S of the lower crust layer (km/s). (figures from Molinari & Morelli 2011)	26
1.5	Model from Molinari et al (2015b) at different depths.	29
1.6	Maps of the thickness of the MAMBo sedimentary layers from Molinari et al 2015a.	30
1.7	Displacement waveform simulation of the 29 May 2012 earthquake ($M_W 5.8$) using SpecFem3D. Red line: simulation using MAMBo. Black line: real data. Gray line: simulation using 1D model used for earthquake location. Amplitudes are normalized. (figure from Molinari et al. 2015a)	31
2.1	Sensitivity kernels for H/V ratio, group and phase velocity at 15 s and 45 s, as a function of v_S (solid line), v_P (dashed line) and density (dotted line) calculated by finite differences using a normal mode formalism for the 1-D Prem Earth model (Dziewonski & Anderson 1981).	34

2.2	Figure from Lin et al. 2012. (a) The 30 sec Rayleigh wave H/V ratio observed across the USArray. The triangles denote the stations used in the study. The 3 km sediment contours are also shown for several major sedimentary basins. WB: Williston Basin; PR: Powder River Basin; GR: Green River Basin; DB: Denver Basin. The depth sensitivities of 30 sec H/V ratio to v_S , density (ρ), and v_P/v_S perturbation are shown in the right. (b) Same as (a) but for 60 sec H/V ratio. (c, d) Same as (a) and (b) but for Rayleigh wave phase velocity.	37
3.1	Distribution of the events database used in this study. We used earthquake with epicentral distance between 10° and 140° from the stations and $m_W \geq 5.0$ occurred from January 2008 to December 2014.	45
3.2	Seismic stations used and corresponding number of measurements. The triangle size indicates the number of earthquake records available for each station and its color represents the percentage of successful measurements. Stations in the Po Plain sedimentary basin generally perform worse (see main text).	46
3.3	Frequency histogram of azimuthal angle deflections with respect to the theoretical great circle path. The maximum angle found is $\delta\alpha = -10.42^\circ$. Mean $\delta\alpha = -0.07^\circ$. Standard deviation = 2.15°	47
3.4	Measurement scheme shown for an earthquake at a distance of 60.3° and magnitude $M_W = 6.4$. We apply a bandpass filter to H and V components (a) and we shift the V component of 90° in advance (b). Then we calculate the cross-correlation between the two signals and the envelope (c). Subsequently we define a characteristic function as the product of cross-correlation and envelope (d). This function defines a time window that contains the fundamental mode of Rayleigh waves. We calculate ellipticity as the mean ratio between the V and the H envelope inside the time window (e).	49

3.5	Comparison between theoretical H/V values and measurements on synthetic seismograms, for 426 CMT solutions of real earthquakes. Theoretical ellipticity for the fundamental mode and first three overtones is represented by lines in different colour. Measurements from full synthetic seismograms calculated for PREM correspond to the black dots. Note that there are 426 dots for each period, mostly concentrated near the average, indicated by a red dot with error bars. The presence of overtones (with different ellipticity ratios) influences some measurements at shorter periods, but these appear as outliers well outside the $\pm\sigma$ error bars of the measurements. (Note that, for shorter periods, many dots overlap actually appearing as one, near the black curve, and control the value of the average shown with error brackets.)	51
3.6	(a): Mean misfit (for all periods) between ellipticity computed for an earthquake on synthetic seismograms, and theoretical value, as a function of hypocentral depth. (b): Synthetic seismograms and characteristic function for sample cases for hypocenters at 20 and 50 km depth in PREM. For depths larger than ~ 40 km the first overtone dominates and misleads the characteristic function. The misfit is calculated using: $m = \frac{\sum_{i=1}^N E_i^m - E_i^t }{\sum_{i=1}^N E_i^m }$, where N is the number of periods, E^m is the ellipticity measured on synthetics and E^t is the theoretical ellipticity calculated from eigenfunctions.	52
3.7	Histograms of ellipticity measurements for station GIMEL (a) and PRMA (b). Red vertical line indicates H/V median, also reported in the labels with the corresponding error. Errors are calculated using the percentiles corresponding to 15.9 and 84.1. Green dashed line is the ellipticity calculated on Prem reference model.	54
3.8	H/V measurements for stations GIMEL and PRMA as a function of period. Different colors show the density of dots. Dashed line is the theoretical ellipticity for the PREM model.	55
3.9	H/V ratios for different periods (shown in coloured solid circles) compared with theoretical values for model MAMBo (Molinari et al., 2015a) shown in the outer rings. Black outer ring means that ellipticity values are greater than 0.6, going up to 2.0 (FAEN station). The Pearson correlation coefficient between the observations and predictions is shown in the title of each diagram. The background shows thickness of the Pliocene sedimentary layer according to model MAMBo.	58

3.10	<p>H/V ratios for different periods (shown in coloured solid circles) compared with theoretical values for model MAMBo (Molinari et al., 2015a) shown in the outer rings. Black outer ring means that ellipticity values are greater than 0.6, going up to 2.0 (FAEN station). The Pearson correlation coefficient between the observations and predictions is shown in the title of each diagram. The background shows thickness of the Pliocene sedimentary layer according to model MAMBo.</p>	59
3.11	<p>Comparison between ellipticity measured on synthetics seismograms computed with a 3D model and ellipticity measured on synthetics computed with a 1D model built using the 3D profiles beneath each station. The bars are the errors associated with real measurements from each station. They give an estimate of the errors expected in real measurements (see figure 3.12). In the boxes the correlation coefficient between the two datasets is shown. This test shows that the local 1D approximation at the receiver can be used instead of a 3D model from source to receiver. The errors are always under the observed data errors.</p>	61
3.12	<p>Comparison between ellipticity of synthetic seismogram computed with 3D model and real data. x and y error bars are from real measurements. In the boxes there is the correlation coefficient. . . .</p>	62
3.13	<p>Theoretical ellipticity curve (solid black line) compared to ellipticity measured on synthetic seismogram (red dots) computed for model MAMBo at station CMPO (for location, see Figure 3.2). The big peak at $\sim 12.5s$ corresponds to the transition between retrograde motion (on the right) and prograde motion (on the left).</p>	63
3.14	<p>Map of the transition period between retrograde and prograde particle motion calculated on model MAMBo. In blank areas no transition is found for $T > 1$ s.</p>	65
3.15	<p>Histograms of ellipticity measurements for station CMPO (a) and BNI (b). Green histograms represent the measurements of retrograde particle motion. Red histograms represents the measurements of prograde motion.</p>	66

3.16	Measurement scheme for the March 11 2011 earthquake in the To- hoku region (Japan) (origin time: 05:46:23.00 UTC, $m_w = 9.0$) recorded at the station CMPO at a period of 4s (left) and 8s (right). (a) Full waveforms filtered with a narrow Butterworth-Bandpass fil- ter. Vertical component is plotted in red, horizontal (radial) compo- nent is plotted in black. (b) Zoom of the waveform. Vertical com- ponent is shifted in advance by a 90° phase. (c) Cross-correlation between the de-phased vertical component and horizontal compo- nent (solid line) and normalized envelope of horizontal times vertical components. Negative cross-correlation indicates a prograde polar- ization of rayleigh waves. (d) Characteristic function, defined as the product of envelope and cross-correlation. (e) H/V ratio between the envelopes of horizontal and vertical component.	67
3.17	Measurement scheme for the March 11 2011 earthquake in the To- hoku region (Japan) (origin time: 05:46:23.00 UTC, $m_w = 9.0$) recorded at the station CMPO at a period of 12s (left) and 16s (right). (a) Full waveforms filtered with a narrow Butterworth-Bandpass fil- ter. Vertical component is plotted in red, horizontal (radial) compo- nent is plotted in black. (b) Zoom of the waveform. Vertical com- ponent is shifted in advance by a 90° phase. (c) Cross-correlation between the de-phased vertical component and horizontal compo- nent (solid line) and normalized envelope of horizontal times vertical components. (d) Characteristic function, defined as the product of envelope and cross-correlation. (e) H/V ratio between the envelopes of horizontal and vertical component.	68
4.1	Synthetic test results. On the left: best v_S profile found (red line) compared with the true model used for the test (green line). Gray lines are all the model sampled during the inversion procedure. On the right: "observed data" obtained from the true model (black cir- cles), H/V calculated from the best model found (red line).	76
4.4	Triangles: v_S of the best model found for each station at different depths. Background: map of v_S from MAMBo model at the same depth.	78
4.5	Triangles: v_S of the best model found for each station at different depths. Background: map of v_S from MOL15 model at the same depth.	79

4.6	Triangles: v_S of the best model found for each station at different depths. Background: map of v_S from MOL15 model at the same depth.	80
4.2	Best model found for station CMPO (a) and BNI (b) compared with MAMBo model (blue line) and MOL15 (green). Gray models are all the models sampled with cost function up to 10 times the best one. .	81
4.3	Triangles: v_S of the best model found for each station at different depths. Background: map of v_S from MAMBo model at the same depth.	82
5.1	Picture from Molinari et al., 2015b. a) stratigraphic column of the Po Plain. b) Gradients of v_P and v_S relative to each stratigraphic layer.	86
5.2	Inversion results for v_S velocity for station CMPO. On the left: best model found (black line) compared to MAMBo (dashed line). In gray all the models sampled during the inversion process. On the right: observed data (black circles with error bars) compared to H/V synthetic values from MAMBo (dashed line) and H/V synthetic values from best model found (black solid line).	88
5.3	Inversion results for v_S velocity for station PRMA. On the left: best model found (black line) compared to MAMBo (dashed line). In gray all the models sampled during the inversion process. On the right: observed data (black circles with error bars) compared to H/V synthetic values from MAMBo (dashed line) and H/V synthetic values from best model found (black solid line).	89
5.4	Delta V_s between MAMBo-E and MAMBo for loose sediment layer (a), Quaternary layer (b), Pliocene layer (c), Oligo-Miocene layer (d), Mesozoic layer (e) and magnetic basement (f)	90
5.5	Section of model MAMBo (top) and MAMBo-E (bottom)	91
5.6	Section of model MAMBo (top) and MAMBo-E (bottom)	92
5.7	Section of model MAMBo (top) and MAMBo-E (bottom)	92
5.8	Section of model MAMBo (top) and MAMBo-E (bottom)	93
5.9	Section of model MAMBo (top) and MAMBo-E (bottom)	93
5.10	Shear-velocity at 2 km of depth for MAMBo (a) and MAMBo-E (b)	94
5.11	Shear-velocity at 4 km of depth for MAMBo (a) and MAMBo-E (b)	94
5.12	Shear-velocity at 6 km of depth for MAMBo (a) and MAMBo-E (b)	95
5.13	Shear-velocity at 8 km of depth for MAMBo (a) and MAMBo-E (b)	95
5.14	Ellipticity observed (circles) compared to expected values for MAMBo (a) and MAMBo-E (b) at 11s period.	96

5.15	Ellipticity observed (circles) compared to expected values for MAMBo (a) and MAMBo-E (b) at 16s period.	97
5.16	Ellipticity observed (circles) compared to expected values for MAMBo (a) and MAMBo-E (b) at 25s period.	98
5.17	Ellipticity observed (circles) compared to expected values for MAMBo (a) and MAMBo-E (b) at 38s period.	99
5.18	Comparison between observed ellipticity (y axes) and synthetic ellipticity calculated on MAMBo (on the left, x axis) and MAMBo-E (on the right, x axis) for 11 s (a), 16 s (b), 25 s(c), 38 s (d).	100
5.19	Phase velocity at period $T = 6$ s for model MAMBo (a) and MAMBo-E (b), group velocity for model MAMBo (c) and MAMBo-E (d). Black dots indicate the seismic stations used in this work.	101
5.20	Phase velocity at period $T = 10$ s for model MAMBo (a) and MAMBo-E (b), group velocity for model MAMBo (c) and MAMBo-E (d). Black dots indicate the seismic stations used in this work.	102
5.21	Phase velocity at period $T = 16$ s for model MAMBo (a) and MAMBo-E (b), group velocity for model MAMBo (c) and MAMBo-E (d). Black dots indicate the seismic stations used in this work.	103
5.22	Phase velocity at period $T = 24$ s for model MAMBo (a) and MAMBo-E (b), group velocity for model MAMBo (c) and MAMBo-E (d). Black dots indicate the seismic stations used in this work.	104

Acknowledgments

I would like to thank my supervisor Andrea Morelli for his guidance and patience. I learned a lot in the last three years and I owe it mostly to him.

A special thanks to Ana Ferreira for her support and help during my long visit to University College of London. It has been a fundamental period for my professional and human growth.

A great thanks also to Paolo and all of my family for their unconditional support and love.

Introduction

Po Plain corresponds to the largest sedimentary basin in Italy extending for approximately 400 *km* in a west-east direction from the western Alps to the Adriatic sea with a total surface of 47,820 *km*². It covers completely the foreland between the southern Alps and the northern Apennines and it corresponds to the drainage basin of the Po river, the largest and longest Italian river. Po Plain is one of the most populated areas of Italy with a total population of ≈ 20 millions of inhabitants and high density of industrial activities.

Despite its flat and homogeneous surface, the Po Plain hides a complex system of buried active thrusts and folds. In the southern part, parallel to the Apennines chain a system of Apennines outer folds runs from west to east. It is divided into three structures named the Monferrato Arc, the Emilia Arc and the Ferrara-Romagna arc, from west to east. These active tectonic structures are totally buried under a thick sedimentary Plio-Quaternary layer. In the northern part of the Plain other buried structures lie parallel to the Alpine chain from Milano to the Garda region. These outer arc are less complex and less tectonically active than the southern Apennines arcs.

These buried structure cause a relatively infrequent seismicity in the region compared to other zones in Italy, big enough for causing damages and impact in human activities. This region has been struck by an important seismic sequence in May/June 2012. The two mainshocks hit the Ferrara area on May 20 (M_W 6.1) and May 29 (M_W 5.9) and caused a total of 27 dead and ≈ 500 injuries, 20,000 evacuated and damages for millions of Euros. This earthquake had a larger impact on human activities than expected for several reasons.

This area has a particular high exposure because of the density of population and economic activities. Together with this factor, the sedimentary basin in the plain strongly influences the propagation of the waves. Basin effects include strong local amplification due to the known effect of seismic waves in a slow medium over a fast crystalline basement and because of the energy trapping phenomenon. These effects caused strong amplification in the terms of amplitude, longer duration of the signals and stronger excitation of surface waves, especially at longer periods.

Ground-shaking recordings exceeded the EC8 recommendation for building design for civil and building works (Dujardin et al 2016), causing more damages than expected. This sequence had also a great impact on the population awareness of the seismic risk. The latest seismic event was in the first decade of 1900 and the population did not have the feeling of living in a seismic active zone, although a number of significant earthquakes are known from historical catalogues. The 2012 sequence was the first seismic activity digitally recorded in this area and focused the attention of the Italian seismological community.

Before the 2012 events there was not a complete and detailed seismic model of the plain. The first comprehensive seismic model of the basin has been published by Molinari et al (2015a). This model, named MAMBo, has been built by the collection and critical interpretation of a number of geological information from water and hydrocarbon research, made in the last decades. MAMBo describes the layered structure of the sedimentary basin with a very high resolution ($0.01^\circ \times 0.01^\circ$). It has been used for ground-shaking simulation for the 2012 mainshocks and it showed a reliable better capability of reproducing the observed recordings. A wide and comprehensive validation of the model is still in progress. Geological studies used for building the MAMBo model gave very detailed information on layer interfaces and shape, but poor information on the seismic parameters inside each layer. Because of this, laboratory researches and empirical relations between seismic parameters have been used for making the model.

The aim of this work is to set up a reliable system to use a relatively little-known parameter of seismic surface waves (Rayleigh-wave polarisation characteristics), potentially very sensitive to the first km of crustal structure, and apply it to improve out knowledge of the shallow crustal structure of this region. We focus mainly on the first $\approx 10\text{-}15$ km of depth, where the largest portion of the sedimentary layers of the plain lies. This shallow section affects mostly the local seismic propagation and causes the strong basin effects. Traditional tomography techniques based on phase and group velocities are not very sensitive to the very shallowest part of the crust (i.e. $1 - 2$ km) so they are not reliable for this purpose. Our approach is based on the measurement and inversion of the ellipticity of Rayleigh waves.

Ellipticity (also named H/V ratio) is defined as the ratio between the amplitude of the horizontal component and the vertical component of a Rayleigh wave. It depends only on the seismic structure beneath the receiver station. It behaves in a similar way to phase and group velocity but it can be measured using only one station. For this reason it is a precise tool even in the case of poor or uneven coverage. Compared to phase and group velocities it has a very shallower sensitivity, an important property in sedimentary basins settings like this. Ellipticity can be measured using teleseisms from all over the world so it can be used virtually

everywhere, even where the local seismicity is small. These two properties makes ellipticity a interesting field of research and a tomographic technique based on it can be applied in many different cases, such as volcanic islands or low-coverage areas.

This thesis is organized in four parts. In the first chapter we give a general overview on the geological and tectonic setting of the Po Plain. We present also the historical and recent seismicity of the region with a particular attention to the May 2012 sequence, presenting also the main basin-effects affecting the area. We give also an overview on the seismic models available in the study area. In the second chapter we focus on the ellipticity of Rayleigh waves presenting the previous studies available on this research field and a theoretical approach to the problem. In the third chapter we present the original technique implemented in this work to measure ellipticity on real data recordings and the results of the measurements. We also present here the results of the study of the phenomenon of the inversion of polarity of Rayleigh waves in sedimentary basins. The last two chapters are devoted to the inversion of ellipticity curves using two different approaches. In the first we use a simple 4-layers parametrization for the crust. In the second we use the same complex parametrization of MAMBo to obtain an updated version of MAMBo. In both the cases we used a completely non-linear inversion technique. We used the Neighbourhood Algorithm, a fast, self-adaptative and efficient Monte Carlo method.

Chapter 1

Po Plain region

1.1 Geological settings

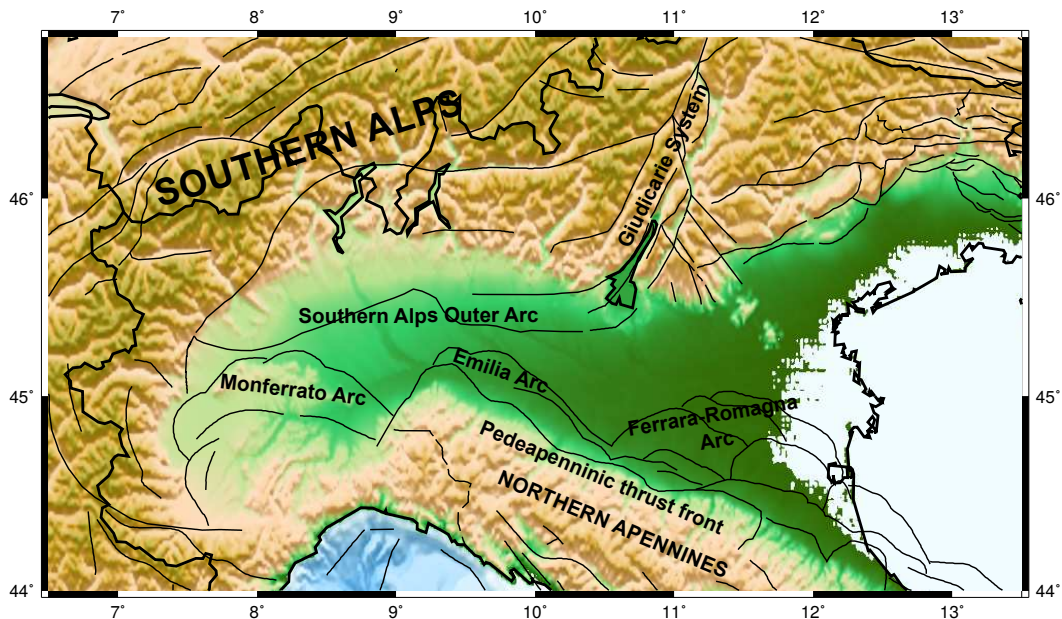


Figure 1.1: *Main structural elements of the Po Plain (Cavaliere, A., 2016, personal communication)*

Po Plain corresponds to the largest sedimentary basin in Northern Italy, extending for about 400 km from the western Alps to the Adriatic sea. It is surrounded by the Alps chain to the North and West, the Apennines chain to the south and Adriatic Sea to the east. It is crossed by the Po river, the longest and largest Italian river. From a geological point of view, the Po Plain corresponds to the foreland basin of the Alpine and Apennines fold-and-thrust belts, verging toward each other. The two chains originated by the convergence of African and European plates. This process started in the Cretaceous age and it caused the subduction of

both the plates (Carminati & Doglioni 2012) and it is still ongoing at a rate of a few mm per year. The Po Plain is composed by a superposition of Pliocene-Quaternary alluvial deposits, filling completely the foreland basin between the two chains. The sedimentary sequence has uneven thickness, from a few hundreds of meters over the buried anticlines to 8 km over the depocenters (e.g. in the Modena area). The thickness generally increases southward, toward the Northern Apennines mountain front. Sediments cover completely the outer arcs of the Northern Apennines, divided into three different structures: the Ferrara Arc, the Emilia Arc and the Monferrato Arc, respectively from east to west. Toward the rear of the Ferrara and Emilia Arcs lies the Pedepenninic Thrust Front (Boccaletti et al. 1985). This structure, at the southern edge of the plain, has been recently interpreted as a anticline forelimb of a deeper thrust ramp (Picotti & Pazzaglia 2008), not as an evidence of a shallow thrust, as thought before. This different interpretation could have a substantial difference in the modelisation of expected ground-shaking, a crucial point considering the high density of population living in this area. In the northern part of the Plain a simpler outer thrust front from the Southern Alps runs from the Milano area to the Garda region. On the East it is connected to the Giudicarie thrust system (Castellarin & Cantelli 2000, Massironi et al. 2006). (For a detailed and comprehensive description of the tectonics of the Plain see Vannoli et al. 2015)

The Po Plain is still seismically quite active, despite the aspect of a completely flat plain at the surface. GPS measurements showed that the convergence process of Europe and African plates that caused the raising of Alpine and Apennines chains is still ongoing. Serpelloni et al. (2007) measured the convergence with a rate of 3-8 mm/year with an increasing rate from west to east of 1-3mm/year. The Adriatic promontory is also rotating counter-clockwise with respect to the European plate. The rotation pole is located in the western Alps (Anderson and Jackson 1987, Weber et al. 2010) and the Po Plain represents the northern termination. Following this model the eastern part of the Plain is characterized by a compressional stress and borehole breakout measurements and focal mechanism in this area confirmed this model (Heidbach et al 2008, Montone et al 2012, Carafa & Barba 2013).

1.2 Seismicity

Convergence processes still active in this area causes a relatively moderate and infrequent seismicity (compared to other zones in Italy) in the plain and surrounding hills. On May-June 2012 a relatively strong seismic sequence hit this densely populated area. The first main shock took place on the 20th of May 2012 at 02:03:52UTC with a moment magnitude 6.1 (Regional Centroid Moment Tensor <http://www.bo.ingv.it/RCMT>). The second main shock hit nine days later, on the

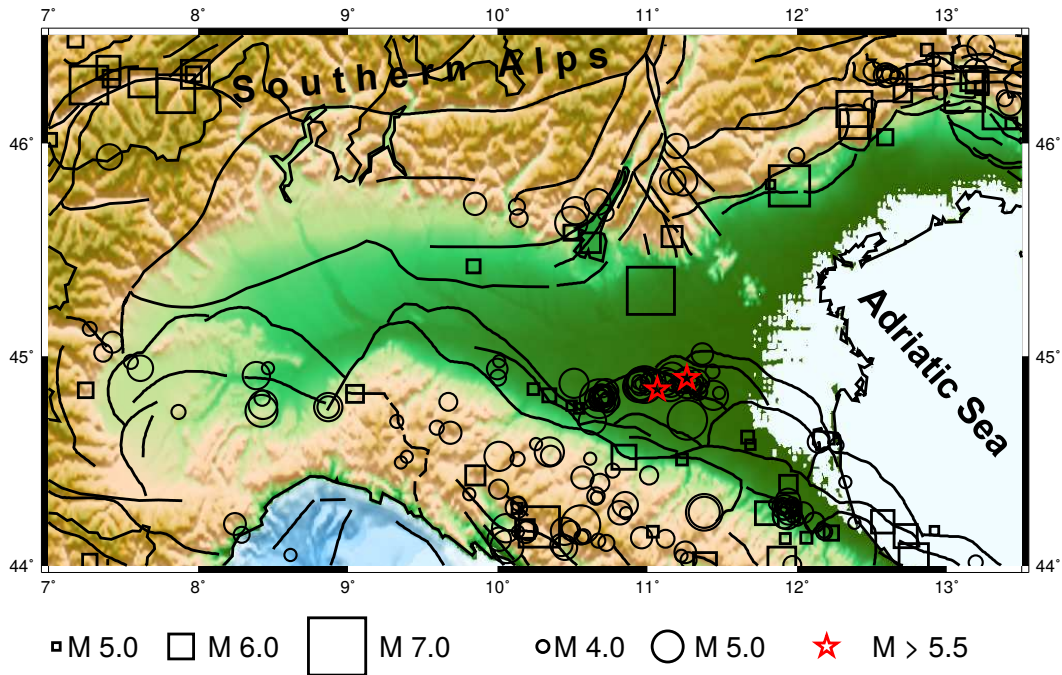


Figure 1.2: *Historical seismicity in the Northern Italy from year 1000 to present day from the CPTI11 catalogue (<http://emidius.mi.ingv.it/CPTI11/>) and ISIDE catalogue (<http://iside.rm.ingv.it>). Historical seismicity before 1985 ($M > 5.0$) is plotted with squares. Instrumental seismicity from 1985 to present day ($M > 4.0$) is shown with circles. Instrumental earthquakes with magnitude $M > 5.5$ are shown with red stars.*

29th of May 2012 at 07:00:03UTC (M_w 5.9, Saraò & Peruzza 2012). Both the mainshocks have been followed by a sequence of hundreds of smaller aftershocks, the strongest one with moment magnitude equal to 5.5. A total of 2100 aftershocks hit this area in the period from 29th of May 2012 and the 25th of June 2012 (Malagnini et al 2012). This seismic sequence caused unexpected heavy damages: 27 dead, ≈ 500 injuries, $\approx 20,000$ people evacuated and damages to historical buildings and industrial facilities for hundreds of millions of Euros. The hypocenters of the 2012 sequence (see fig.1.3) were located on the Ferrara-Romagna Arc, in particular in the central section of this buried active zone (Lai et al 2015, Luzi et al 2013, Dolce & Di Bucci 2014). A WSW-dipping low angle thrust faults sources have been indicated by the spatial distribution of aftershocks and focal mechanisms (Saraò & Peruzza 2012), with a seismogenetic zone ranging the depth between 5 and 10 km, above the basal detachment of the outer thrust fronts.

The 2012 sequence was the first in this area registered by digital recordings. In the history several other earthquakes hit this region (see fig. 1.2). The historical catalogues show that the seismicity is located principally along the foothills and the buried thrusts of the northern Apennines and southern Alps. The strongest

earthquake that hit the region, the M_w 6.7 with epicentre in the Verona area, was an exception to this setting. Northern Apennines thrusts show a higher seismicity than Southern Alps. Even if the distribution of the epicentres is not regular there is an increasing trend of historical seismicity eastward, from the Monferrato Arc to the Ferrara-Romagna Arc. The seismic activity is in general due to a compressional mechanism, with mainly thrust faults. Seismic sequences are often characterized by a mainshock followed by several similarly large aftershocks, a characteristic similar to all the Italian sequences. This may be due to the high complexity of Italian faults, where a mainshock often causes the rupture of the fault into a number of transverse smaller faults (Vannoli et al. 2015). This behaviour limits the length of the rupture of a fault, but it can cause the activation of several adjacent structures. Historical catalogues also record possibly deeper seismicity, below the approximately 15 km depth typical of earthquakes located in the active arcs. The 1909 earthquake, M_w 5.5, that hit the *Bassa Padana* has been felt in a wide area of 180,000 km^2 , with also spread damages and injuries. This suggests that the hypocentre of this event may have been ≈ 40 km deep (Faccioli 2013). More recently a couple of lower-crustal earthquakes have been recorded in the Reggio Emilia area (25th January 2012, M_L 5.0, depth 29.0 km) and Parma area (27th January 2012, M_L 5.2, depth 72.4 km).

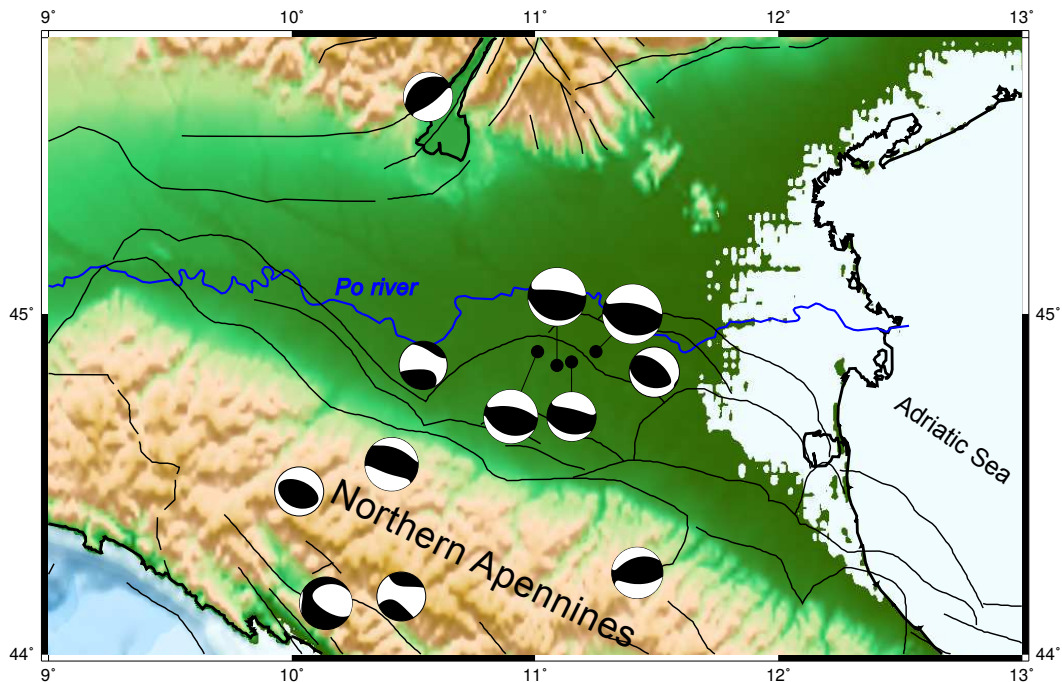


Figure 1.3: Focal mechanisms available for events with magnitude $M_w > 5.0$ from 2006 to present day (Pondrelli et al 2002, Pondrelli et al 2004, Pondrelli et al 2006, Pondrelli et al 2007, Pondrelli et al 2011; Pondrelli et al 2015; RCMT database: <http://www.bo.ingv.it/RCMT/>)

1.3 Basin-effects

Sedimentary basins often have strong effects on seismic wave propagation and ground shaking. Basin effects have been studied widely in the past, from the 19th September 1985 Mexico City earthquake (Bard et al 1998) to the 4th September 2010 Darfield earthquake in New Zealand (Bradley 2012). The long list of studies on basin effects on seismic wave propagation include those on the Los Angeles basin (Aagaard et al 2008), the Kanto basin (Koketsu & Kikuchi, 2000; Dhakal & Yamanaka, 2013), the Osaka basin (Kagawa et al., 2004) and the Grenoble basin (Stupazzini et al., 2009; Chaljub et al., 2010) The 2012 seismic sequence, despite the relatively small magnitude (M_W 6.1 and M_W 5.9), caused unexpected damages in a large area in the middle of the plain. Seismic records in some areas exceeded the EC8 recommendation for building design for civil and building works (Dujardin et al. 2016). Bragato et al. (2011) and Massa et al. (2012) showed that the ground motion equations underestimated the actual ground shaking by a factor of 2 or more. This effect is particularly evident for longer periods, i.e. $T > 10s$.

Recently Dujardin et al. (2016) simulated the basin effect in the 2012 Emilia earthquake using the empirical Green's function simulation (EGF) technique to reproduce the recorded seismograms. This technique reproduced with a good agreement seismic signals (Seismograms, Fourier spectra, PGA, PGV, duration, Stockwell transform) at an epicentral distance ranging between 5 and 160 km. Long-period seismic waves in sedimentary basins are mainly controlled by surface waves. Abraham et al. (2015) showed that in this particular setting Rayleigh waves are more excited, even if the seismic source is located inside the basin and the source-receiver distance is relatively small. Rayleigh waves are more dispersive than Love waves, with a clear separation of waves in the frequency domain. This phenomenon is due to the geometrical configuration of the basin that causes internal reflections, scattering and energy trapping. Waves dispersion of Rayleigh waves causes also a significant increasing of signal duration that increases the potential for damages to structures (Bommer & Martinez-Perreira 1999 and Bommer et al., 2009). Liquefaction effects of the soils have been recorded in large areas of the Po Plain (Emergeo working group, 2013). These effects increased the impact of the earthquake on the buildings and they were amplified by the long duration of ground-shaking and by long-periods signals. Summarizing, the effects of the basin on seismic waves propagation are:

- 1 Stronger generation of surface waves
- 2 Surface wave amplification
- 3 Liquefaction phenomena

All these effects highlighted the importance of a detailed knowledge of the basin seismic structure to better estimate the local effects of earthquakes to buildings and human activities.

1.4 Seismological models

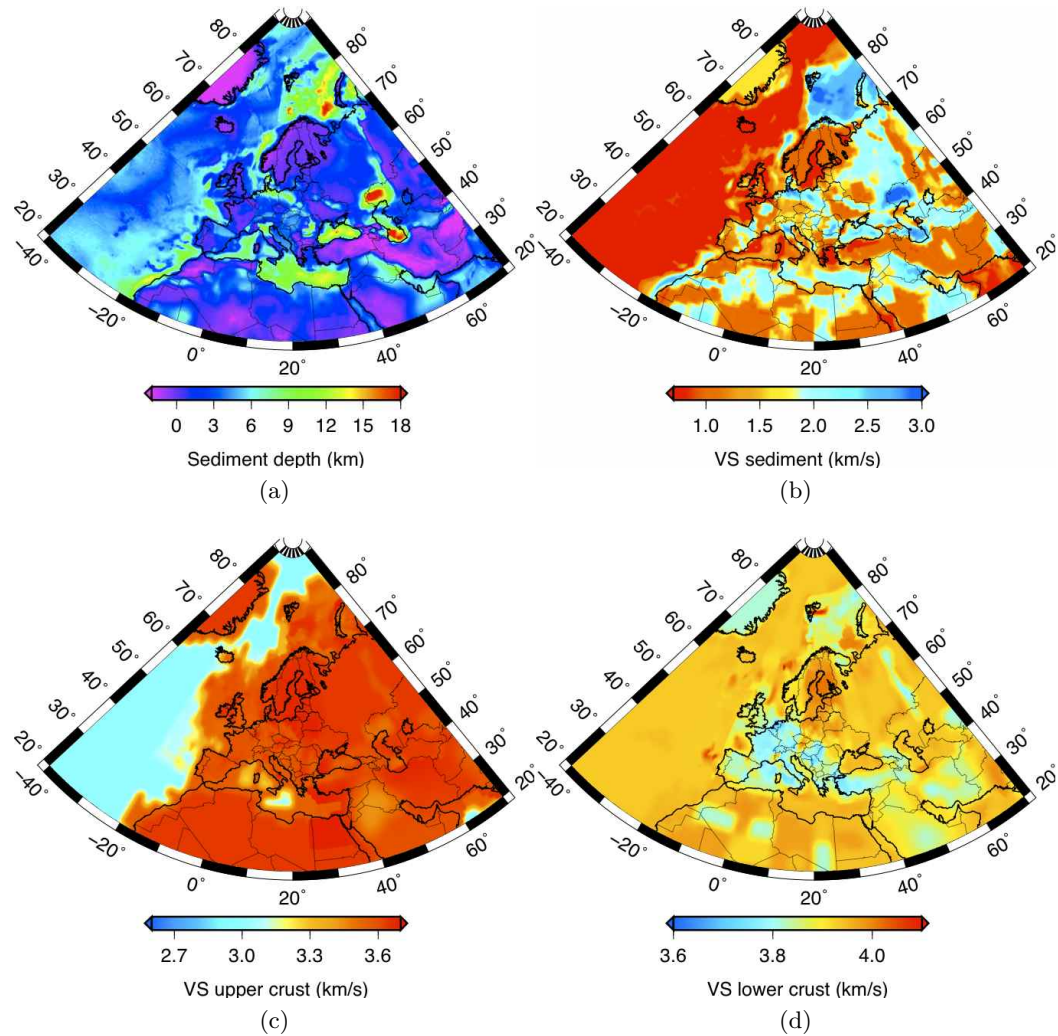


Figure 1.4: *a) EPcrust: sediment layer thickness (km). b) EPcrust: v_S of the sedimentary layer (km/s). c) EPcrust: v_S of the upper crust layer (km/s). d) EPcrust: v_S of the lower crust layer (km/s). (figures from Molinari & Morelli 2011)*

The detailed knowledge of the crustal structure of the plain has a crucial importance for the estimation of ground-shaking and seismic hazard. After the 2012 seismic sequence, the Po Plain has been the subject of renewed interest by, mostly, Italian seismologists.

In the previous decades a number of seismic models with a continental scale had become available for this region. For example EPcrust by Molinari & Morelli (2011) is a crustal model for the European Plate (fig.1.4). It has been derived by the collection and integration of information from previous literature. It covers the full Europe plate from Northern Africa to the North Pole with a resolution of $0.5^\circ \times 0.5^\circ$. The crust is parameterised with a 3-layers setting: sediments, upper crust and lower crust. It can be used for example for seismic wave propagation modelling in a continental scale or linearised crustal correction in seismic tomography. Because of its low resolution it can not be used for local-scale studies such as earthquake scenario computation.

Diehl et al (2009) obtained a 3D P-wave velocity structure of the Alpine crust from local earthquake tomography using a set of high-quality traveltime data. The model covers the depth ranging between 0 and 60 km with a lateral grid of 5 km x 5 km and 1 km of vertical resolution. In their study they located relatively small-scale known geological structures like Ivrea Body, in the western Alps.

Also Wagner et al (2012) focused their attention to the Alpine chain, in particular on the western part. They used a combination of controlled-source seismology (CSS) and local earthquake tomography (LET) data to obtain a 3-D crustal model of the Alps. The combined technique takes advantage by the strengths of both the methods: both CSS and LET data constrained well the Moho and LET constrained mainly the lateral variations of seismic velocities. Their model showed three Moho surfaces: Europe, Liguria and Adria and the major tectonic structures like suture zones and Ivrea Body.

Gualtieri et al (2014) built a model of the whole Italian crustal and shallow mantle structure, including a revised Moho depth map using a regional travel time tomography technique. They inverted 191,850 P_n and P_g wave arrivals from 6850 earthquakes. The final model has a 0.1° lateral resolution and 2 km vertical grid spacing. They used EPcrust model (Molinari & Morelli, 2011) as a-priori information in the non-linear inversion process.

Molinari et al (2015) derived a 3-D crustal structure model for S-wave velocity under Italy and Alpine region. They used a database of Rayleigh-wave phase and group velocities from ambient noise cross-correlations (Verbeke et al., 2012) integrated by a dense set of new ambient-noise-based phase and group velocities observations. They also parameterised the model using the same scheme as EPcrust reference model with a lateral resolution of $0.25^\circ \times 0.25^\circ$ degrees (figure 1.5).

A high-resolution model of the Po Plain has been published by Molinari et al 2015a. The model, named "MAMBo", covers the area of northern-Italy and it has been built with the purpose to have an instrument for local modelling of ground-shaking and seismic scenarios calculation. MAMBo is mainly focused on

the detailed description of the Po Plain with a very high resolution: $0.01^\circ \times 0.01^\circ$. It has been built by the collection and interpretation of all the information on the geological structure available for the plain, mainly obtained in the last decades for hydrocarbon and water exploration. These geological studies gained very reliable information on the depth and thickness of each sedimentary layer, but poor resolution on the seismic parameters associated to them. Seismic parameters inside each layer have been taken from laboratory research and petrological surveys. They are parameterised with two consecutive linear slopes to simulate the velocity increasing as a function of depth and they are laterally uniform. The model is made of a maximum of six superposed layers, from the most recent and shallowest loose sediment layer to the deeper Mesozoic sedimentary layer (see fig.1.6). All the stratigraphic column lies on a crystalline-rock basement. MAMBo has been used to simulate ground-shaking effects of earthquakes localised in the plain using a spectral-element model (SpecFem3D Komatitsch and Tromp, 2002; Peter et al, 2011). Comparison with real-data recordings shows a better agreement than simulation with 1D model used usually to locate earthquakes for the Italian seismic bulletin by INGV (see fig.1.7). The comparison show a reliable better agreement, especially for the simulation of duration of the signal, due to a better simulation of the basin-effect of internal reflections. This model has a very detailed layered structure with a very high resolution. On the other hand seismic velocities and densities inside each layer have been obtained by laboratory surveys and empirical laws between seismic parameters and there is no lateral variation of the seismic parameters inside each layer. Because of these two reasons an update of MAMBo using an independent method is necessary.

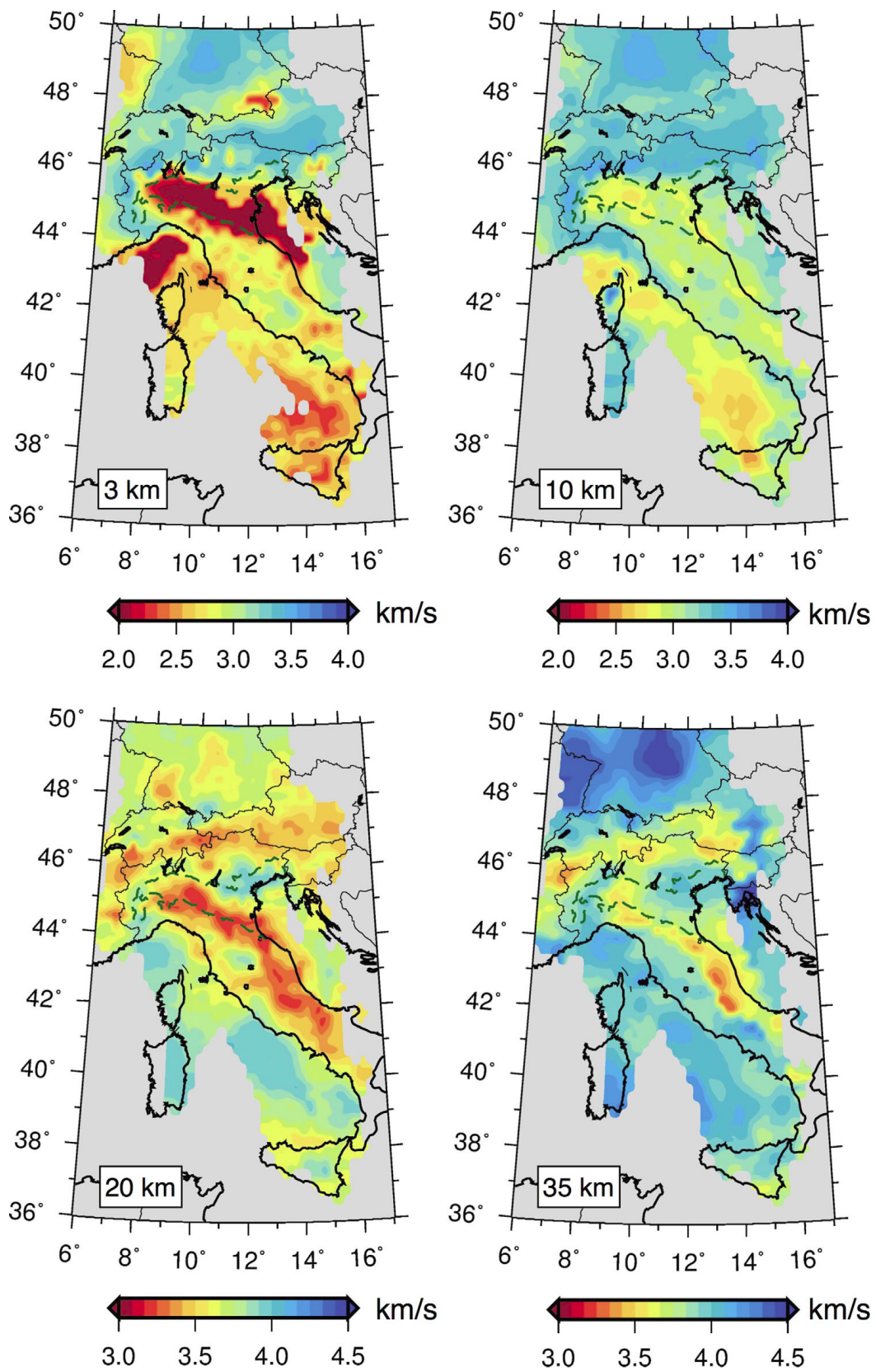


Figure 1.5: Model from Molinari et al (2015b) at different depths.

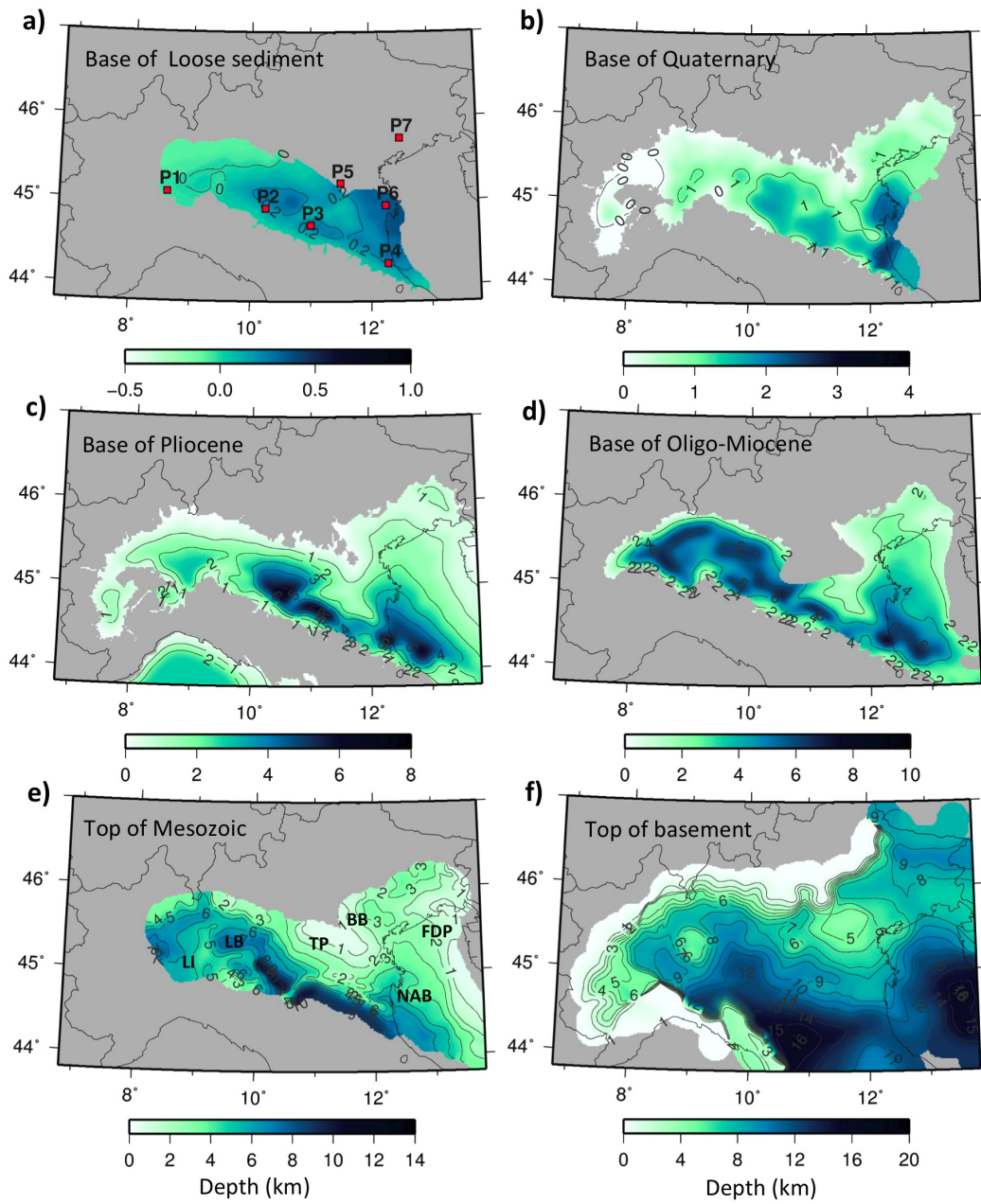


Figure 1.6: Maps of the thickness of the MAMBo sedimentary layers from Molinari et al 2015a.

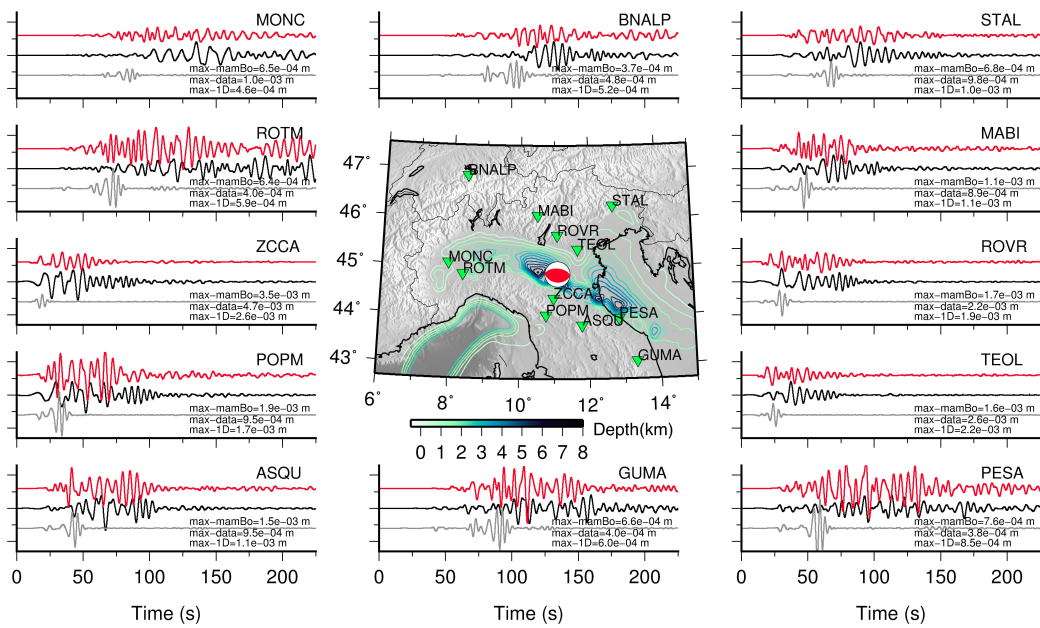


Figure 1.7: Displacement waveform simulation of the 29 May 2012 earthquake ($M_W 5.8$) using SpecFem3D. Red line: simulation using MAMBo. Black line: real data. Gray line: simulation using 1D model used for earthquake location. Amplitudes are normalized. (figure from Molinari et al. 2015a)

Chapter 2

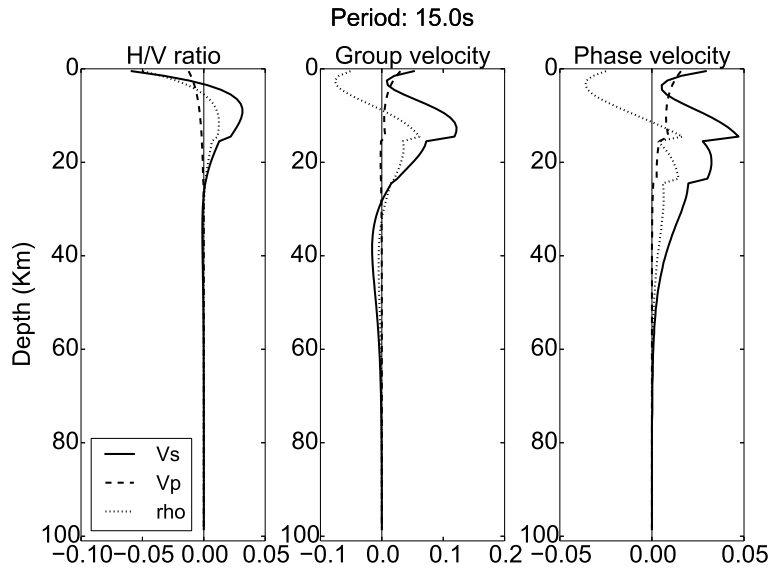
Rayleigh Waves Ellipticity

2.1 Introduction

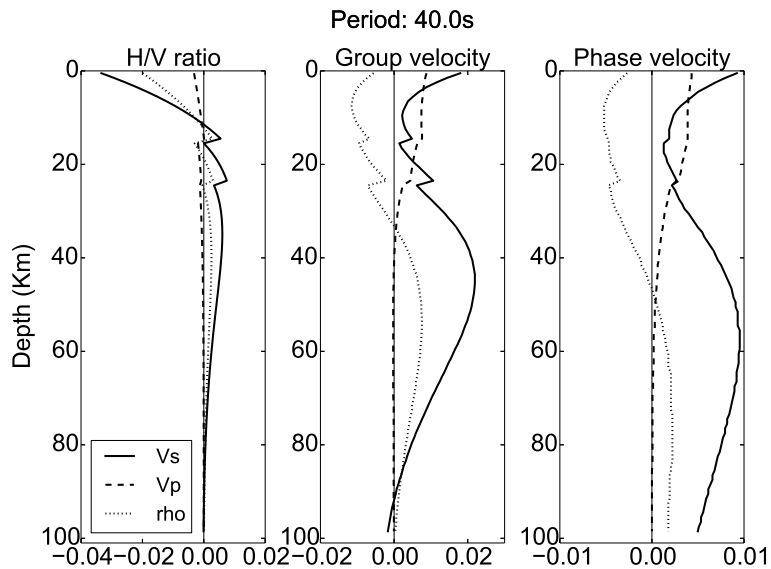
As we have seen in the previous chapter, the detailed knowledge of the shallowest seismic structure of the crust is a key-point for hazard estimates and ground-shaking scenario. Local effects are mainly influenced by the local shallowest structure, especially in sedimentary terrains. The models described in the last section of the previous chapter have been obtained from classical tomography like phase and group velocities (excepted MAMBo model), often measured by the cross-correlation of ambient noise. Phase and group velocities in the period range between 5s and 50s are mostly sensitive to crustal structure ranging between 10 km and 80 km (see fig.2.1). They are not very sensitive to the shallowest part of the crust, corresponding to the sedimentary layers. For this reason surface wave dispersion is not the best observable to model the sedimentary layers.

Rayleigh waves are surface waves P-SV polarised on vertical plane ellipses. They have a quite similar to ocean waves, but the particle motion at the surface is usually retrograde (we will see in the next chapter that this assumption is not always true).

Ellipticity (also named H/V ratio) is a seismic parameter defined as the ratio of amplitudes of vertical and horizontal motion of the Rayleigh wave. Like phase and group velocities, ellipticity depends only on the local structure at the receiver, but it can be measured locally using a single station. Such a characteristic makes ellipticity an interesting alternative observable in the cases of poor or uneven coverage of seismic networks or poor seismicity: it can be measured using teleseisms and it can be applied virtually everywhere in the world.



(a)



(b)

Figure 2.1: Sensitivity kernels for H/V ratio, group and phase velocity at 15 s and 45 s, as a function of v_S (solid line), v_P (dashed line) and density (dotted line) calculated by finite differences using a normal mode formalism for the 1-D Prem Earth model (Dziewonski & Anderson 1981).

As we can see in fig.2.1 ellipticity has a shallower sensitivity compared to phase and group velocities. For example at a period of 15s it has a negative maximum very close to the surface and it decreases around 20 km. At a period of 40s it is sensitive down to around 60 km. This characteristic makes ellipticity a good seismic

observable for very shallow crust imaging. The presence of a large negative peak in the sensitivity kernel of ellipticity shows that this observable has a strongly non-linear behaviour as a function of increasing seismic velocities of the model. This makes ellipticity measurements difficult to be interpreted because the same increase of v_S at two different depths will increase or decrease ellipticity depending if the variation is under or above the zero-crossing of the sensitivity kernel.

H/V ratio is a relatively little known and little used parameter and only a few seismological studies have been published on this topic in the last decades. However it may be very useful in sedimentary basin environments, to retrieve the sedimentary layer structure.

In fact, H/V has been widely used for engineering purposes (Nakamura & Saito, 1983). They measured H/V ratios from ambient noise using a statistical approach, without a proper identification of seismic sources. Here we are concerned on deterministic measurements on particle motion identified as elliptically polarised.

In this chapter we will present the most important previous studies on the subject, and briefly discuss theoretical implications.

2.2 Previous studies

The first studies about ellipticity of Rayleigh waves have been published at the beginning of 80s, when Nakamura & Saito (1983) observed the strong motion records from different sites in Japan. They noticed that in soft soils the horizontal component had larger amplitude than vertical component. In hard-rock sites, instead, the two components were almost equal in terms of both maximum amplitude and waveform. They measured H/V ratio firstly as the ratio between the maximum of the amplitudes of the horizontal and vertical component and they related it with the soil softness and local amplification factor. This result has been confirmed by measuring H/V from the spectral ratio between frequency spectrum of ambient noise, starting from the assumption that ambient noise is mainly composed by Rayleigh waves. They hypothesized that the vertical component of the ambient noise is not strongly influenced by the sedimentary layer and it keeps the characteristics of the Rayleigh waves at the basement. On the other hand the horizontal component is strongly amplified by low-velocity shallow structures. When taking the ratio between the horizontal and vertical component the effects of Rayleigh wave path and source included in the vertical component are cancelled out and only the effects of receiver structure remain. They found a simple relation between the frequency F_0 of the first peak on spectral H/V ratio and impedance contrast and thickness of shallowest layer. In a simplified model with a single slow layer with S-wave velocity C_s and thickness h over a faster hard basement with S-velocity C_b the depth of the

basement is:

$$H = \frac{C_b}{4A_0F_0} \quad (2.1)$$

where A_0 is the impedance contrast

$$A_0 = C_b/C_s \quad (2.2)$$

Nakamura's technique, also called QTS (Quasi-Transfer Spectra), has been widely applied in engineering and microzonation studies to evaluate the local site parameters for hazard mitigation. Such a technique based on ambient noise works with high frequency signals between around 0.1 Hz and 20 Hz. The sensitivity of the method is then limited to the first few hundred meters from the surface. Such a shallow sensitivity is enough for engineering purposes but it is not usable for seismological imaging of the first kilometres of the crust. For this purpose the seismological community focused mainly on the usage of longer period signal such as earthquake recordings.

In the last decades the availability of good-quality and large seismic data gained more attention to the deterministic measurement of ellipticity on earthquake recordings. Ferreira & Woodhouse (2007b) made a first attempt of measuring ellipticity of fundamental mode of Rayleigh wave on earthquake-generated seismic signals at a single period of 150s. They found a clear unexpected variation on H/V results, but the small dataset used did not permit a wide statistical analysis of the results.

Tanimoto & Rivera (2008) introduced two observational approaches to ellipticity measurement on seismic records for a period range between 20s and 250s. Both the schemes work on the phase-shift measurement between vertical and horizontal component and they are based on the assumption that for the fundamental mode Rayleigh wave the two components are phase-shifted by 90° . These methods showed a good capability of detecting and separating the fundamental mode from spurious arrivals for a source-receiver distance ranging between 20° and 140° . They applied the two schemes to a large dataset of real data from all the large events that occurred between 1988 and 2003 recorded by two broadband stations in Southern California. They found similar results for both the schemes and values compatible with theoretical values computed for that seismic structure. They pointed out that measuring ellipticity is possible only using a large amount of data. They also showed that a numerical finite-difference approach is possible for calculating sensitivity kernels for ellipticity.

Yano et al. (2009) measured H/V ratios analysing data from GEOSCOPE network in the period range between 20 and 250s. They also inverted them for v_S structure beneath each station using a linearised method using CRUST2.0 and PREM as starting models. They found that the final solutions are strongly linked

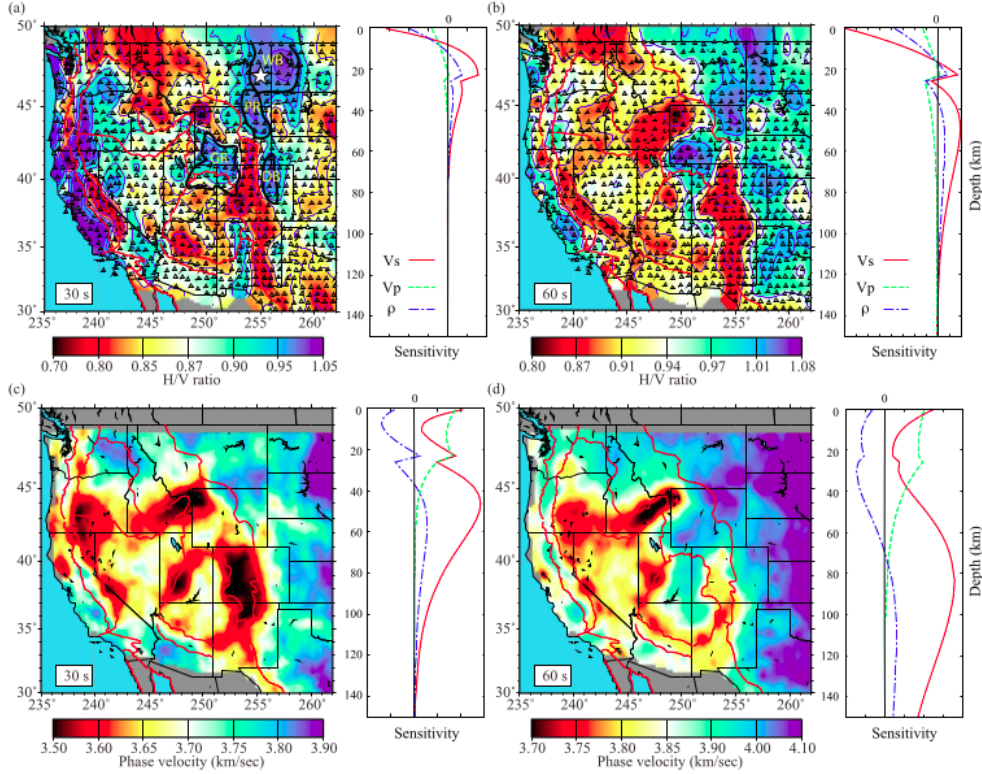


Figure 2.2: *Figure from Lin et al. 2012. (a) The 30 sec Rayleigh wave H/V ratio observed across the USArray. The triangles denote the stations used in the study. The 3 km sediment contours are also shown for several major sedimentary basins. WB: Williston Basin; PR: Powder River Basin; GR: Green River Basin; DB: Denver Basin. The depth sensitivities of 30 sec H/V ratio to v_S , density (ρ), and v_P/v_S perturbation are shown in the right. (b) Same as (a) but for 60 sec H/V ratio. (c, d) Same as (a) and (b) but for Rayleigh wave phase velocity.*

to initial models and the depth of the Moho is a delicate parameter to set up before the inversion. They showed that H/V ratio data can be used as a supplementary information during a joint phase and group velocity inversion because of the different sensitivity in depth.

Lin et al. (2012) jointly inverted for v_S and density structure H/V measurement together with phase-velocities from USArray data available at the time of their work. They used a simple 4 layer parametrization for the crust with Moho depth fixed to values given by previous studies and thickness of the layer fixed. They found that the shallowest structure is better constrained by the joint inversion compared to the inversion with phase-velocity alone. The results are in good agreement with known v_S anomalies in the western US (see figure 2.2).

2.3 Theoretical approach

H/V ratio or, in short, ellipticity depends only on the structure beneath the receiver station through the ratio between eigenfunctions (Ferreira and Woodhouse, 2007). This characteristic derives directly from full ray theory: for a smooth, laterally heterogeneous, slightly anisotropic, anelastic, non-rotating, self-gravitating earth model the amplitude of a surface wave is we can approximate the generic component \hat{v} of the surface wave displacement in the frequency domain as (Woodhouse 1974):

$$u(\omega) = \sum_{\alpha=0}^{\infty} \sum_{n=1}^{\infty} A(\omega) e^{-i\Psi(\omega)} \quad (2.3)$$

Where $A(\omega)$ is the amplitude factor that takes the form:

$$A = A_s A_p A_r \quad (2.4)$$

and the phase:

$$\psi = \psi_s + \psi_p + \psi_r \quad (2.5)$$

Here the subscript s indicates the term depending on the seismic source, p the term depending on the waves path and r the term depending on the structure at the receiver. A_s , A_p , A_r are given by:

$$A_s e^{-i\psi_s} = \frac{1}{\sqrt{C_s}} \mathbf{M} : \mathbf{E}_s^* e^{i\frac{\pi}{4}} \quad (2.6)$$

$$A_p e^{-i\psi_p} = \sqrt{\frac{\lambda}{8\pi S}} e^{\int_{path} \left(-i\lambda_l - \frac{\alpha_l}{c_l}\right) dl + iN\frac{\pi}{2}} \quad (2.7)$$

$$A_r e^{-i\psi_r} = \frac{1}{\sqrt{C_r}} \hat{v} \cdot \mathbf{s}_r \quad (2.8)$$

C is the angular group velocity $C = \frac{\partial\omega}{\partial\lambda}$. \mathbf{s}_r is the local displacement eigenvector at the receiver. For Rayleigh waves it is:

$$\mathbf{s}_r = U_r \hat{\mathbf{r}}_r - iV_r \hat{\mathbf{k}}_r$$

U_r is the radial and K_r is the vertical eigenvalue. A_s and A_p don't have any dependency on which component of $u(\omega)$ we are considering so if we take the ratio between the vertical and radial component of u , A_s and A_p cancel out. We then have:

$$E(\omega) = \frac{u_H(\omega)}{u_V(\omega)} \propto \frac{A_r^H}{A_r^V} \quad (2.9)$$

where $A_r^H \propto -V_r$ and $A_r^Z \propto U_r$. U_r and V_r are the displacement eigenfunctions evaluated at the receiver. Ellipticity will be:

$$E(\omega) \propto -\frac{V_r}{U_r} \tag{2.10}$$

Chapter 3

Ellipticity of Rayleigh waves in basin and hard-rock sites in Northern Italy¹

Abstract

We measure ellipticity of teleseismic Rayleigh waves at 95 seismic stations in Northern Italy, for wave period between 10 s and 110 s, using an automatic technique and a large volume of high-quality seismic recordings from over 500 global earthquakes that occurred in 2008-2014. Northern Italy includes a wide range of crustal structures, from the wide and deep Po Plain sedimentary basin to outcropping sedimentary and crystalline rocks in the Northern Apennines and Alps. It thus provides an excellent case for studying the influence of shallow earth structure on polarisation of surface waves. The ellipticity measurements show excellent spatial correlation with geological features in the region, such as high ellipticity associated with regions of low seismic velocity in the Po Plain and low ellipticity values in faster, hard rock regions in the Alps and Apennine mountains. Moreover, the observed ellipticity values also relate to the thickness of the basement, as highlighted by observed differences beneath the Alps and the Apennines. Comparison between observations and predicted ellipticity from a reference crustal model of the region show substantial fit, particularly for $T \sim 38$ s data. Discrepancy for shorter wave period suggests that slight modifications of the model are needed, and that the ellipticity measurements could help to better constrain the shallow crustal structure of the region. Predictions for the Po Plain are larger than the observations by a factor of four or more and transition from retrograde to prograde Rayleigh wave

¹This chapter has been submitted to Geophysics Journal International and it is currently under review.

motion at the surface for periods of $T \sim 10\text{-}13$ s is predicted for seismic stations in the Plain. Analysis of corresponding real data indicates a possible detection of teleseismic prograde particle motion, but the weak teleseismic earthquake signals are mixed with ambient noise signals at the predicted, short, transition periods. Detection of the period of polarity inversion from the joint analysis of earthquake and ambient noise ellipticity measurements may provide further, stringent, constraints on the structure of sedimentary basins.

3.1 Introduction

Ellipticity of Rayleigh waves (also called H/V ratio) is defined as the ratio between the axes of the elliptically-polarised particle motion, and is measured as the ratio between the displacement amplitude of horizontal and vertical components of the fundamental mode wave train. In a flat layered medium or in a smooth, laterally heterogeneous medium, the H/V ratio depends only on the structure beneath the station, without any dependence on event distance, azimuth, depth or magnitude (e.g., Ferreira and Woodhouse, 2007b). This represents a main advantage of the usage of this observable: using ellipticity we can retrieve earth structure beneath each station without the need of a description of the structure between source and receiver. This feature is particularly relevant in areas with low or uneven data coverage. Ellipticity measurements do not require high seismicity rates in the study area because they can conveniently be performed on teleseismic records, so they can be carried out virtually anywhere. Ellipticity is more sensitive to shallow crustal structure than surface wave group and phase velocity at the same period (Figure 2.1) so it is a useful observable for example for the characterisation of sedimentary basins (e.g., Lin et al., 2012). The situation is somewhat similar to that of receiver function studies, insofar teleseismic records can be used to characterise the structure beneath a receiver. Unlike receiver functions, however, ellipticity is sensitive to seismic velocities (and density) rather than to discontinuities.

The use of Rayleigh wave ellipticity for the determination of crustal structure has been proposed several times in the past (e.g. Boore & Nafi Toksöz, 1969) but for decades other seismic observables have been preferred, such as phase and group velocities of surface waves. This was perhaps due to more difficulties in modelling amplitude rather than phase (arrival time) of a seismic pulse. A H/V spectral technique based on ambient noise signals has been introduced by Nogoshi and Igarashi (1971) and Nakamura (1989). This rather empirical technique — that works without proper identification of Rayleigh-wave polarisation, assuming that background noise is mainly composed by surface waves — has been further developed using small-aperture seismic arrays to derive wavefield characteristics and shear-wave ve-

locity profiles (e.g., Di Giulio et al., 2006; Wathelet et al., 2008), mainly for seismic engineering applications. Over the last decades, a wealth of high-quality seismic data have become available, so the deterministic measurement of ellipticity on the fundamental-mode wave packet of earthquake-generated Rayleigh waves has gained more attention. Some attempts of measuring ellipticity for characterisation of deep earth structure have been done by Ferreira & Woodhouse (2007b). They measured ellipticity at the single period of 150 s, and they found substantial variability in amplitude ratios — in contrast with expectations — possibly revealing the presence of small-scale heterogeneity. However, they used a small dataset that did not permit a statistical analysis of results. Tanimoto & Rivera (2008) developed two automatic schemes to measure ellipticity on a complete seismogram. They applied the method to all the large events that occurred between 1988 and 2003 recorded by two broadband stations in Southern California. They showed that by using a very large set of measurements, the results become statistically consistent and in good agreement with theoretical expectations. On the other hand, their study was limited only to two seismic stations. Other studies recently followed this approach, such as Yano et al. (2009), Lin et al. (2012) and Lin et al. (2014). In particular, Lin et al. (2012) jointly inverted H/V measurements together with phase velocities of ambient noise Rayleigh waves in the western United States, using data from all USArray stations available at the time of their study. Phase velocity is sensitive to deeper structure than H/V (Figure 2.1) so the joint inversion allows a better illumination of crust and upper mantle structure. On the other hand, by using phase velocity measurements, the technique is not based on single stations any more.

Northern Italy includes a wide variety of crustal structures ranging from the wide and deep Po Plain sedimentary basin, to outcropping sedimentary and crystalline rocks in the elevated terrains of the Northern Apennines and Alps, representing an excellent laboratory for validating seismic appraisal techniques aimed at gauging shallow earth structure. Tomographically-imaged crustal shear-wave velocities are generally low beneath the Po Plain and Molasse basins, and high velocities are seen in the crystalline crust of the Alpine mountain belt (e.g., Molinari et al., 2015b). This region has been hit in 2012 by two earthquakes, on two close tectonic structures ($M_W = 5.9$ on May 20th, 2012, and $M_W = 5.8$ on May 29th, 2012) that caused extensive damage, hundreds of injuries, and 27 fatalities, in spite of their moderate magnitudes. These events revealed considerable seismic vulnerability of this region, even for relatively modest earthquakes. Significant damage appears to be due to high exposure of this territory associated high density of population and industries, and because of local amplification of seismic waves caused by sedimentary basin structures. Seismic knowledge of this region has recently improved due to renewed interest and recent investigations. For example, the recent 3D seismic

model MAMBo (Molinari et al., 2015a) has been constructed collecting and merging information from geological studies and active-source experiments carried on during the 80's and 90's decades of the last century for hydrocarbon and water research. MAMBo is a rather reliable 3D model including laterally-varying thickness of stratigraphic layers, that has shown to be quite accurate in modelling seismic wave propagation at a regional scale. However, being mostly based on a compilation of geological and geophysical information, MAMBo has not been directly constructed inverting seismic data. The many new broadband seismic stations deployed in the region in the past decade offer an opportunity to further refine this model. Thus, the northern Italian basin and neighbouring mountain belts, with a large variety of geological terrains, wide availability of recent data, evolving background geological and geophysical studies, and a reliable *a priori* seismic model of the crust, seem an excellent candidate for a comprehensive analysis of Rayleigh wave ellipticity.

The main objective of this study is to evaluate the reliability of observation of Rayleigh wave ellipticity, and its dependence on local crustal structure (or other factors) in diverse geological situations. With this purpose, we carry out extensive measurements on fundamental-mode Rayleigh wave trains from teleseismic earthquake records in Northern Italy. We investigate the reliability and robustness of the measurements, and the response of hard rock v_S . sedimentary sites. We preliminary assess potential azimuthal misalignments in the seismic stations in the region, which could have an impact on amplitude measurements. We also quantify the differences between observations and predictions for the MAMBo crustal model, and examine the possibility of identifying prograde v_S . retrograde (normal) particle motion and its use to constrain shallow earth structure. Finally, we assess the validity of our approach using complete theoretical seismograms for a 3-D Earth model.

3.2 Data

Events distribution

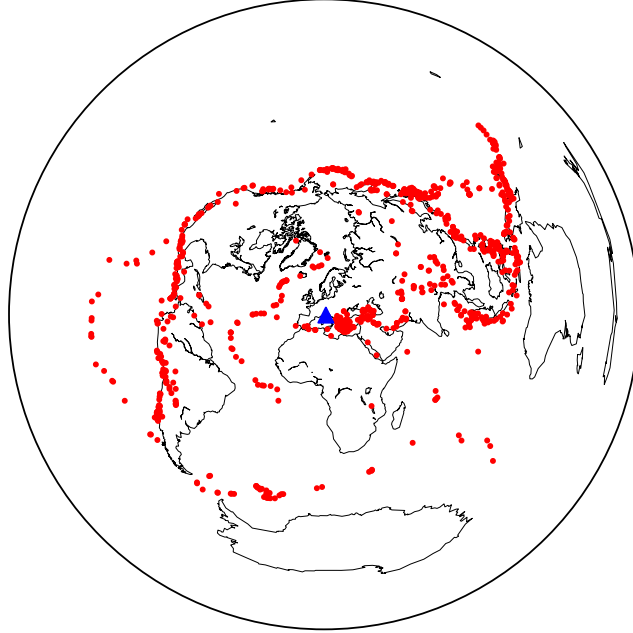


Figure 3.1: *Distribution of the events database used in this study. We used earthquake with epicentral distance between 10° and 140° from the stations and $m_W \geq 5.0$ occurred from January 2008 to December 2014.*

We focus our attention on the northern part of Italy, in a region encompassing the Po Plain, the northern Apennines and the Alps (Figure 3.2). We use data from 95 seismic stations belonging to different networks: Italian Seismic Network (47 stations), South Tyrol Seismic Network (7 stations), North East Italy Broad Band Network (8 stations), Swiss Seismological Network (9 stations), MEDNET Project (5 stations) and Regional Seismic Network of Northwestern Italy (19 stations). We collected all the data from the ORFEUS data center. For each station we select earthquakes with magnitude $M_W \geq 5.0$ and epicentral distance between 10 and 140 degrees that occurred from January 2008 to December 2014 (see figure 3.1). We measure ellipticity on all available data, using the measurement scheme described in the following section, in the period range between 10 s and 110 s. We perform measurements excluding all the data with an estimated signal-to-noise ratio less than 100. We also remove clear outliers with computed H/V ratio ≥ 10.0 and H/V ratio ≤ 0.1 , since such values are not realistic (see theoretical predictions in the next section). We then calculate the median and percentiles of the ellipticity

measurements corresponding to $\pm\sigma$.

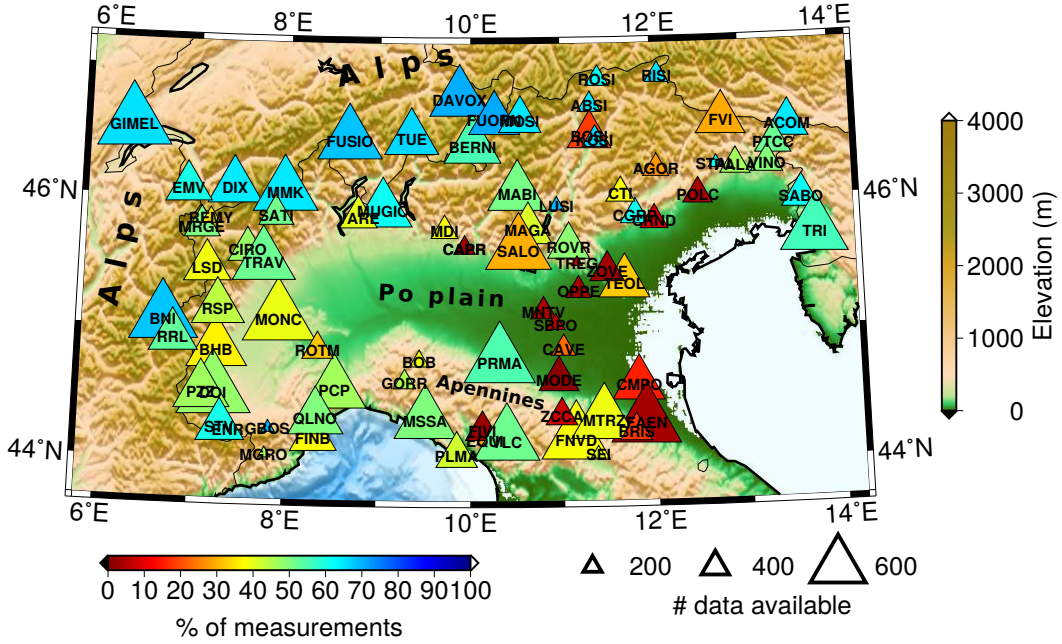


Figure 3.2: *Seismic stations used and corresponding number of measurements. The triangle size indicates the number of earthquake records available for each station and its color represents the percentage of successful measurements. Stations in the Po Plain sedimentary basin generally perform worse (see main text).*

Figure 3.2 shows, for each station, the number of earthquake records retrieved from the database (depending on data availability and station operation), for which an attempt to measure ellipticity has been done; and the success rate, i.e., the ratio of number of measurements effectively obtained v_S . the number of attempts. We notice that the measurement success rate is generally much lower for stations in the sedimentary plain than for stations on the mountain belts. This is probably due to two main reasons: 1) noisier locations in the plain, due to anthropic activities; and 2) more complex crustal structure of sedimentary layers that causes the superposition of the fundamental mode with overtones, reflected/converted modes, and other spurious arrivals. Some of the stations on the plain also have fewer data (smaller triangles in Figure 3.2) because they have been installed more recently than other stations.

Measurements of seismic wave amplitudes can be affected by systematic errors due to problems in the station set-up, such as orientation or amplitude response of horizontal sensors. If sensor pairs are not perfectly aligned (north and east), the amplitude of the horizontal component of Rayleigh waves will be under-estimated, because of the wrong rotation from north and east directions to the radial compo-

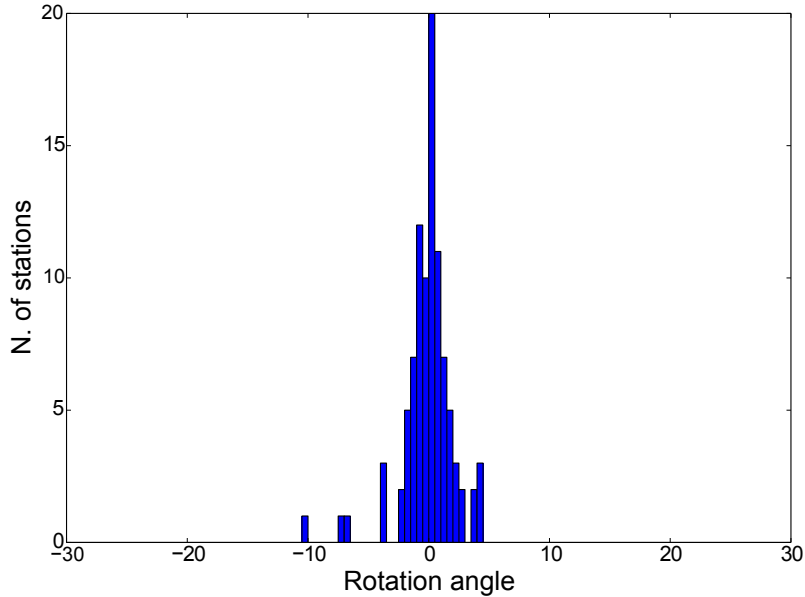


Figure 3.3: *Frequency histogram of azimuthal angle deflections with respect to the theoretical great circle path. The maximum angle found is $\delta\alpha = -10.42^\circ$. Mean $\delta\alpha = -0.07^\circ$. Standard deviation = 2.15° .*

ment of motion. Errors in sensor bearing are not so rare: Ekström & Busby (2008) found alignment errors up to 20 degrees for USArray stations. For this reason we implemented an algorithm for the determination of possible errors due to the misalignment of sensors. We started from the technique outlined by Ekström & Busby (2008). For each station we calculate synthetic seismograms using normal mode summation (Gilbert, 1970; Herrmann, 2013) for PREM (Dziewonski & Anderson 1981) for radial and transverse components, and we compare them to the corresponding components of real data, rotated from N-E (geographical) to R-T (radial-transverse) using the great circle path filtered with a Butterworth-bandpass filter in the range 100s - 150s. Then we rotate the R-T components of real seismograms from -90° to $+90^\circ$ with 1.0° steps. At each step we compute the correlation coefficient C between the data and the synthetics using the following equation:

$$C = \frac{\sum_{i=1}^N o_i s_i}{\sqrt{\sum_{i=1}^N o_i^2 \sum_{i=1}^N s_i^2}} \quad (3.1)$$

where o_i are the observed data and s_i are the synthetic. N is the number of time points in the surface wave window. We then recalculate C for the radial and transverse component at each rotational step. We define the total correlation coefficient

C_{TOT} as:

$$C_{TOT}(\delta\alpha) = \min(|C_R(\delta\alpha)|, |C_T(\delta\alpha)|) \quad (3.2)$$

where $\delta\alpha$ is the correction angle. The best correction angle $\delta\alpha$ is the one that corresponds to maximum C_{TOT} .

We run the algorithm for each earthquake available and for each station. We statistically summarize the $\delta\alpha$ found and calculate the median for each station. We then obtain a correction angle for each station. The results of this analysis are shown in Figure 3.3. We found for most of the stations rather small correction angles: the maximum angle found is -10.42° , but most values are smaller than about 3° (with a mean and standard deviation of -0.07° and 2.15° , respectively), corresponding to a maximum underestimation of the radial amplitude generally less than 0.2%, that is small enough for the purpose of this study. Hence, we do not deem necessary to apply azimuthal corrections for our further analyses.

3.3 Measurement scheme and results

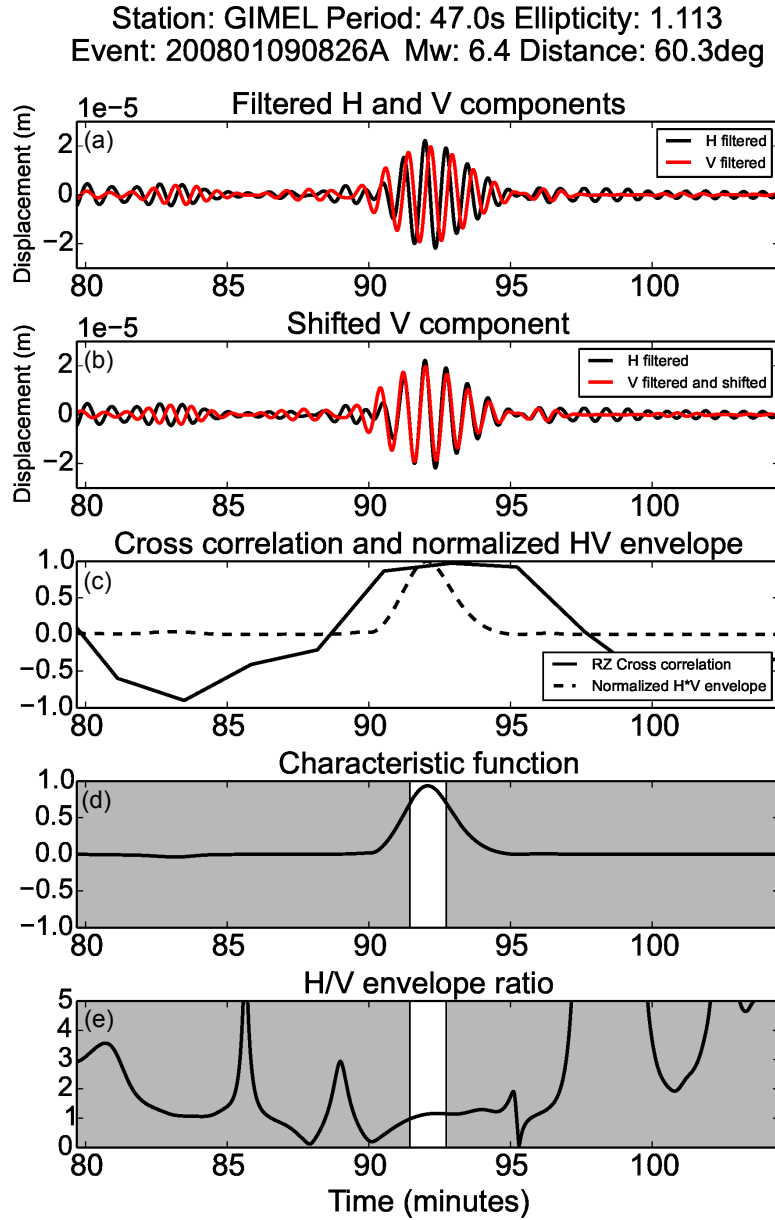


Figure 3.4: *Measurement scheme shown for an earthquake at a distance of 60.3° and magnitude $M_W = 6.4$. We apply a bandpass filter to H and V components (a) and we shift the V component of 90° in advance (b). Then we calculate the cross-correlation between the two signals and the envelope (c). Subsequently we define a characteristic function as the product of cross-correlation and envelope (d). This function defines a time window that contains the fundamental mode of Rayleigh waves. We calculate ellipticity as the mean ratio between the V and the H envelope inside the time window (e).*

The first and main difficulty in the determination of the H/V ratio are the detection and identification of the Rayleigh fundamental mode wave train from the rest of the signal. To do this we look for the particular elliptical and retrograde polarisation of Rayleigh waves. In theory, the radial component is 90° degrees phase-advanced with respect to the vertical component for smooth, laterally varying media. Starting from this assumption we implemented a measurement scheme based on that proposed by Tanimoto & Rivera (2008). This is illustrated in Figure 3.4. We first measure the signal-to-noise ratio (SNR) on all the records by comparing the maximum amplitude in the Rayleigh-wave time window to the average background noise amplitude in a 10-minute pre-event window, and then discard records with SNR below 100. We then apply a narrow Butterworth bandpass filter to the vertical and radial components, and phase-shift the vertical component advancing it by 90° . When the signal consists of fundamental-mode Rayleigh-wave motion, the two components will match. We then cross-correlate the radial and the phase-shifted vertical components, and multiply the result by the product of the envelopes of both components. We thus obtain a characteristic function that defines a time window as it exceeds a pre-defined threshold, where the measurement is made. This, in fact, applies a further requirement on the coherence and amplitude of the signal beyond the noise level, as a condition must be met not only on high cross-correlation but also — via multiplication by envelopes — on amplitude of signal as compared to noise. This measurement technique proved very selective, and very effective in separating the fundamental mode Rayleigh wave from the rest of the signal, but we need a large data set in order to have enough measurements. We carry out these measurements for many earthquakes, and calculate median and percentiles of results. As we consider the ratio of two positive numbers, either of which can become very small, rather than using the straight amplitude ratio — H/V or V/H — we always use and show the logarithm of the ratio $\log_{10}(H/V)$, that is better behaved and statistically more meaningful.

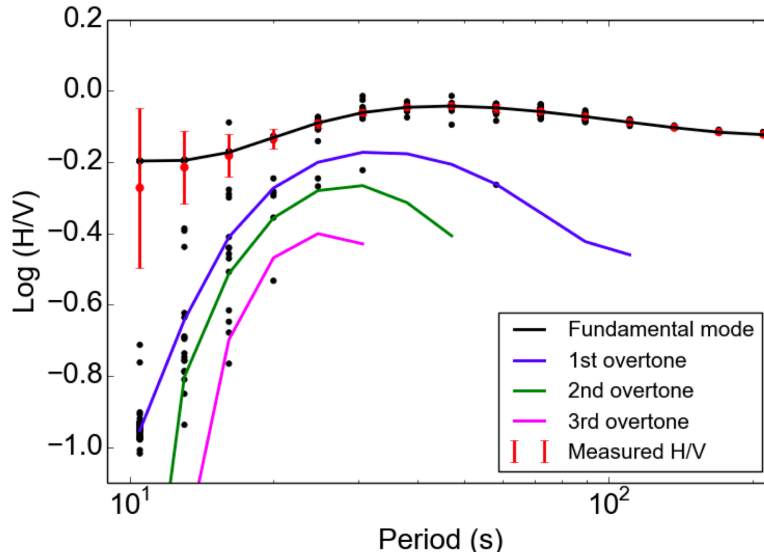
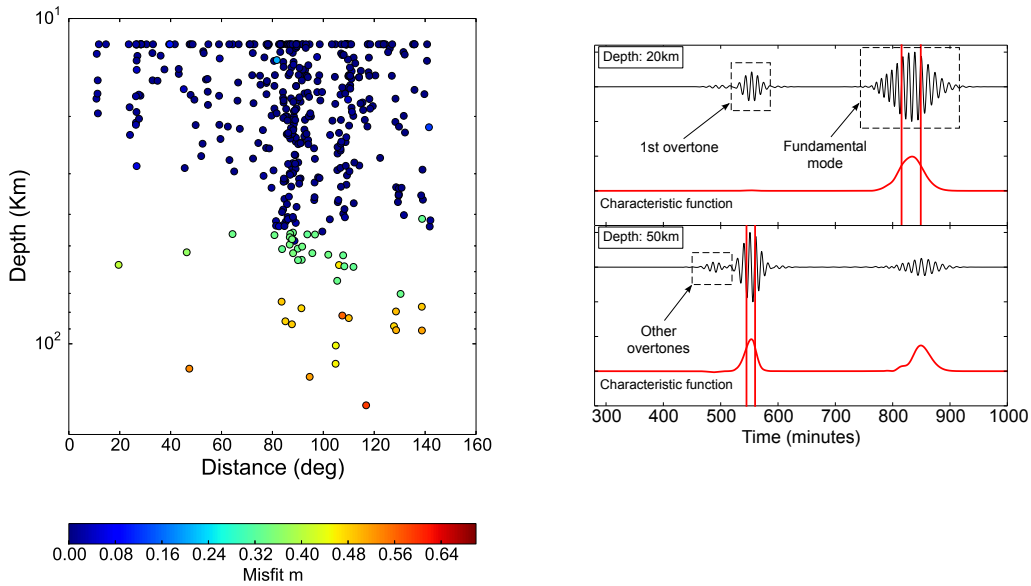


Figure 3.5: Comparison between theoretical H/V values and measurements on synthetic seismograms, for 426 CMT solutions of real earthquakes. Theoretical ellipticity for the fundamental mode and first three overtones is represented by lines in different colour. Measurements from full synthetic seismograms calculated for PREM correspond to the black dots. Note that there are 426 dots for each period, mostly concentrated near the average, indicated by a red dot with error bars. The presence of overtones (with different ellipticity ratios) influences some measurements at shorter periods, but these appear as outliers well outside the $\pm\sigma$ error bars of the measurements. (Note that, for shorter periods, many dots overlap actually appearing as one, near the black curve, and control the value of the average shown with error brackets.)



(a)

(b)

Figure 3.6: (a): Mean misfit (for all periods) between ellipticity computed for an earthquake on synthetic seismograms, and theoretical value, as a function of hypocentral depth. (b): Synthetic seismograms and characteristic function for sample cases for hypocenters at 20 and 50 km depth in PREM. For depths larger than ~ 40 km the first overtone dominates and misleads the characteristic function. The

misfit is calculated using: $m = \frac{\sum_{i=1}^N |E_i^m - E_i^t|}{\sum_{i=1}^N |E_i^m|}$, where N is the number of periods, E^m is the ellipticity measured on synthetics and E^t is the theoretical ellipticity calculated from eigenfunctions.

To validate and quantify the ability of this scheme to detect and estimate H/V ratios, we compute synthetic seismograms using normal mode summation and we measure the H/V ratio on these synthetics. We then compare the results with theoretical ellipticity curves calculated as the ratio of spheroidal mode horizontal and vertical eigenfunctions evaluated at the Earth surface (e.g., Ferreira & Woodhouse, 2007b). For both synthetic seismograms and theoretical values we use the global model PREM (Dziewonski & Anderson 1981). We perform this calculation for an ensemble of 426 centroid-moment tensors of real earthquakes from the Global CMT catalogue (GCMT, Dziewonski et al. 1981; Ekström et al. 2012; <http://www.globalcmt.org/CMTsearch.html>) — the same set used for the analysis on real data. Figure 3.5 shows these results, i.e., 426 ellipticity values for 15

wave periods between 10 seconds and 200 seconds. As expected, measured ellipticity mostly concentrates quite well along the theoretical value for the fundamental mode (black line). At shorter periods ($< 30s$) a few events show a bias of measurements with respect to values expected for the fundamental mode. These outliers can be attributed to the overlap of overtones, which have lower H/V (see Figure 3.5) and may in some cases appear conspicuously on the waveforms. In fact, while we did not find any dependence of measured ellipticity on back azimuth, focal mechanism, magnitude, or time, there is some correlation with focal depth, as shown in Figure 3.6a. For focal depths larger than about 40 km the misfit increases. We verify that this is due to the increased excitation of overtones for deeper events. Figure 3.6b shows the characteristic function, used to identify the wiggles on the seismograms to compute H/V amplitude ratio, for two PREM synthetic seismograms for earthquakes with 20 km and 50 km depth. For depths larger than about 40 km, the first overtone dominates and misleads the characteristic function, which affects the ensuing amplitude ratio measurement. In real measurements, a selection of crustal earthquakes therefore avoids this source of error. We then proceed to make measurements on real data for all the stations shown in Figure 3.2, for 12 wave periods between 10 s and 110 s. Results for two sample stations are shown in Figure 3.8 where, for reference, we also plot the theoretical ellipticity curve for PREM. The behaviour of the measured ellipticity as a function of period is rather smooth and stable. For longer periods, both stations show ellipticity values similar to those of PREM, but deviate quite significantly for the shorter periods. The difference is more notable for PRMA, a station on the edge of the sedimentary basin, than for GIMEL, which is located in the Alps (Figure 3.2). This difference reflects different crustal structures beneath the stations, as we will discuss in the following section.

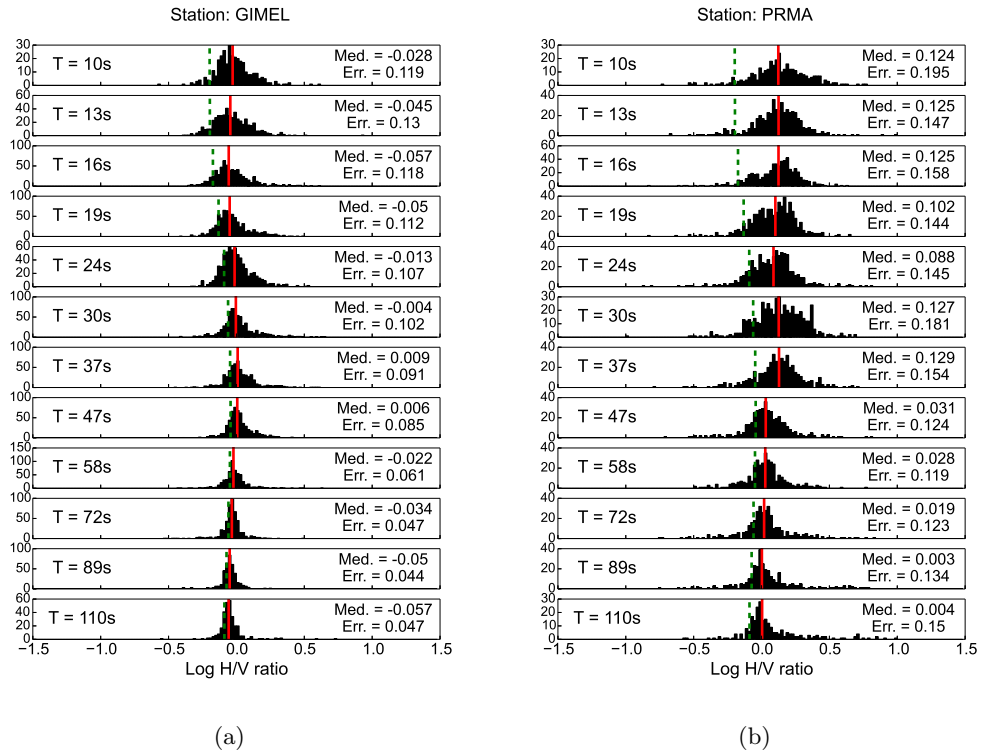
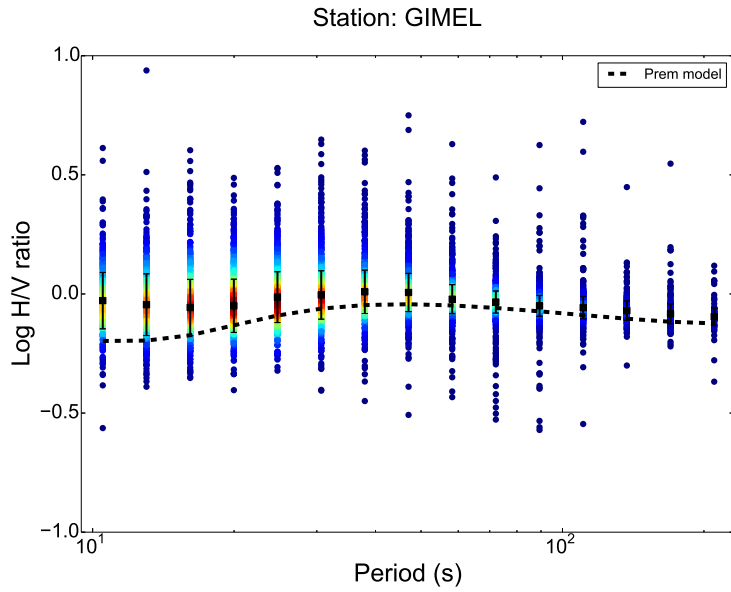
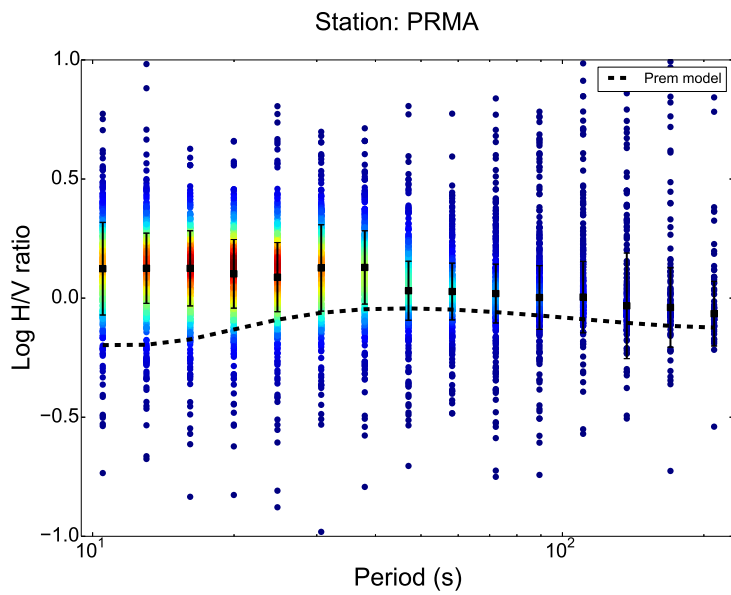


Figure 3.7: Histograms of ellipticity measurements for station GIMEL (a) and PRMA (b). Red vertical line indicates H/V median, also reported in the labels with the corresponding error. Errors are calculated using the percentiles corresponding to 15.9 and 84.1. Green dashed line is the ellipticity calculated on Prem reference model.



(a)



(b)

Figure 3.8: H/V measurements for stations GIMEL and PRMA as a function of period. Different colors show the density of dots. Dashed line is the theoretical ellipticity for the PREM model.

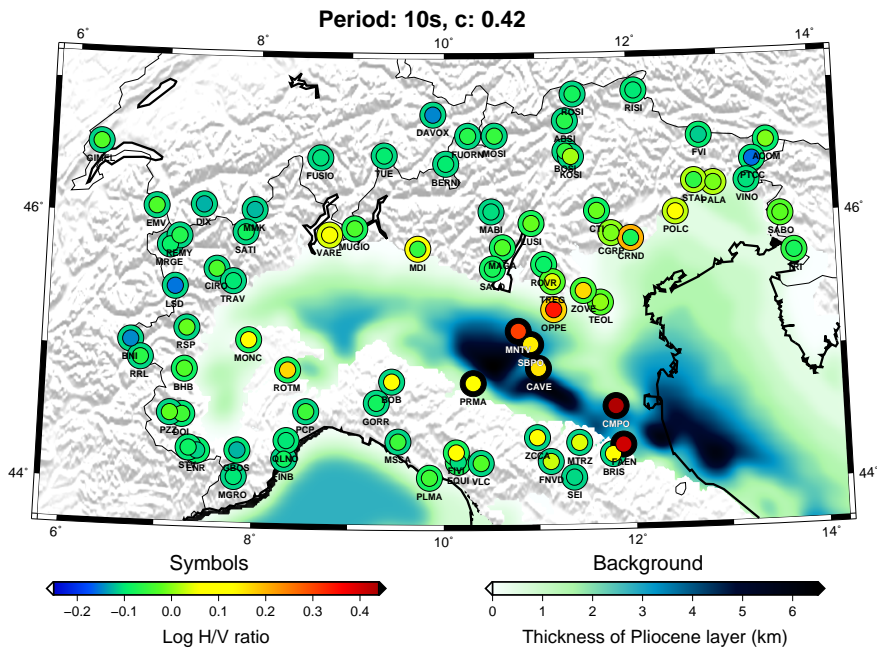
Figure 3.9 and 3.10 show the measured H/V ratios at four sample periods (10 s, 16 s, 24 s, 37 s) for all stations, superimposed on a map of thickness on the Pliocene sedimentary layer in model MAMBo (Molinari et al., 2015a). As explained previously, MAMBo is a recent seismic model of the sedimentary basin of this region, and it integrates information from exploration geophysics and geological studies

performed in the last decades for hydrocarbon and water research. It describes the basin with six sedimentary layers, among which the Pliocene deposits represent the seismically most relevant unit. We computed theoretical H/V ratios for this crustal model combined with PREM velocities in the upper mantle. Large-scale tomographic models show only slight lateral variation of shear wave velocity at the top of the mantle over this region, and values always very close (within $\pm 1\%$) to PREM (e.g., Schivardi and Morelli, 2011) so — given the weak sensitivity to mantle depths — this simplification appears legitimate. For each station, such theoretical prediction is shown with color in the outer ring of symbols in the map of Figure 3.9 and 3.10 to be compared with measured values, plotted instead in the inner circle. The Pearson correlation coefficient between predictions and observations is computed for each period, and is shown in the title of each diagram. The measured ellipticity values clearly correlate with geological features. We observe higher values of H/V (reddish colours) for stations in the sedimentary basin (e.g., MNTV, SBPO, CAVE, CMPO, PRMA, ROTM). This is particularly clear for shorter periods (Figure 3.9), as we expect from the sensitivity kernels (Figure 2.1). On the other hand, stations in the Alps and Apennines show lower values of H/V . For the longest wave period (Figure 3.10b) we notice that stations in the Apennines (southern side of the plain) have higher observed values of H/V compared to Alpine stations, which likely reflects the deeper basement beneath the Apennines than in the Alps (e.g., Molinari et al., 2015a).

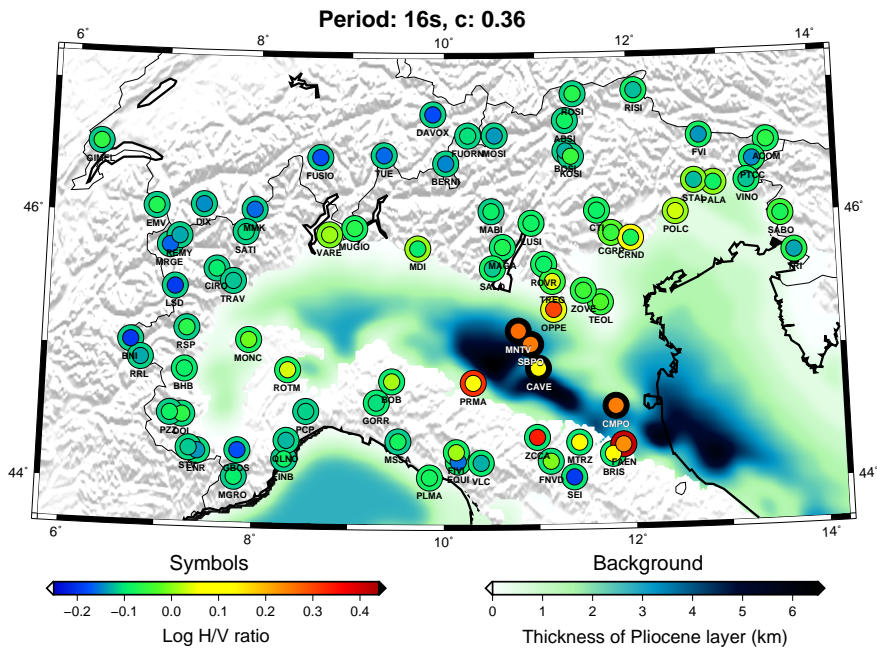
Comparing the H/V ratio predictions for the MAMBo model (outer rings) and the observations (inner circles), we see that for stations in the Apennines and in the Alps, MAMBo predictions are nearly constant and in good agreement with observations at many stations. However, the observations show some lateral variations not predicted by MAMBo, notably a region of decreased ellipticity in the North Western Alps (Figure 3.9b and 3.10a; e.g., for stations DAVOX, TUE, FUSIO, DIX, MMK, MRGE, LSD). This correlates well with increased upper and mid-crustal v_P and v_S in the Western Alps, with respect to the Eastern Alps (Gualtieri et al., 2014; Molinari et al., 2015b) via negative sensitivity of H/V (kernels in Figure 2.1). In the Po Plain, the MAMBo model predicts ellipticity values much larger than observed for the two shortest wave periods by a factor of about four (Figure 3.9); this discrepancy will be discussed in the next section. Finally, there is generally an improved agreement between the predictions and observations for the longest wave period (Figure 3.10b), which is probably due to the sensitivity of these data to deeper, simpler structure.

Lateral resolution is still an open issue. The variations also observed at short distances may perhaps be related to the fact that amplitude data are more sensitive to small scale structure than phase (or travel times). Some variability at short

spatial scale has indeed been observed in other H/V studies (e.g., Lin et al 2012), but the larger spacing between USArray stations used (about 70 km) does not allow a clear assessment. The SEM simulations we show here are not very informative to this purpose, because the crustal model we use has resolution wider than the station spacing, and hence not very relevant for this particular test. Unfortunately computing synthetics with such a fine grid needs longer computational time and would be well beyond the scope of this study. We may also speculate that, because sensitivity kernels are shallow and very peaked at the surface, a local, very shallow, very slow heterogeneity could in principle affect one single station only and not show up in neighbouring ones, even for the longer of the periods we consider.

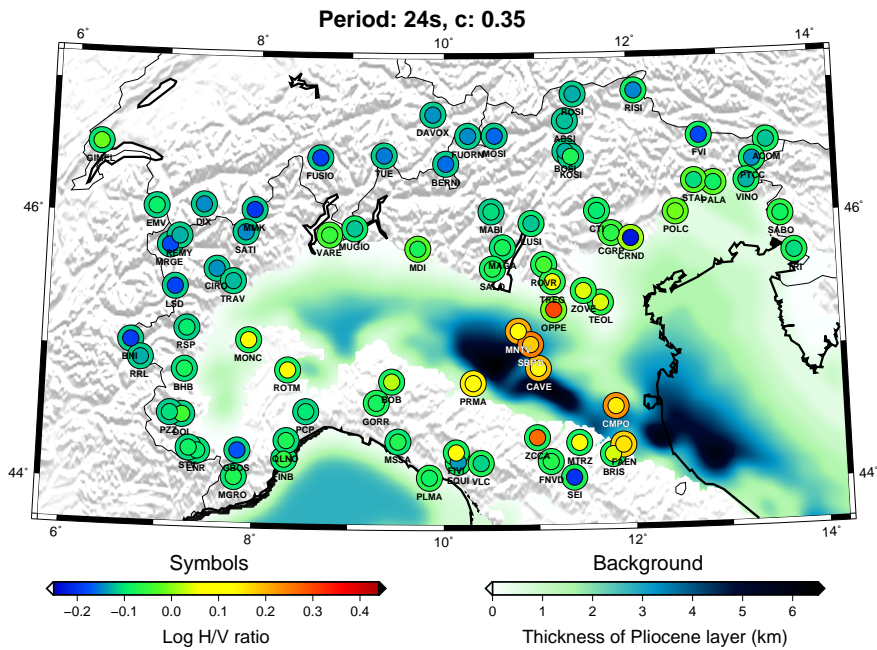


(a)

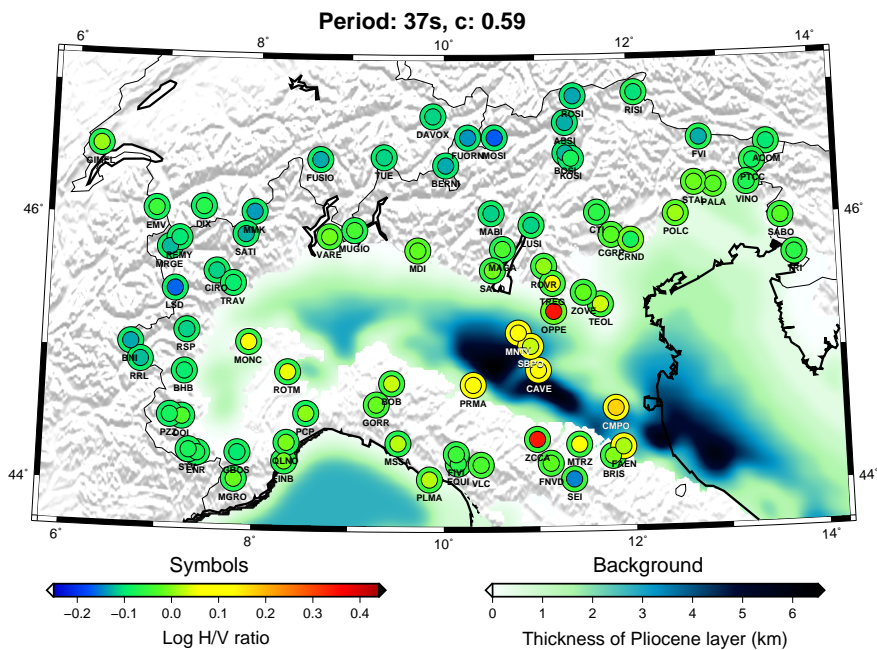


(b)

Figure 3.9: H/V ratios for different periods (shown in coloured solid circles) compared with theoretical values for model MAMBo (Molinari et al., 2015a) shown in the outer rings. Black outer ring means that ellipticity values are greater than 0.6, going up to 2.0 (FAEN station). The Pearson correlation coefficient between the observations and predictions is shown in the title of each diagram. The background shows thickness of the Pliocene sedimentary layer according to model MAMBo.



(a)



(b)

Figure 3.10: H/V ratios for different periods (shown in coloured solid circles) compared with theoretical values for model MAMBo (Molinari et al., 2015a) shown in the outer rings. Black outer ring means that ellipticity values are greater than 0.6, going up to 2.0 (FAEN station). The Pearson correlation coefficient between the observations and predictions is shown in the title of each diagram. The background shows thickness of the Pliocene sedimentary layer according to model MAMBo.

3.4 Rayleigh wave ellipticity predictions from 3-D synthetics

Ellipticity of Rayleigh waves is a local property of the elastic medium. In this, it is not different from, e.g., phase velocity. However, generally we cannot measure local phase velocity directly: rather, we measure a phase difference (or a travel time) between two points at some distance, so a phase measurement brings information on phase velocity integrated along a path. Measurement of ellipticity at a single station, instead, brings information solely on the structure beneath the seismograph, and not about the whole path travelled by the wave. This dependency of ellipticity only on the structure beneath the receiver station can be demonstrated for a smooth, laterally heterogeneous, slightly anisotropic, anelastic, non-rotating, self-gravitating medium using full ray theory (e.g., Ferreira and Woodhouse, 2007a,b). However, one can question whether such description is valid for realistic 3-D Earth models and for the wave periods considered in this study.

In order to address this question, we perform a synthetic test. We compute synthetic seismograms of a real earthquake with `SPECFEM3D_GLOBE` (Komatitsch and Tromp, 2002; Peter et al, 2011), which is a widely used code for the simulation of seismic wave propagation. It is based on the spectral-element method (SEM) and it accurately simulates complete waveforms in complex media. We perform simulations using a global 3D Earth model combining the recent global mantle model `SGLOBE-rani` (Chang et al., 2015) with the crustal model `Crust2.0` (Laske et al., 2012). We use an event that occurred in Costa Rica on July 5th, 2012, with $M_W = 6.8$ and 29.7 km hypocentral depth, at a distance of approximately 88° from the area of study. The SEM synthetics are computed using 3456 processors and are accurate down to a period of ~ 5.6 s. H/V ratios are then measured on the SEM synthetics using the same measurement technique as that used with real data. We also compute theoretical ellipticity using 1D models with the same structure as in the 3D Earth model beneath each station in Northern Italy. We then compare the SEM H/V ratios with the theoretical predictions from the 1-D models as a function of the wave period. We see in Figure 3.11 that overall there is a good agreement between the values of ellipticity measured on the 3D synthetics and the theoretical predictions for the local 1D models, notably for wave period $T \sim 25-72$ s. Differences are always smaller than the errors of real data measurements shown as grey error bars, which further strengthens the validity of our approach. We also compare the SEM H/V ratios with real data measurements (Figure 3.12). As expected, there are larger differences between them than in Figure 3.11 because the real structure in the study region is much more complex than in `CRUST2.0`. These discrepancies, along with the differences between predictions and observations seen in Figure 3.9

Event: 201209051442A
Mw: 7.7 Distance: 87.2deg

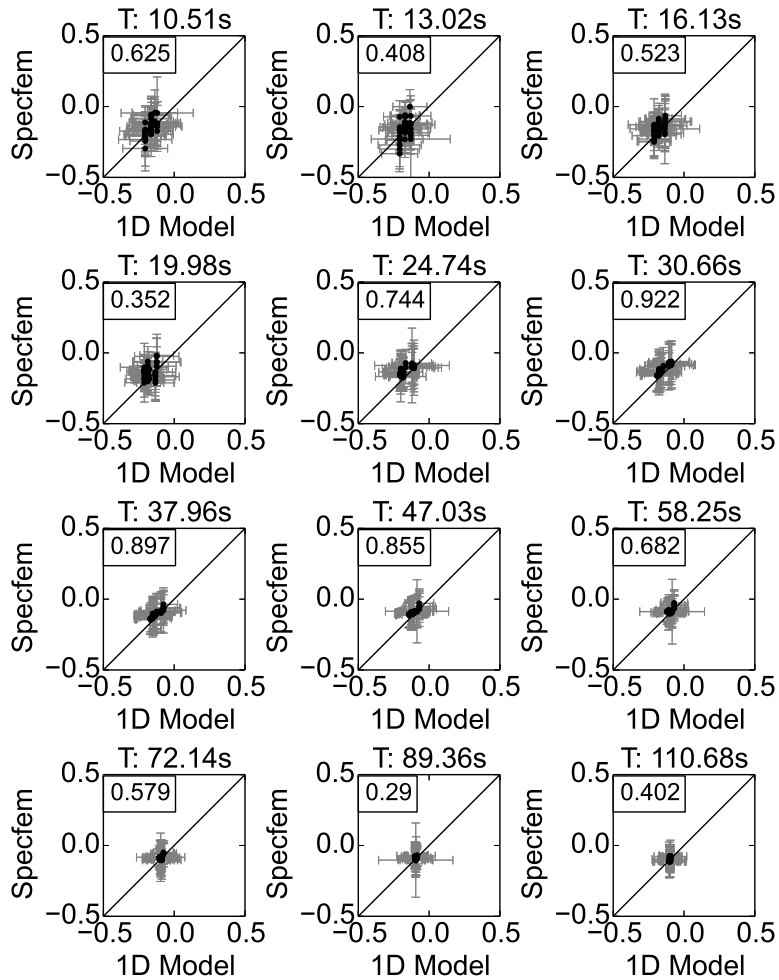


Figure 3.11: Comparison between ellipticity measured on synthetic seismograms computed with a 3D model and ellipticity measured on synthetics computed with a 1D model built using the 3D profiles beneath each station. The bars are the errors associated with real measurements from each station. They give an estimate of the errors expected in real measurements (see figure 3.12). In the boxes the correlation coefficient between the two datasets is shown. This test shows that the local 1D approximation at the receiver can be used instead of a 3D model from source to receiver. The errors are always under the observed data errors.

Event: 201209051442A
Mw: 7.7 Distance: 87.2deg

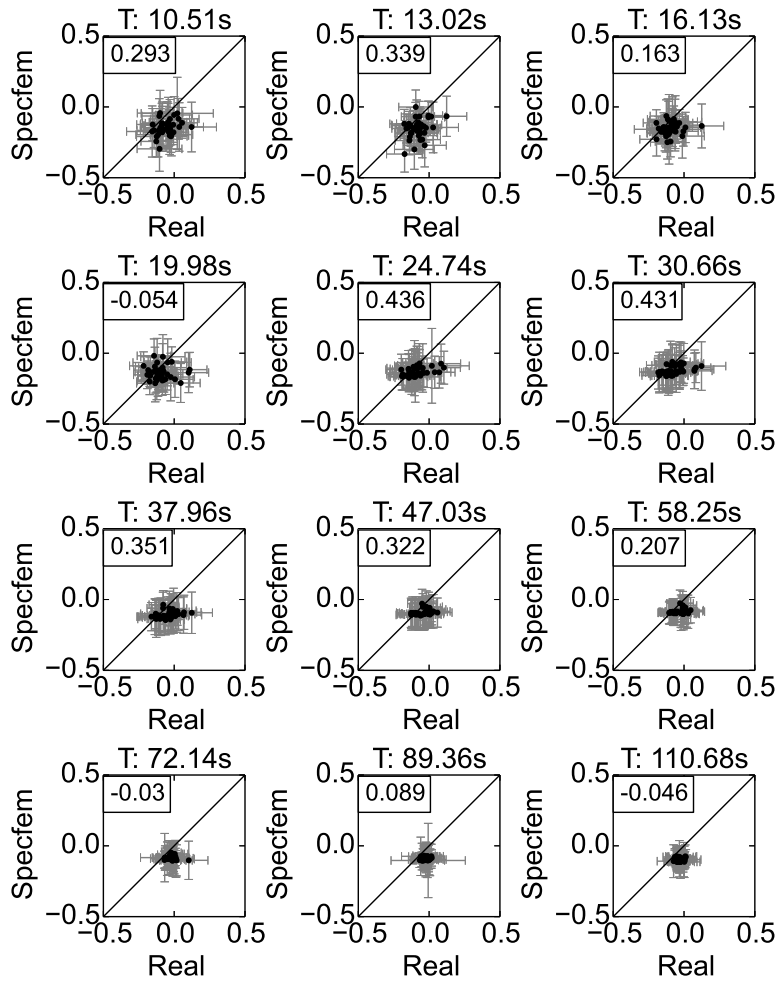


Figure 3.12: Comparison between ellipticity of synthetic seismogram computed with 3D model and real data. x and y error bars are from real measurements. In the boxes there is the correlation coefficient.

and 3.10, highlight that inversions of the observed H/V ratios for elastic structure as a function of depth should help refine Earth structure models of the study region. Nevertheless, it is important to bear in mind that these comparisons are only for one earthquake (due to the high computational cost of the SEM simulations accurate down to $T \sim 5.6$ s). Hence, probably part of the differences observed in these tests are mitigated by the fact that in real data applications a very large number of events along with strict data selection criteria are used to ensure stable measurements of H/V ratios.

3.5 Prograde Rayleigh wave motion

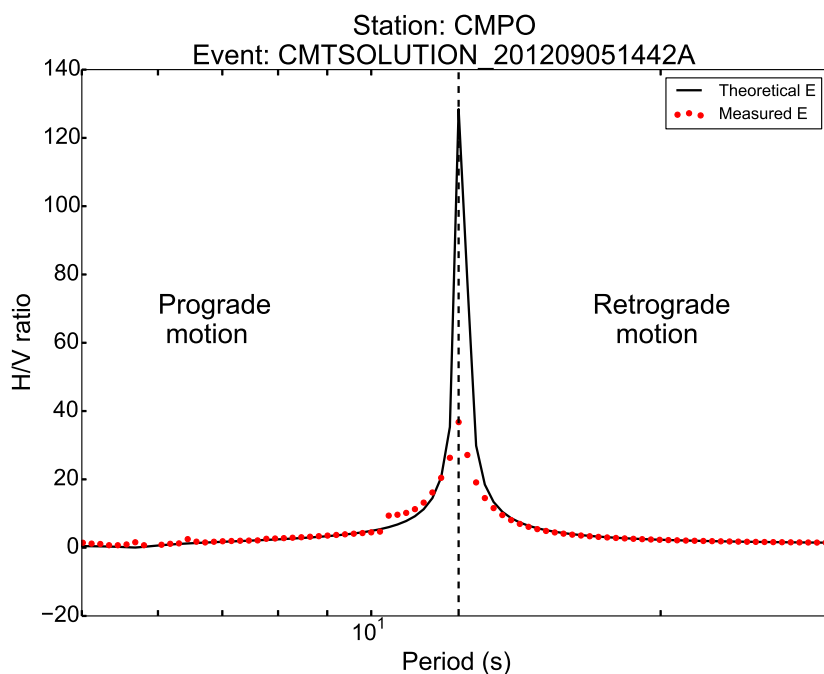


Figure 3.13: *Theoretical ellipticity curve (solid black line) compared to ellipticity measured on synthetic seismogram (red dots) computed for model MAMBo at station CMPO (for location, see Figure 3.2). The big peak at ~ 12.5 s corresponds to the transition between retrograde motion (on the right) and prograde motion (on the left).*

Rayleigh wave elliptical polarisation usually implies retrograde particle motion at the surface, but inverts polarity and becomes prograde at a certain depth. This behaviour can be seen theoretically for Rayleigh waves in a homogeneous half-space (e.g., Stein and Wysession, 2009). However, in some cases, it may happen that the Rayleigh wave fundamental mode shows prograde particle motion at the surface, e.g., when a very slow sedimentary layer is overlaid onto a faster crustal structure.

Tanimoto & Rivera (2005) studied this phenomenon with numerical simulations using a mode summation technique, and showed that such sign inversion of the elliptically polarised motion of Rayleigh waves may indeed take place near the surface in the period range 3.8 – 7.1 s for a sedimentary layer of 4 km. They also found a correlation between the thickness of the sedimentary layer and the period where the reversal begins: the thicker is the layer, the longer the inversion period is. No inversion has been found if the sedimentary layer is thinner than 2 km.

Since, on sedimentary basins, Rayleigh wave particle motion trajectories may transition to prograde polarity, we could potentially face measurement instabilities near the period corresponding to the transition from 'normal' (retrograde) to prograde motion in Po Plain stations. In order to investigate this issue, we compare theoretical ellipticity curves from the MAMBo model for stations in the Po Plain with values measured on synthetic seismograms computed by normal mode summation for the same model. In order to allow prograde motion to be detected, we modify our measurement algorithm to allow separation of retrograde from prograde motion, by considering for simplicity that prograde motion would show a cross-correlation equal to -1 (rather than $+1$), maintaining the usual (positive) phase shift.

Figure 3.13 presents the results of measurements on the mode summation synthetics for station CMPO. We notice a big peak in the theoretical curve at a period of about 12.5 seconds corresponding to the transition period between retrograde motion (on the right) and prograde motion (on the left). This also explains the very large predicted ellipticity values in the Po Plain seen in Figure 3.9. Measurements performed on the synthetics align along the theoretical curve, except for the amplitude of the transition peak, which corresponds to a singularity, and hence where the bigger mismatch occurs. Nevertheless, the overall behaviour of the theoretical curve is captured well, and gives us some clues on the expected behaviour for real data measurements.

We then calculate the theoretical transition period for the whole study area as expected by the MAMBo model, and shown results in Figure 3.14. The transition period is longer for stations on the plain than elsewhere, and no inversion from retrograde to prograde motion is predicted for periods $T > 1$ s for stations on hard-rock sites on the mountain chains, where the motion is always expected to be retrograde.

Figure 3.14 shows that the expected transition periods are in the range 2-16s with longer periods in the southern part of the plain, in a region parallel to the Apennines chain (around PRMA, CMPO, CAVE, MODE stations). In this area the sediments reach a thickness of 6 - 8 km (Molinari et al 2015). In such a geological setting the expected inversion periods of 10-13 s are compatible with the values

predicted by Tanimoto & Rivera (2005) for the Los Angeles basin, that has similar geological features, where they predicted the transition in the period range between 3 and 20s.

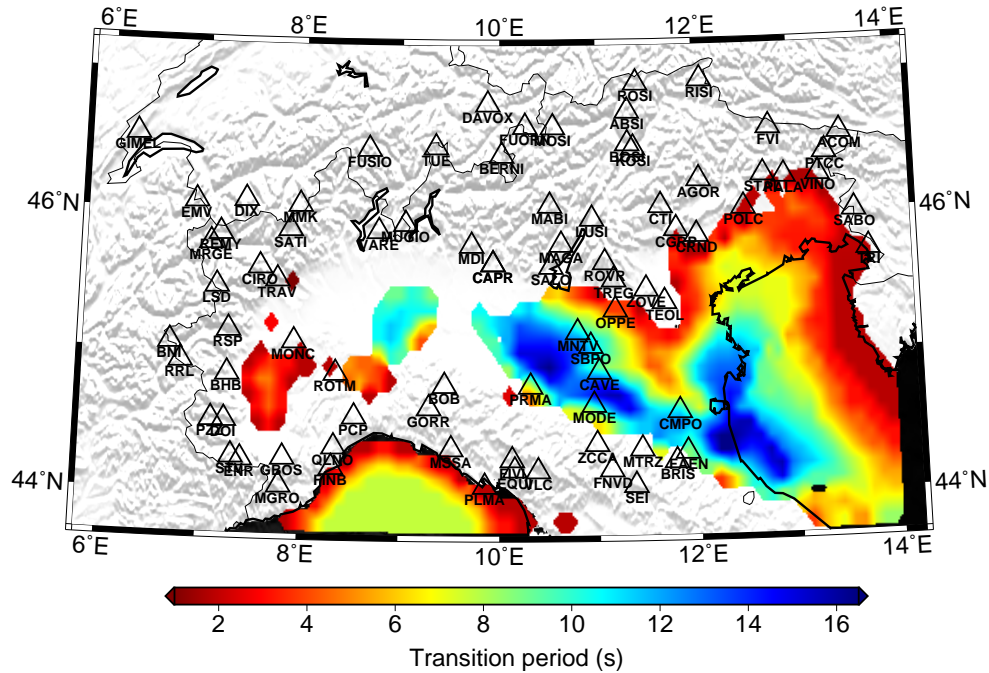


Figure 3.14: Map of the transition period between retrograde and prograde particle motion calculated on model MAMBo. In blank areas no transition is found for $T > 1$ s.

Finally, we measure ellipticity on real data for all the stations in the Po Plain separating retrograde from prograde motion in the same way as in the synthetic test explained above. For comparison, we also carry out the same analysis for station BNI in the Western Alps. Figure 3.15 compares histograms of the results for stations BNI and CMPO, the latter being located in the Po Plain (the results for the other stations in the Plain are similar to CMPO). Figure 3.15 shows that at CMPO for periods shorter than 13.3 s the detections of prograde motion on earthquake seismograms generally increase as the period decreases, where they are mixed with retrograde motion. This suggests that there may be an actual transition period around ~ 13.0 s, from which both prograde and retrograde motion can sometimes be detected. This agrees well with the transition period predicted by MAMBo (Figure 3.13). On the other hand, for station BNI there seems to be no transition to prograde motion down to 10 s. In both cases, it is difficult to measure ellipticity for shorter periods on earthquake data, because of the surge of microseismic noise where prograde and retrograde detections are mixed together (possible coherent noise

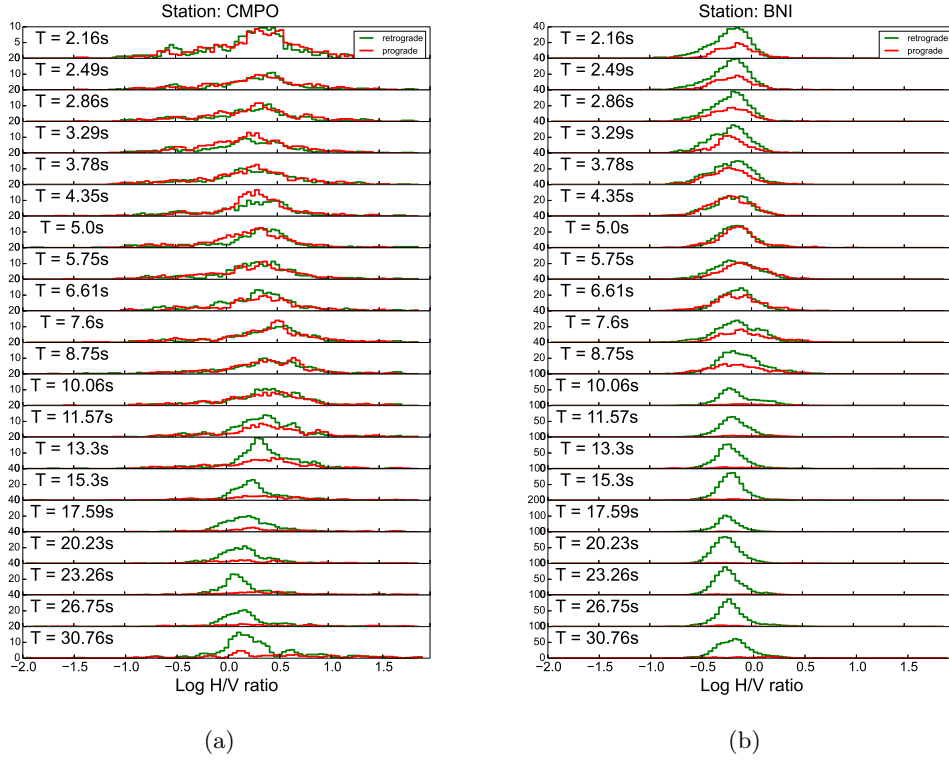


Figure 3.15: *Histograms of ellipticity measurements for station CMPO (a) and BNI (b). Green histograms represent the measurements of retrograde particle motion. Red histograms represents the measurements of prograde motion.*

wave trains may come from all azimuths, hence they present complete ambiguity on motion polarity). Moreover, the presence of ambient noise propagating in the same or opposite azimuth of the earthquake may also lead to detections of signals in the vertical component, which may reduce the measured H/V ratios. Hence, while these results suggest that for station CMPO we may have detected a transition period around 13 s, further work based on analysis of azimuthal distribution and polarisation of ambient noise signal is needed for firmer conclusions. (For time-domain waveforms recorded at station CMPO see figures 3.16 and 3.17.)

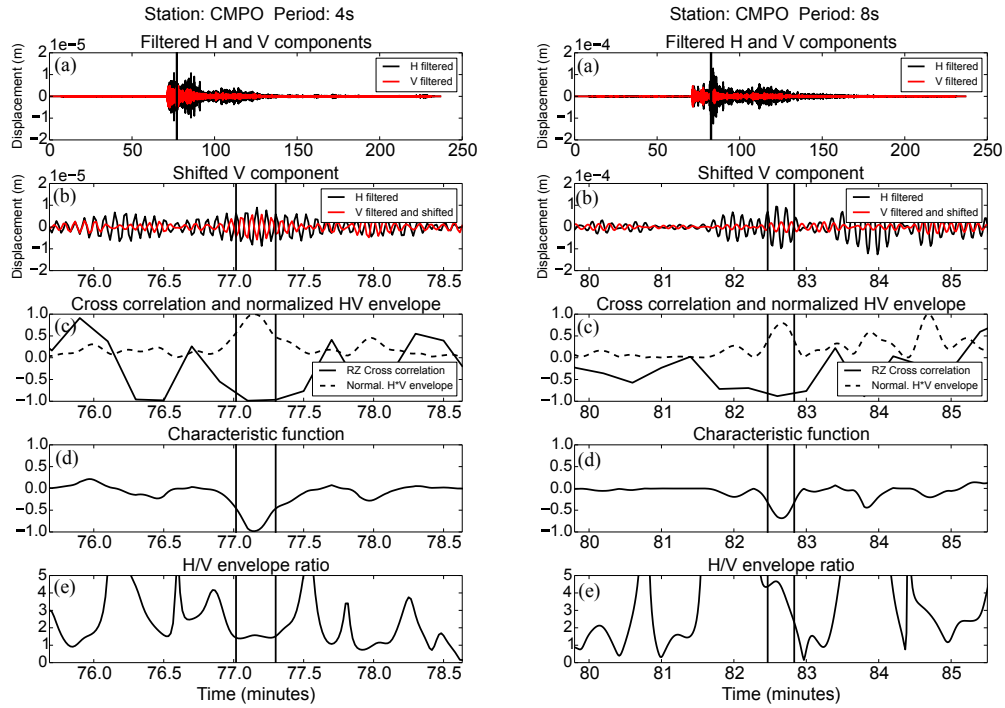


Figure 3.16: Measurement scheme for the March 11 2011 earthquake in the Tohoku region (Japan) (origin time: 05:46:23.00 UTC, $m_w = 9.0$) recorded at the station CMPO at a period of 4s (left) and 8s (right). (a) Full waveforms filtered with a narrow Butterworth-Bandpass filter. Vertical component is plotted in red, horizontal (radial) component is plotted in black. (b) Zoom of the waveform. Vertical component is shifted in advance by a 90° phase. (c) Cross-correlation between the de-phased vertical component and horizontal component (solid line) and normalized envelope of horizontal times vertical components. Negative cross-correlation indicates a prograde polarization of rayleigh waves. (d) Characteristic function, defined as the product of envelope and cross-correlation. (e) H/V ratio between the envelopes of horizontal and vertical component.

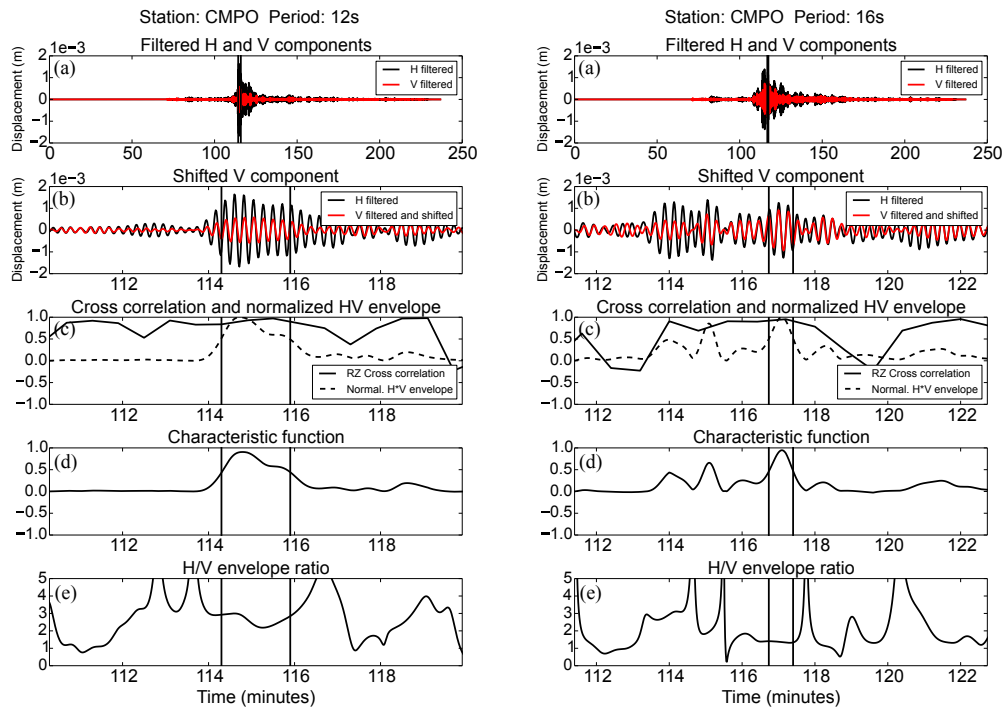


Figure 3.17: Measurement scheme for the March 11 2011 earthquake in the Tohoku region (Japan) (origin time: 05:46:23.00 UTC, $m_w = 9.0$) recorded at the station CMPO at a period of 12s (left) and 16s (right). (a) Full waveforms filtered with a narrow Butterworth-Bandpass filter. Vertical component is plotted in red, horizontal (radial) component is plotted in black. (b) Zoom of the waveform. Vertical component is shifted in advance by a 90° phase. (c) Cross-correlation between the de-phased vertical component and horizontal component (solid line) and normalized envelope of horizontal times vertical components. (d) Characteristic function, defined as the product of envelope and cross-correlation. (e) H/V ratio between the envelopes of horizontal and vertical component.

3.6 Discussion and Conclusions

We measured ellipticity H/V of Rayleigh waves in Northern Italy in the period range 10-110s using an automatic scheme that showed good capability of detection and separation of fundamental mode of Rayleigh waves from the rest of the signal. A large volume of high-quality teleseismic recordings in 2008-2014 has been used and we investigated potential horizontal component misalignments in the seismic stations used, which were found to be negligible.

Rayleigh wave ellipticity is sensitive to shallower structure than phase and group velocity for the same period. It is mostly sensitive to v_S , but it is also sensitive to v_P and density. However, the dependence of ellipticity on earth structure is more complex than that of phase or group velocity, because sensitivity kernels change sign with depth. Sensitivity to v_S is typically negative near the surface and becomes positive deeper in the crust, with a zero-crossing at some depth that depends on the wave period (Figure 2.1). Hence, a shallow fast v_S anomaly generates a low ellipticity value, whereas the same fast anomaly at greater depths leads to a high ellipticity value.

Our new measurements of H/V ratios show a good spatial coherency and excellent correlation with geological features, and exhibit small-scale variations, possibly highlighting small-scale heterogeneity. Locations of high ellipticity correspond to regions of low velocity in the Po plain sedimentary basin. Conversely, seismically faster hard rock regions in the Alps and Apennine mountain ranges show lower ellipticity values. Moreover, the observed ellipticity values also relate to the thickness of the basement, as highlighted by differences in observations beneath the Alps and the Apennines, notably for wave periods of $T \sim 37$ s.

Comparisons between observations and predicted H/V ratios for the MAMBo model show a reasonable agreement in terms of the first order patterns, particularly for the longest period data ($T \sim 37$ s). For the two shortest wave periods considered ($T \sim 10$ s and 16s), the predictions for the Po Plain are larger than the observations by a factor of four or more. This is due to the fact that for $T \sim 10-13$ s MAMBo predicts an inversion from retrograde to prograde Rayleigh wave particle motion at the surface in the Plain, where the vanishing amplitude of vertical component of motion leads to a singularity in the ellipticity, and hence to very large predicted values. Analysis of real data from the Plain allowing the detection of both retrograde and prograde surface wave particle motions suggests possible detection of prograde particle motion. However, the mix of weak teleseismic earthquake signals with ambient noise at the predicted transition periods complicates the interpretation of the results. Future work should be carried out analysing the polarisation and ellipticity of both earthquake and ambient noise data, including azimuthal analyses,

which are beyond the scope of this study. Nevertheless, when robust detections of inversion periods are confirmed, they could provide key information about the structure of sedimentary basins, notably about their thickness.

In order to test whether ellipticity depends only on the structure beneath the receiver station for realistic 3-D Earth models, we use our technique to compute Rayleigh ellipticity using accurate theoretical seismograms calculated using the Spectral Element Method for a recent 3-D mantle model and a global crustal 3-D Earth model. Our results show an overall good agreement between the measurements on the 3-D synthetics and the ray theory, local receiver structure predictions, within the measurement errors. These tests help us further validate our technique. A significant step of the Moho under the Northern Apennines has been shown to reflect laterally surface waves in the 15-20 s period band (Stich and Morelli, 2007) and has been imaged from time reversal of reflected surface waves along the axial zone of the mountain chain (Stich et al., 2009). Such a strong and sharp lateral gradient of structure could possibly perturb ellipticity measurements, but we find no clear indication of that in our measurements. However, actual sensitivity of elliptical polarisation parameters in situations far from a flat layered medium, or its smooth perturbations, still have to be explored in detail.

Besides an overall fair agreement between theoretically predicted and observed values, we also image geographically coherent deviations from expectations. This makes us conclude that ellipticity may indeed represent an appropriate tool for improving knowledge of shallow crustal structure. The strong non-linearity of its dependence, represented by highly variable sensitivity kernels, may grant resolution, but make the inversion more complex. Joint inversion with other observables — such as surface wave group and phase velocities, or body wave receiver functions — may result beneficial to this extent.

Acknowledgments. Data used in this study were collected from ORFEUS-EIDA Data Center and they have been provided by several networks: Italian National Seismic Network operated by Istituto Nazionale di Geofisica e Vulcanologia (<http://eida.rm.ingv.it/>): 47 stations. Province Südtirol seismic network operated by ZAMG - Central Institute for Meteorology and Geodynamics: 7 stations. North-East Italy Broadband Network (OGS and University of Trieste, 2002): 8 stations. Switzerland Seismological Network (<http://www.seismo.ethz.ch/>): 9 stations. Med-Net Project (<http://mednet.rm.ingv.it/>): 5 stations. Regional Seismic Network of North Western Italy (University of Genova, 1967): 19 stations. Data analysis and measurements have been performed using ObsPy (Beyreuther et al., 2010, Megies et al., 2011, Krischer et al., 2015). A.M.G.F. thanks funding by the Fundacao para a Ciencia e Tecnologia (FCT) project AQUAREL (PTDC/CTE-

GIX/116819/2010) and computing time in the UK supercomputer Archer.

Chapter 4

Inversion for shear-wave velocity

4.1 Inversion technique

As we have seen in the previous chapter, ellipticity shows a highly non-linear behaviour. This is evident looking at the v_S sensitivity kernels (fig.2.1): they depend on the local structure, and they change sign at a relatively shallow depth, so that, say, a low-velocity layer may cause positive or negative H/V change depending on the actual (unknown) velocity profile. For this reason we must use a complete non-linear inversion technique to obtain v_S profiles from ellipticity curves. Therefore we follow a Monte Carlo approach, in particular we employ the neighbourhood algorithm. This method, implemented by Sambridge (1999), samples the model space iteratively in a very efficient way: in the first stage the system pick randomly a set of models inside the parameter ranges set by the user. For every model it solves the forward problem, calculating the theoretically-expected observations (for us, a theoretical ellipticity curve found by modal summation, following Herrmann, 2013) and compares them with the observed data to calculate the misfit between observed and synthetic data. The best models found are then used to re-sample the model space iteratively, re-sampling at every step around the best models found. The final ensemble of models will be denser around the best model found.

4.1.1 Forward problem

We calculated the theoretical ellipticity curve for each model sampled by modal summation using the algorithm implemented by Herrmann (2013). This fast and efficient algorithm uses a 1D flat layered model to calculate the eigenfunctions at the receiver. As we have shown in the previous chapter, we can consider that ellipticity

of the fundamental mode only depends on the structure at the receiver, without the need of a modelisation of the structure at the source and along the wave path.

4.1.2 Cost function

The inversion process is based on the minimisation of a cost function, that indicates the ability of a model to fit the observed data. Minimising the distance, in data space, between observed and theoretical values using the L^2 norm can lead to unrealistic results, with rough models showing too large variations between adjacent layers and v_S decrease with depth. This behaviour is common in solving inverse problems and is due to under-determination: many models fit the data equally well or, however, within data errors. A possible and well known solution to this issue consists of searching only relatively smooth models, under the assumption that they are more realistic and simpler, hence preferable on the basis of Occam's rule (Constable et al., 1987). We implement this condition by adding a term to our cost function, expressing a will to also keep model roughness (represented by its curvature) minimum when fitting observed data:

$$c = \sqrt{\sum_{i=1}^N \frac{(d_i - g(m)_i)^2}{\sigma_i^2}} + A \sum_{j=2}^{P-1} (v_s(j-1) - 2v_s(j) + v_s(j+1))^2 \quad (4.1)$$

Here N is the number of measurements, d_i is the observed data, $g(m)_i$ is the theoretical ellipticity value for the m model, A is a scale factor, P is the number of parameters and v_S is the shear-wave velocity. The first term is the misfit between observed and synthetic data. The second term represents the model roughness, as the norm of its second derivative implemented by a finite-difference operator. The scale factor, A , needs to be chosen. There may be different ways to find the most appropriate value for A (the original implementation of Occam's razor searches the smoothest model that fits data within data errors) but for this experiment we easily find a best value so that the models attain good fit to the data without unrealistic oscillations.

4.2 Parameterisation

To calculate the theoretical ellipticity curve we need to parametrise the crust as a layered model with flat, parallel, laterally uniform, isotropic layers. We chose a simple parametrisation based on the one proposed by Lin et al 2012 (see tab. 4.1). Thickness of the layers are fixed because ellipticity has a weak sensitivity to layers' thickness. We inverted v_S only and calculate v_P and density as a function of v_S

Layer	Thickness (km)	V_s
1	3+elevation	Inverted (gradient)
2	8	Inverted (gradient)
3	[Moho - (thick 1 + thick 2)]/2	Inverted
4	[Moho - (thick 1 + thick 2)]/2	Inverted

Table 4.1: *Parameterisation of the crust used in the inversions. v_P and density are calculated from v_S by Brocher relations (Brocher 2005)*

by empirical relations (Brocher 2005). We parameterised v_S in the first two layers with a gradient and we inverted for the v_S at the top and at the bottom of the layers. Third and fourth layers have constant v_S . We fixed the moho depth to the value of Epcrust (Molinari 2011) and we used for the upper mantle the values of Epmantle (Schivardi 2011). We also take into account the altitude of the stations increasing the thickness of the first layer by the elevation value.

4.3 Synthetic test

To verify the ability of the inversion algorithm to select the best models and to validate the parameterisation chosen we first perform a synthetic test. We select a "true" complex model and we calculate an ellipticity curve. Then we use the synthetic curve as observed data and invert it using the technique described before. In fig.4.1 we show to the left the best models found (red profile) compared to the true model (green profile). All the models sampled are plotted in light grey. Models that fit the data within 10 times the best cost function found are plotted in darker grey. To the right we show the "observed" data (black circles) compared to the ellipticity curve for the best model found (red line) and the ellipticity curve from models with cost function down 10 times the best one. We conclude that our non linear inversion scheme is indeed able to reconstruct the model that originated a given ellipticity curve. The neighbourhood algorithm explores a wide model space and indicates, as a result, a rather narrow domain of acceptable models, very close to the true one.

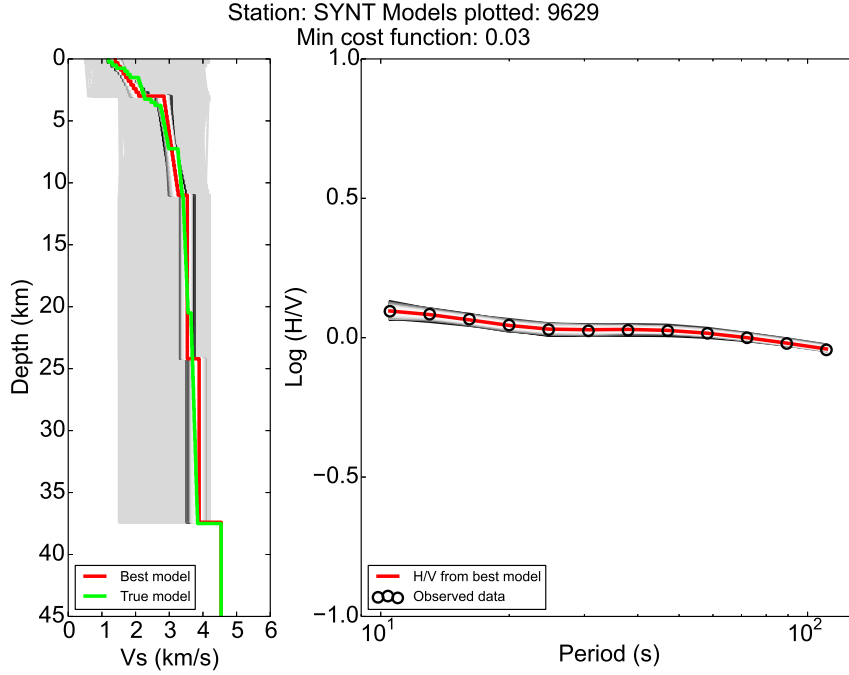


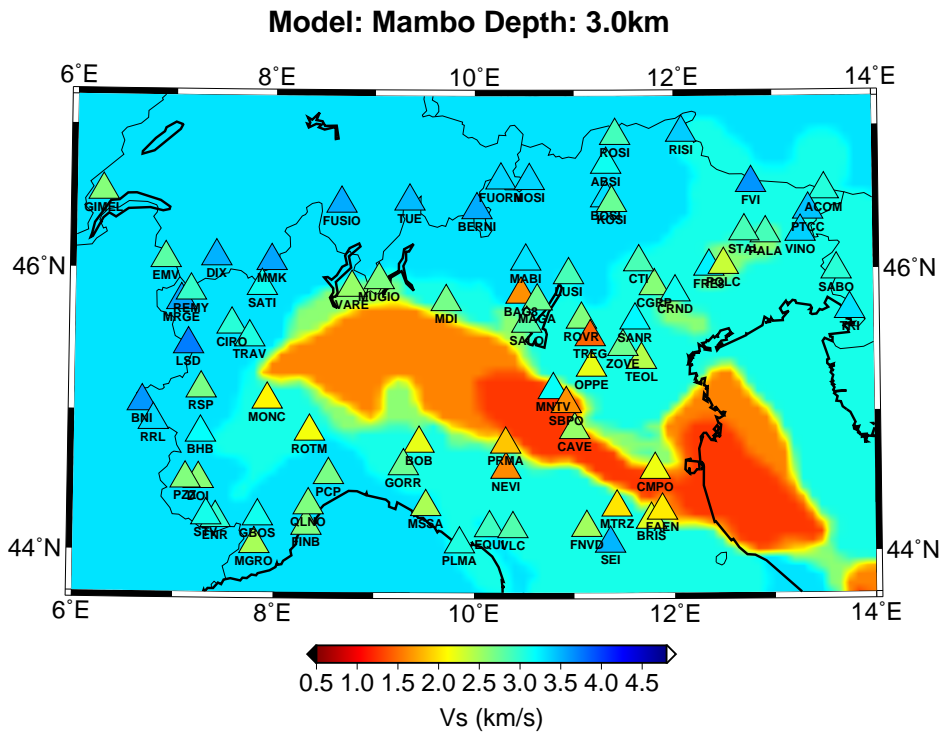
Figure 4.1: *Synthetic test results. On the left: best v_S profile found (red line) compared with the true model used for the test (green line). Gray lines are all the model sampled during the inversion procedure. On the right: "observed data" obtained from the true model (black circles), H/V calculated from the best model found (red line).*

4.4 Inversion results

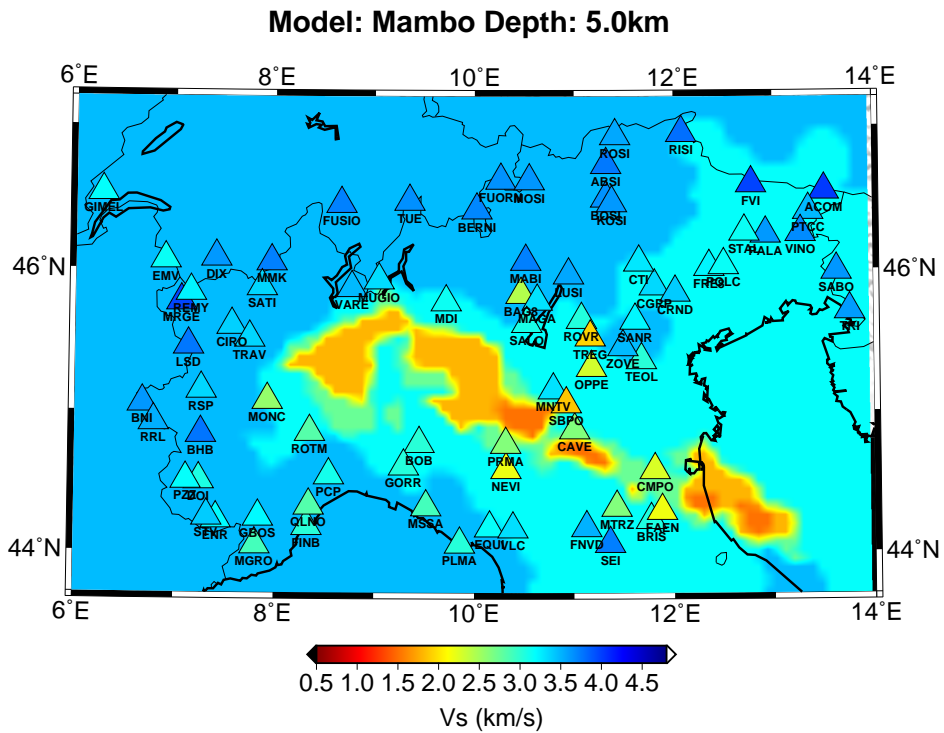
We inverted the ellipticity curve for stations in northern Italy (see previous chapter) using the inversion technique described before. We obtain a v_S profile for each station and we compare them with the most recent models available for this region: MAMBo (Molinari et al 2015a) and MOL15 (Molinari et al 2015b). For details about the models see chapter 1.

In fig.4.2a and b we show as an example the results for two station, CMPO, in the center of the Po Plain and BNI, in the western Alps. The best model found in the inversion is plotted in red, model MAMBo is plotted in blue, MOL15 in green. We also show in shadows of grey the models that obtained a cost function up to 10 times the best one. CMPO results show a very good agreement between our results and MAMBo model at the shallowest depth, down to 4 km. At larger depths our results are slower than the values predicted by MAMBo. Conversely, comparing with MOL15, we see a bad agreement at shallow depth, down to 7 km and a better agreement between 7 and 37 km. We may point out that model MOL15 is the result of inversion of surface-wave dispersion data, that may not have best

sensitivity to the shallowest few km of the structure, and may be considered more reliable at lower-crustal depths. BNI shows in general a better agreement between the three models. This is probably due to the simpler structure of the Alps where no sedimentary layer at the surface. The three models are mostly flat and the predicted ellipticity curves do not show great differences with the observed data. We show in fig.4.3 and 4.4 and fig.4.5 and 4.6 the inversion results for all the stations used in this study at four depths, compared with the values of MAMBo and MOL15 respectively.

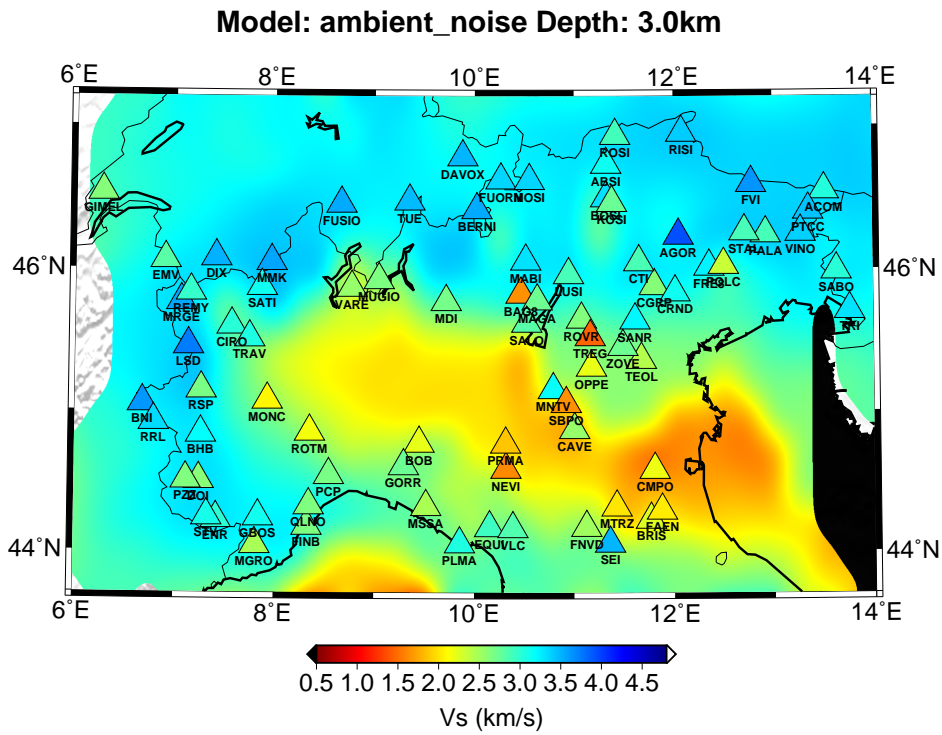


(a)

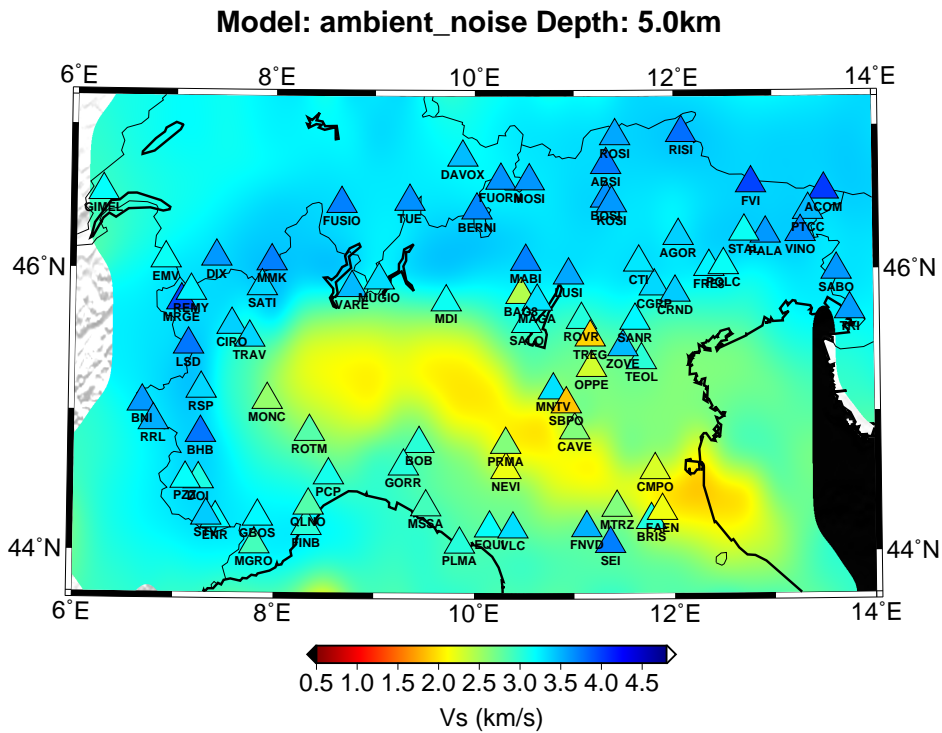


(b)

Figure 4.4: *Triangles: v_s of the best model found for each station at different depths. Background: map of v_s from MAMBo model at the same depth.*

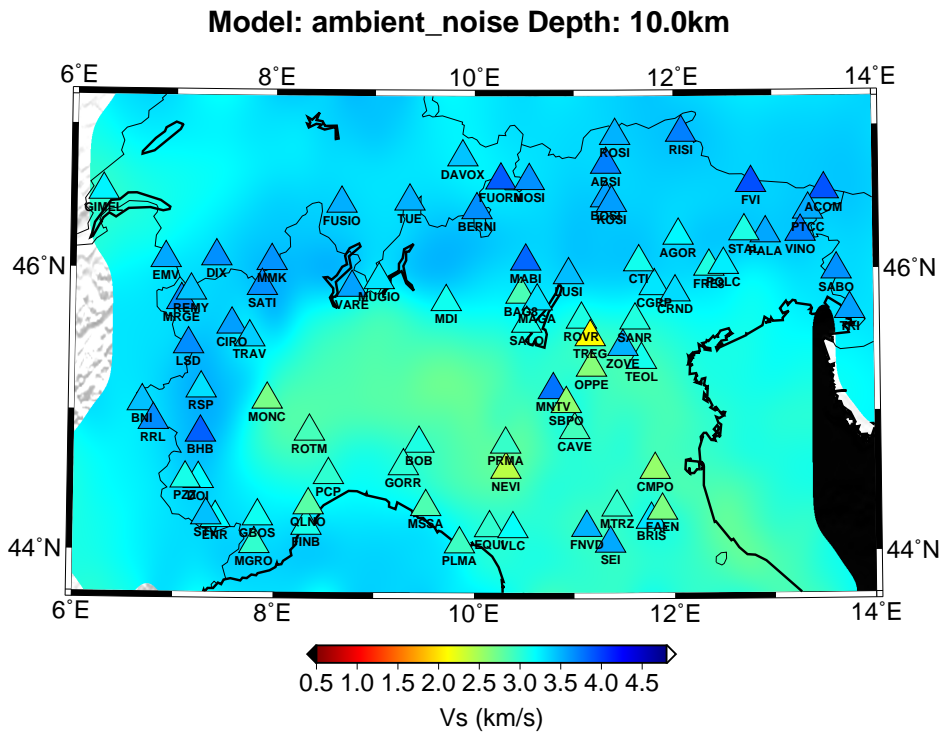


(a)

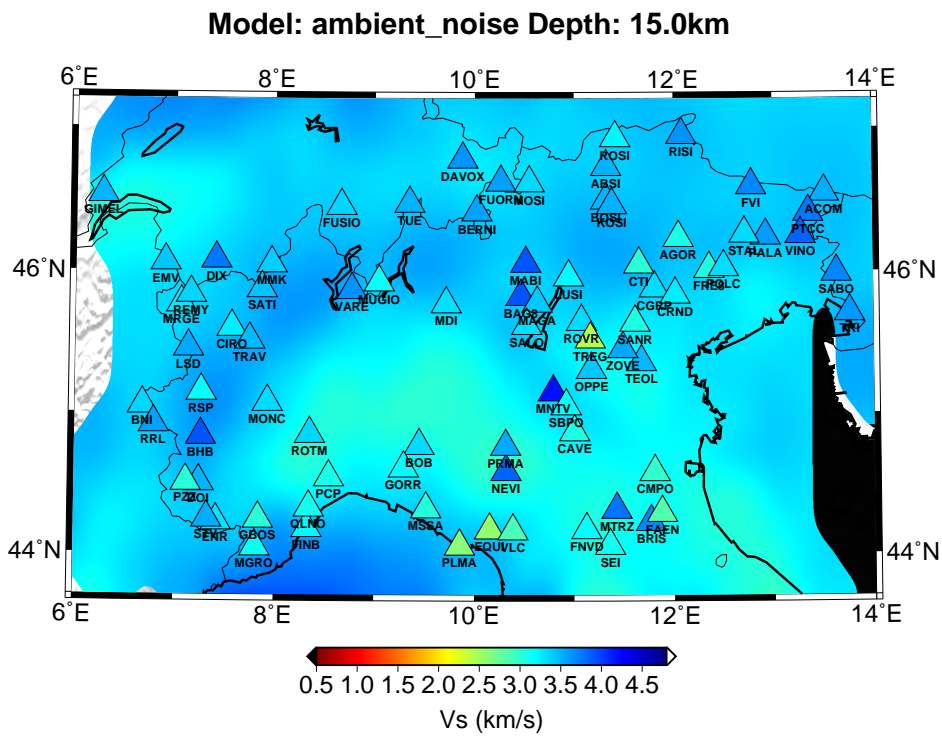


(b)

Figure 4.5: *Triangles: v_s of the best model found for each station at different depths. Background: map of v_s from MOL15 model at the same depth.*

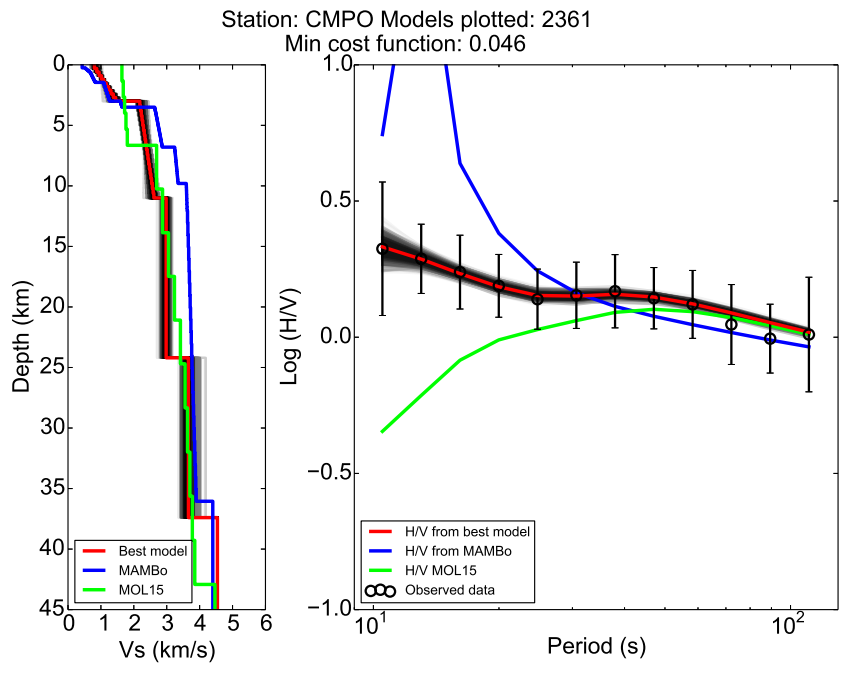


(a)

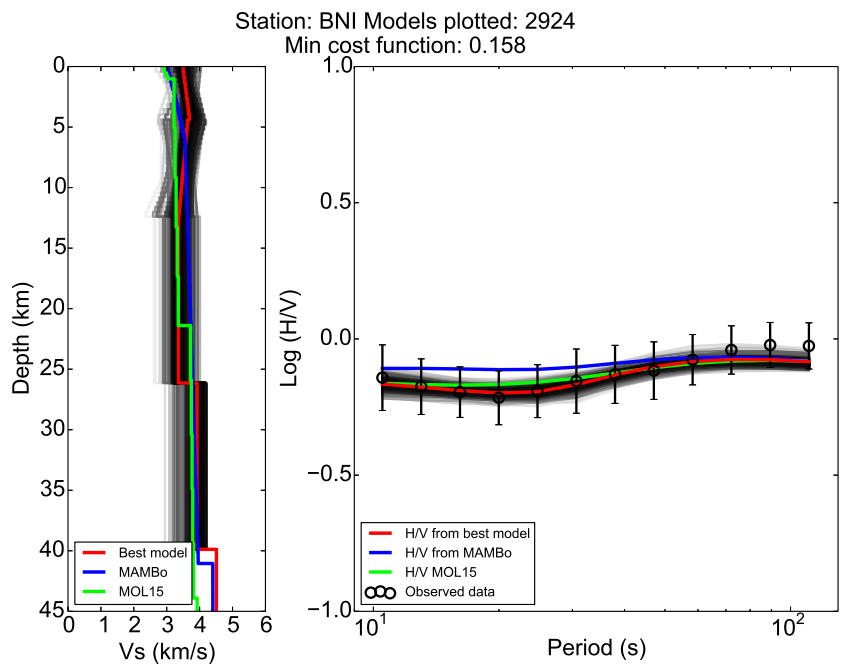


(b)

Figure 4.6: *Triangles: v_s of the best model found for each station at different depths. Background: map of v_s from MOL15 model at the same depth.*

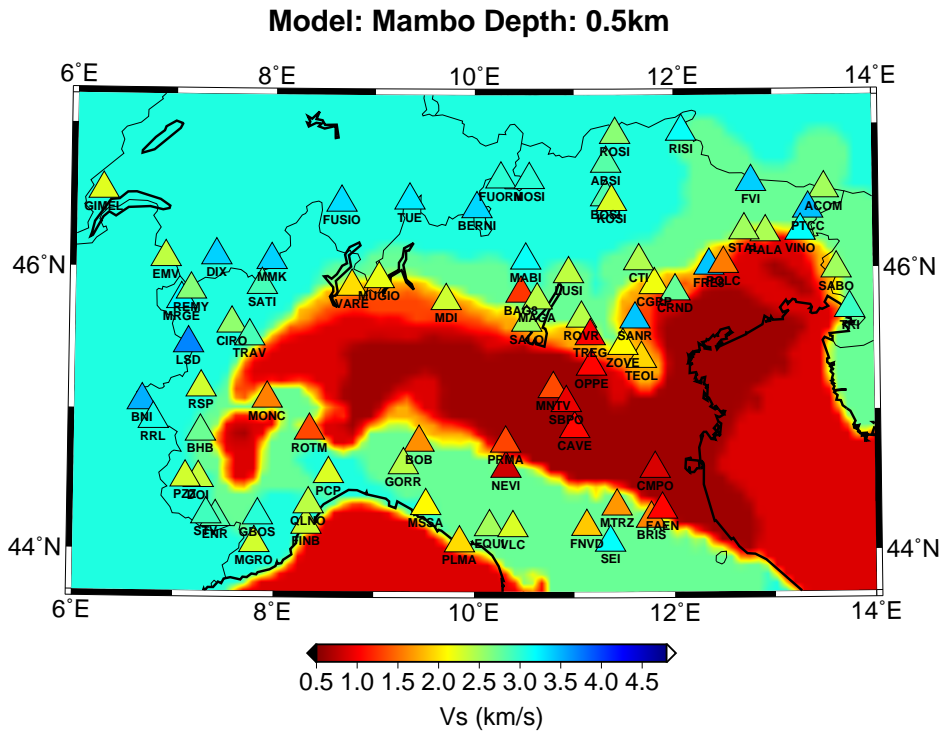


(a)

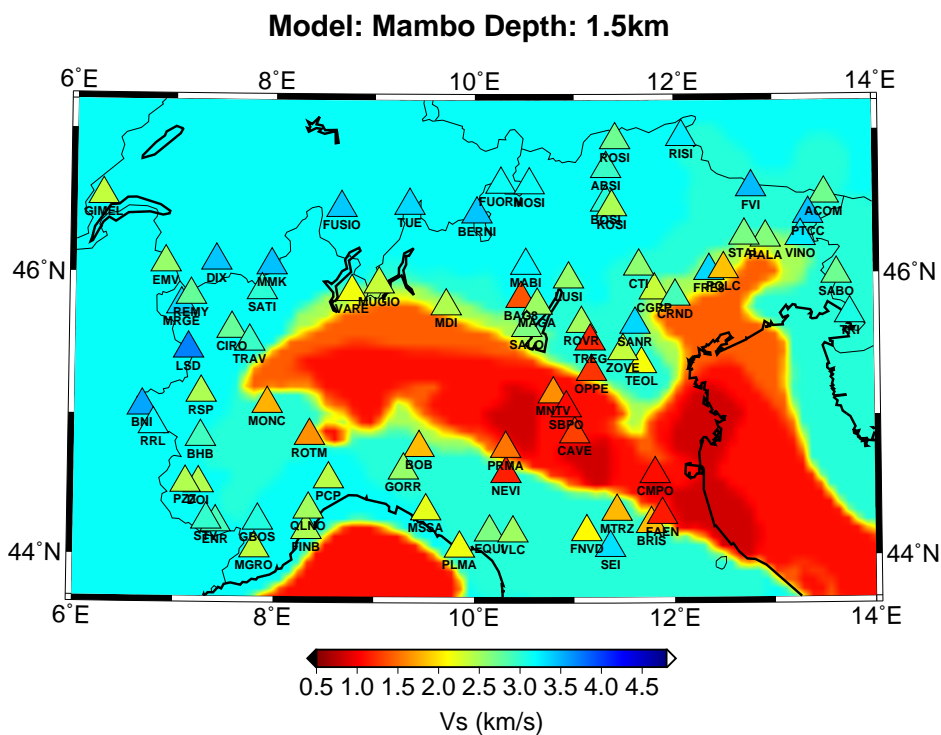


(b)

Figure 4.2: Best model found for station CMPO (a) and BNI (b) compared with MAMBo model (blue line) and MOL15 (green). Gray models are all the models sampled with cost function up to 10 times the best one.



(a)



(b)

Figure 4.3: Triangles: v_s of the best model found for each station at different depths. Background: map of v_s from MAMBo model at the same depth.

4.5 Discussion and conclusions

Results plotted in fig.4.3 and 4.4 show that for small depth there is a good agreement between v_S obtained in the plain and reference MAMBo values. Slow velocities of ≈ 0.5 -1.0 results at 0.5 km depth for station CMPO. At this depth values slightly higher than expected result for stations CAVE, SBPO, MNTV and OPPE, in the central part of the plain. A similar trend is observed at 1.5 km depth. At larger depths it becomes evident that stations on the Apennines show a generally lower v_S than stations on the Alps. This is probably due to the different geology of the two chains: Apennines are composed mostly by metamorphic and compact sedimentary rocks while Alps are made of granite-crystalline rocks. It is also notable that at 3 and 5 km depth stations on the southern part of the Alps show a slower v_S than northern (and higher) Alps. This is probably due to the different composition of the geological structure of the Italian Prealps, made of sediments and metamorphic rocks.

Looking at the comparison with ambient noise model in figure 4.5 and 4.6, we notice that the minimum depth described by the model is 3 km because of the deeper sensitivity of phase velocity used in the tomography. We can notice also that model MOL15 is much smoother than MAMBo, because it has a regional scale covering the whole Italian territory with a resolution of $0.1^\circ \times 0.1^\circ$. Comparisons in this case should consider the difference in resolution: our ellipticity bring information on local, shallow, structure beneath each station, while MOL15 represents a smoother shear-wave velocity field best resolved at a larger horizontal scale and larger depth.

These results show good ability of the inversion to infer the shallowest part of the crust with a good fit with observed data. Resolution rapidly decreases at depth larger than 15 - 20 km. This simple parametrization with 4 layers permits a fast and efficient Monte Carlo inversion, with the Nearest Neighbourhood sampling technique, with very short computational time (≈ 10 minutes in a small cluster with 20 CPUs).

Because of its strong shallow sensitivity ellipticity measurements appear to be a good tool to update and calibrate the pre-existing model MAMBo, that has a very detailed layer structure. But we need to find a more appropriate parameterisation, than the one used here to derive velocity profiles. Also, velocities profiles beneath each station refer to totally different geological structures, from the sedimentary basin of the plain to the crystalline rocks of the Alps. It would not be realistic to just interpolate shear-wave velocity between stations, at each depth, without any account for known geological structure. We therefore choose to change the setting of the inversion using exactly the same layered structure of MAMBo and modify the seismic parameters inside each layer.

Chapter 5

Calibrating MAMBo with Rayleigh ellipticity: inversion with shape constraints

5.1 Introduction

In the previous chapter we used a simple parameterisation of v_S as a function of depth to invert ellipticity curves. Such a simple scheme was a good pilot study to evaluate the ability of H/V measurements to retrieve information on the shallow structure of the crust, but it is not functional for building a new crustal model. The study region has a very complex shallow structure and it cannot be described using a simple 4-layers scheme. The Po Plain is made by the superposition of a number of sedimentary layers, from the shallowest most recent loose sediment layer to the oldest, more compact mesozoic layer. The use of the same parameterisation beneath all the stations can not give the possibility of any interpolation between them: For example two stations, one located on the plain and one on the mountain, will give information on v_S at a certain depth, but the information will be related to different geological structures and they cannot be interpolated to obtain a continue information between them. We then choose to start from a previous 3D model of the plain, MAMBo (Molinari et al 2015), and update it using the information given by the ellipticity measurements, but keeping the same parameters (and volume shapes) as in the original model. Velocities in MAMBo layers only depend on depth on the basis of pre-assigned profiles: we build here also lateral variations (see chapter 2). In this chapter we describe in detail the MAMBo model and the updating procedure by the inversion of ellipticity curves.

5.2 MAMBo model

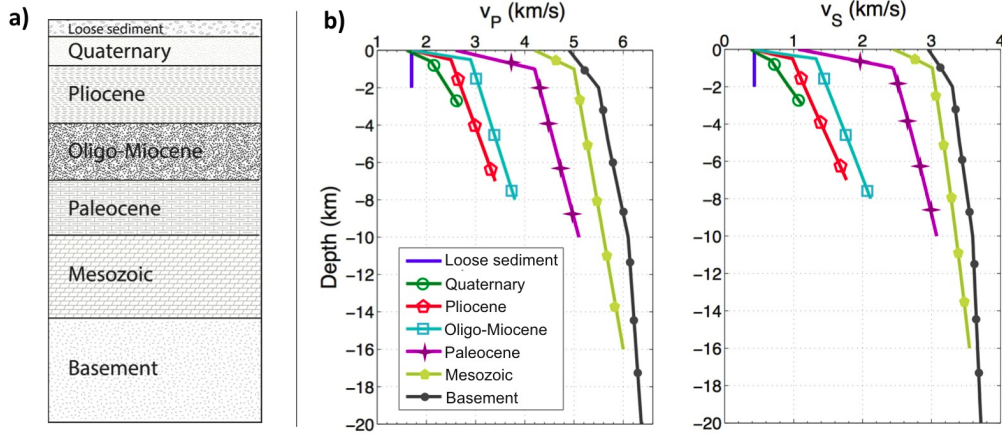


Figure 5.1: Picture from Molinari *et al.*, 2015b. a) stratigraphic column of the Po Plain. b) Gradients of v_P and v_S relative to each stratigraphic layer.

The seismic model MAMBo covers a region of around 600 km by 300 km in northern Italy. It describes with a resolution of 1 km the Po Plain area and the surrounding regions. It is made of a maximum of 6 superposed sedimentary layers lying on a crystalline basement: they are named Loose sediments, Quaternary, Pliocene, Oligo-Miocene, Paleocene and Mesozoic, from the shallowest and most recent to the deepest and oldest. The stratigraphic column is shown in Figure 5.1a. The thickness of each layer varies laterally but it could also be equal to zero when the layer does not exist. Together with the high-resolution geometrical description of the layers of the plain (called “objects”), the model is made of an ensemble of “rules” giving the velocities and density gradients inside each layer (Figure 5.1b). All the geological layers but the loose sediment one, have a simple velocity profile with two linear slopes. The shallower gradient is higher than the lower because seismic velocities and density increase more rapidly at shallower depth. These gradients have been derived by laboratory studies and empirical measurements (Brocher, 2005) and, within each layer, they do not change with geographical position. Consequently inside each layer there will not be any lateral variation at a certain depth. The lateral variations of seismic parameters in the earth’s crust will only be given by the different layer structure. In this study we have used the same layered structure as MAMBo and we inverted ellipticity curves to gain information about lateral variations of the rules associated to each layer.

5.3 Inversion

For each station we invert the ellipticity data shown in chapter 2 using the same non-linear technique described in the previous chapter. For each station we use the layer structure by MAMBo and we invert for the shear-wave velocities inside each layer. We keep the slope coefficient unchanged because ellipticity did not show a high sensitivity to it, especially for very thin layers. We then scale proportionally the shear-wave velocity profile by the same factor, changing the intercept parameters q_1 and q_2 . For each iteration we calculate the theoretical ellipticity curve expected for the model sampled and we compare it with the observed data. Assuming Gaussian uncertainty in measurements, represented by uncorrelated variances σ_D^i for measurements $i = 1, \dots, N$, and a similar Gaussian uncertainty on the a priori model MAMBo, represented by uncorrelated variances σ_M^j on model parameters $j = 1, \dots, P$, the classical least squares solution is found by minimising the cost function (Tarantola, 2005):

$$\|g(m) - d\|_{C_D^{-1}}^2 + \|m - m_{prior}\|_{C_M^{-1}}^2 \quad (5.1)$$

(where diagonal matrices C_D^{-1} and C_M^{-1} are formed by σ_D^i and σ_M^j respectively), that can be simplified as:

$$c = \sqrt{\sum_{i=1}^N \frac{(g^i(m) - d_{obs}^i)^2}{\sigma_D^i{}^2}} + \sqrt{\sum_j^P \frac{(m^j - m_{prior}^j)^2}{\sigma_M^j{}^2}}$$

Where $g^i(m)$ is the expected value for the sampled model calculated by modal summation, d_{obs}^i is the observed data, σ_D^i is the error associated to the measurement. The first part defines the misfit between observed data and expected values for the model sampled while the second part defines the difference between the model and the a priori model. During the inversion process the system will minimise the cost function and it will produce an ensemble of models that fit the dataset. As before, to tackle the non-linearity of the functional $g(m)$, we use the neighbourhood direct-search method (Sambridge, 1999) to sample the model space.

5.4 Results

We show in detail results for stations CMPO and PRMA. The first is in the eastern part of the plain, close to the Adriatic Sea, the second in the center, close to the southern edge of the plain. In fig. 5.2 and fig. 5.3 on the left we see the best model found (solid line) compared to MAMBo model (dashed line) in grey we show all the models sampled. On the right hand side we show the observed data with error bars

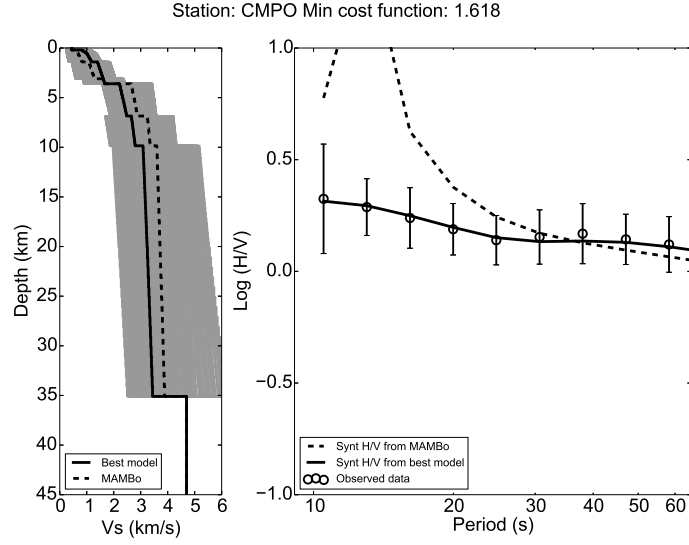


Figure 5.2: *Inversion results for v_S velocity for station CMPO. On the left: best model found (black line) compared to MAMBo (dashed line). In gray all the models sampled during the inversion process. On the right: observed data (black circles with error bars) compared to H/V synthetic values from MAMBo (dashed line) and H/V synthetic values from best model found (black solid line).*

and the synthetic data for both MAMBo (dashed line) and best model found (solid line). CMPO best model shows a faster structure than MAMBo down to around 4 km and a slower v_S in the deeper crust. For station PRMA we notice a similar shape, with faster layers on the top of the profile and slower v_S below. For both stations H/V values predicted by MAMBo are much higher than the observed data. This is due to the instability of H/V around the polarization inversion period, as we explained in chapter 2, where relatively small changes in structure may result in very different polarisation characters.

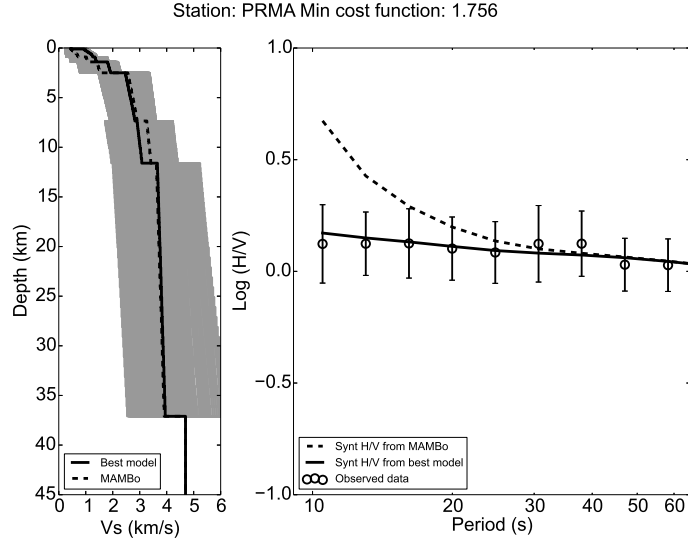


Figure 5.3: *Inversion results for v_S velocity for station PRMA. On the left: best model found (black line) compared to MAMBo (dashed line). In gray all the models sampled during the inversion process. On the right: observed data (black circles with error bars) compared to H/V synthetic values from MAMBo (dashed line) and H/V synthetic values from best model found (black solid line).*

5.5 MAMBo-E

We applied the inversion scheme to all the stations available and we obtained an updated shear-wave velocity profiles beneath each station, through adjustments of the original parameters. We then interpolate the values obtained using a Ordinary Kriging scheme (Davis 2002). This interpolation technique is widely used in geosciences as it has been built to characterise geographic areas without information in the case of uneven distribution of geological data. We then build a new model putting together the MAMBo objects and the rules derived by the kriging interpolation of the inversion results. As a result a new model contains the same layers as before, but with lateral variations within each layer, as we show in fig. 5.4. We plot here the percentage variation of MAMBo-E as a respect to MAMBo.

The loose sediment layer (fig.5.4a) do not show a big difference to MAMBo, all the variations are smaller than 2.5%. This is probably due to the very small thickness of this layer that cause a very low sensitivity. We notice that for the Quaternary and Pliocene layers (fig.5.4b and c) v_S of MAMBo-E is in general faster then MAMBo with a variation of $\sim 10-25\%$. The central part of the plain, around MNTV, SBPO and CAVE stations is faster then the other part of the basin. The Oligo-Miocene layer (fig.5.4d) has very small variations with respect to MAMBo in the eastern part of the plain, while it is faster in the western part. The Mesozoic layer (fig.5.4e) has

a similar shape, with faster shear-wave velocity on the western-northern part of the plain and lower velocity on the eastern-southern part, possibly due to different composition of Alpine sediments that went into the sin-orogenic foreland basin. The magnetic basement layer (fig.5.4f) shows lower v_S under the plain, especially in the western area (around MONC and ROTM stations).

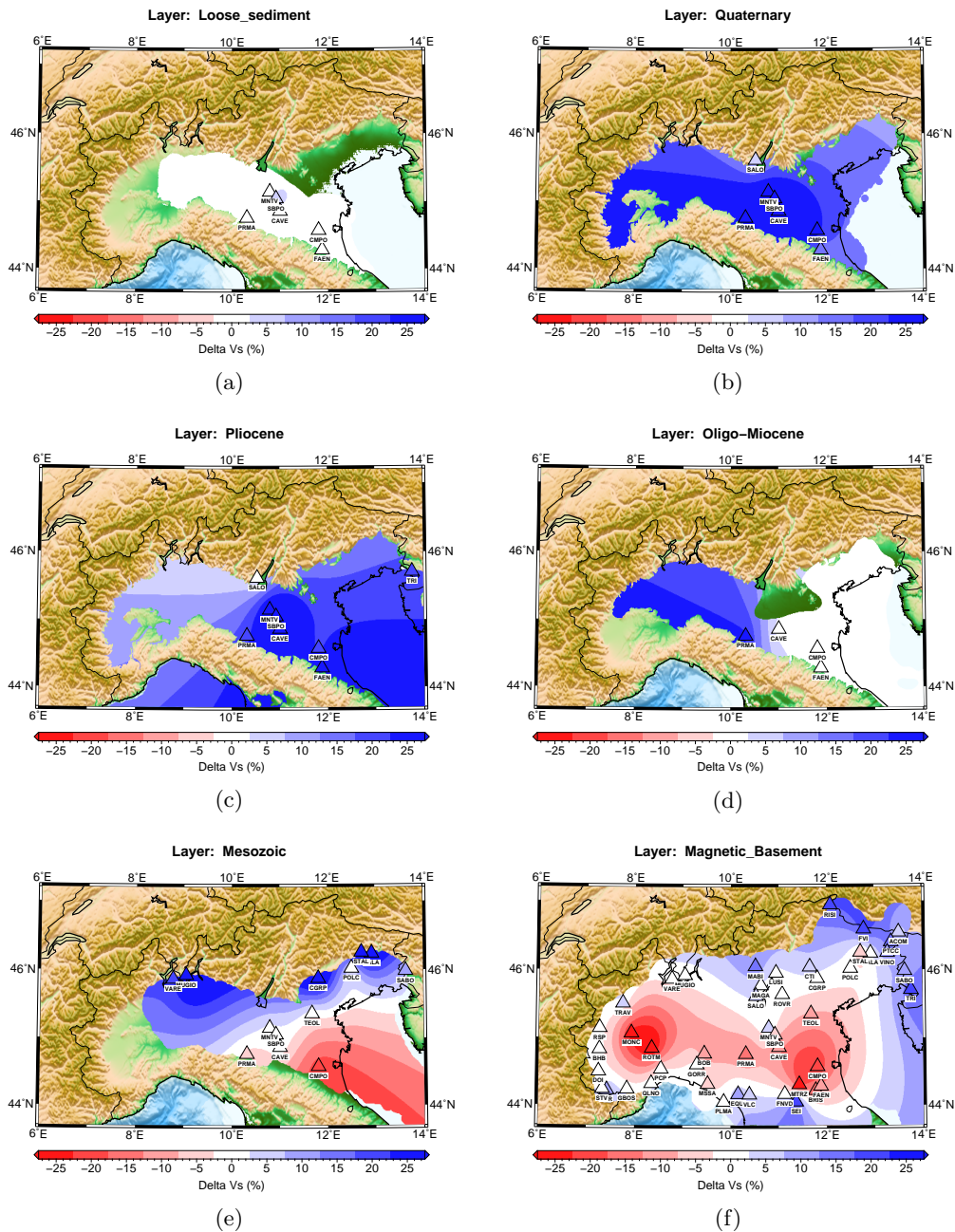


Figure 5.4: *Delta V_s between MAMBo-E and MAMBo for loose sediment layer (a), Quaternary layer (b), Pliocene layer (c), Oligo-Miocene layer (d), Mesozoic layer (e) and magnetic basement (f)*

5.5.1 Vertical cross-sections

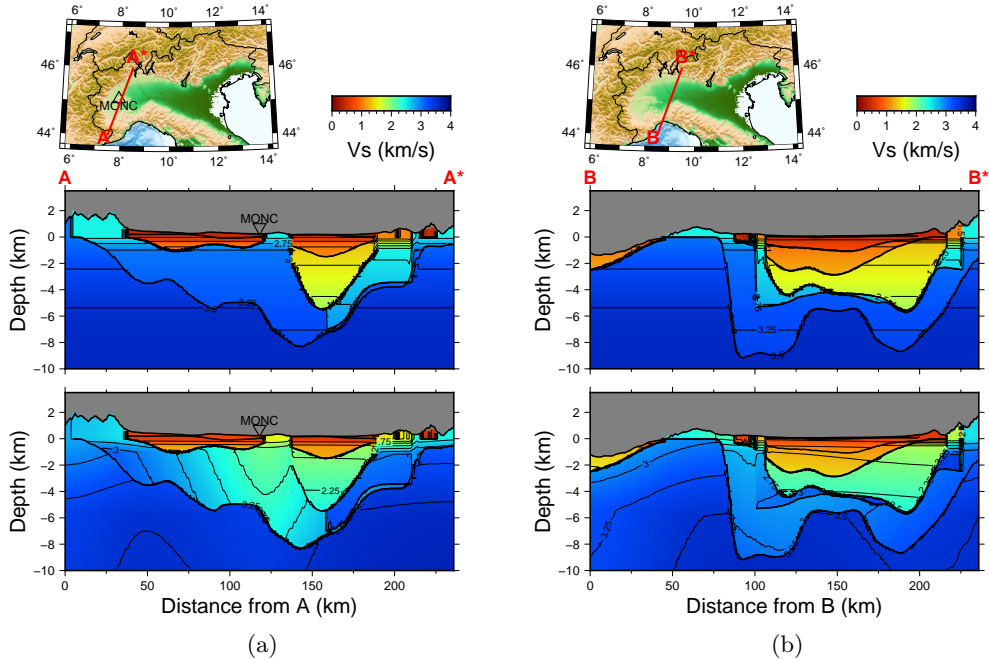


Figure 5.5: *Section of model MAMBo (top) and MAMBo-E (bottom)*

We show a few vertical cross-sections, cut through both the original MAMBo (top panels), and the calibrated MAMBo-E models (bottom panels). A detailed discussion of the geological implications of the variations mapped here is beyond the scope of the present study. We may however briefly point out some of the most relevant features. We focused on the shallowest crust down to 10 km where the most relevant differences are.

MAMBo-E shows a general higher shear-wave velocity compared to MAMBo, especially in the plain. Differences with MAMBo are more evident in the eastern part of the plain (sections C, D, E and F) at shallow depth.

At section A (figure 2.4) a high-velocity zone is evident beneath station MONC, at ≈ 125 km from A point. This area corresponds roughly with the Monferrato Arc, an outer arc of northern Apennines (see section 1.1).

Another high-velocity zone is visible in the eastern part of the plain at around 375 km from G and H points (figure 5.8 and 5.9). This area corresponds to the Eastern extremity of the Ferrara-Romagna Arc, the fold system that caused the 2012 Emilia seismic sequence (see chapter 1).

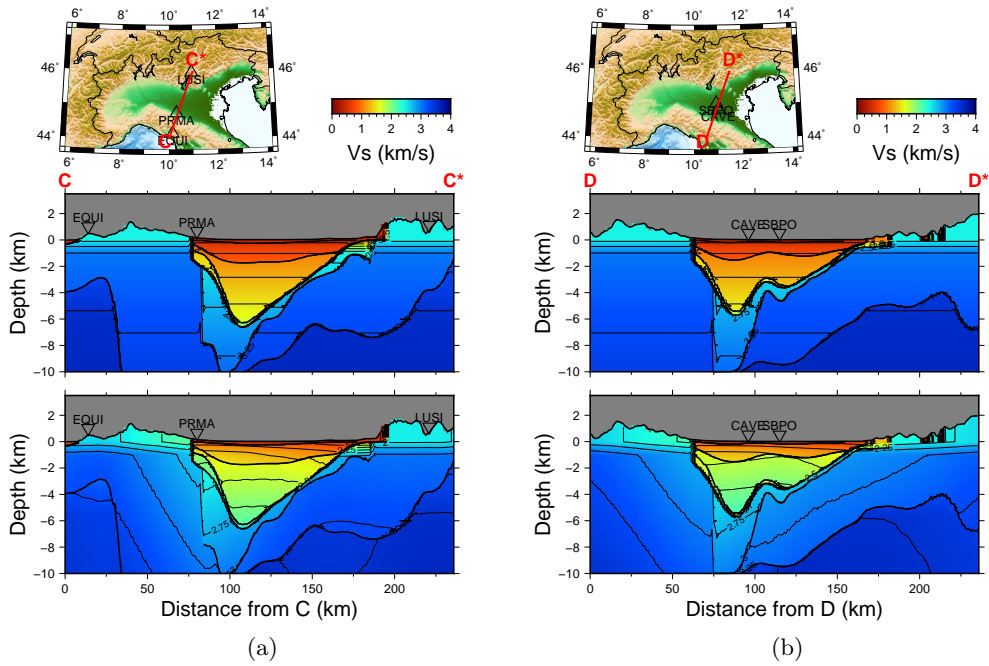


Figure 5.6: Section of model MAMBo (top) and MAMBo-E (bottom)

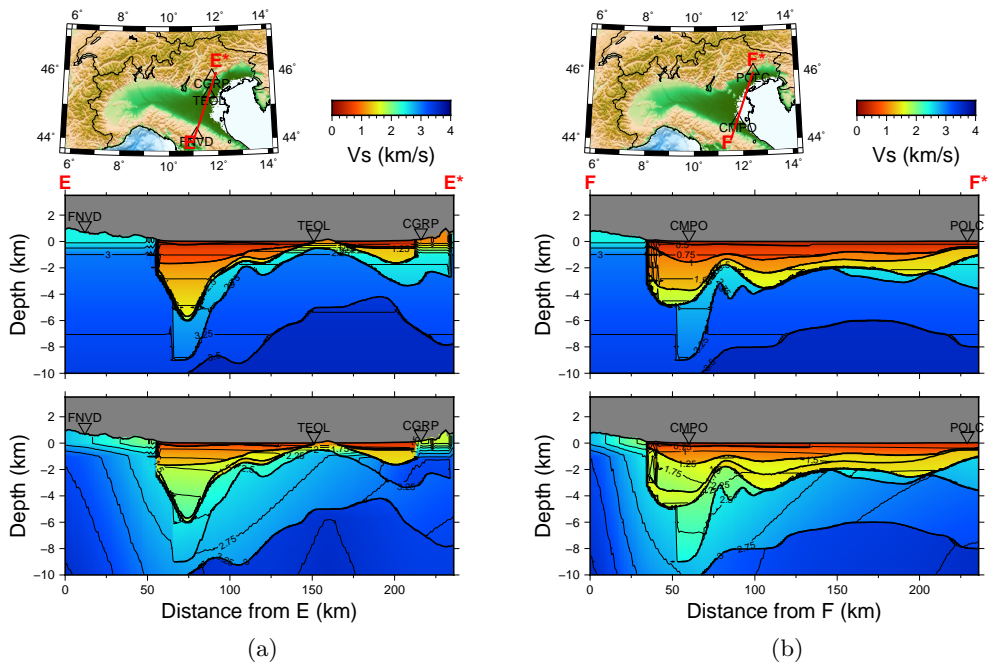


Figure 5.7: Section of model MAMBo (top) and MAMBo-E (bottom)

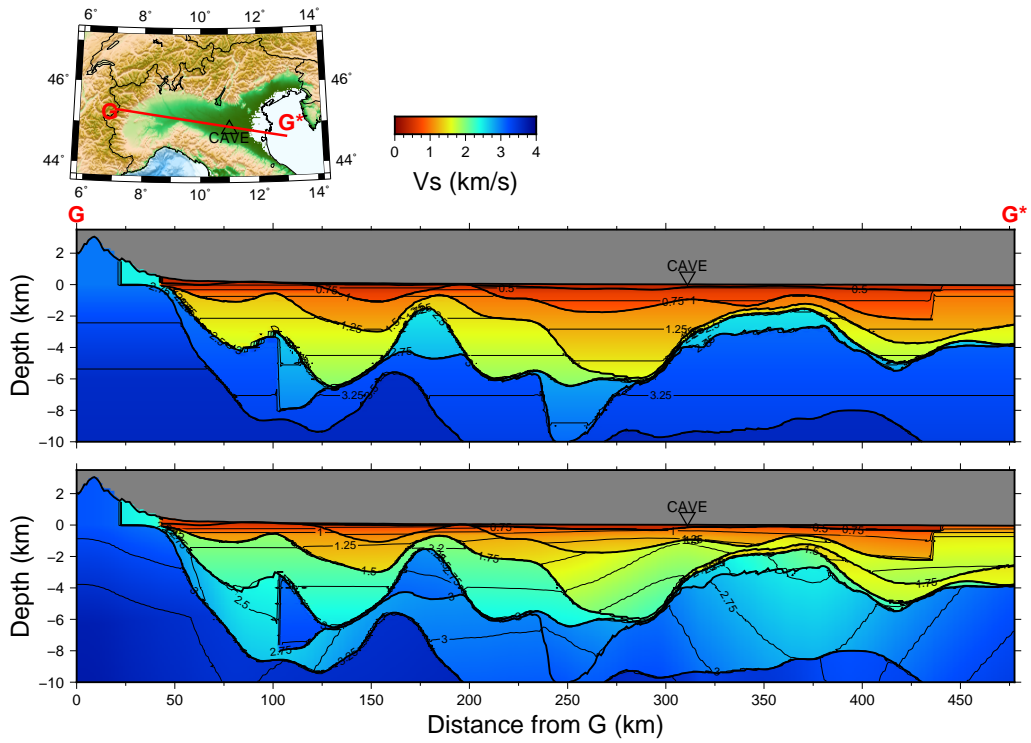


Figure 5.8: Section of model MAMBo (top) and MAMBo-E (bottom)

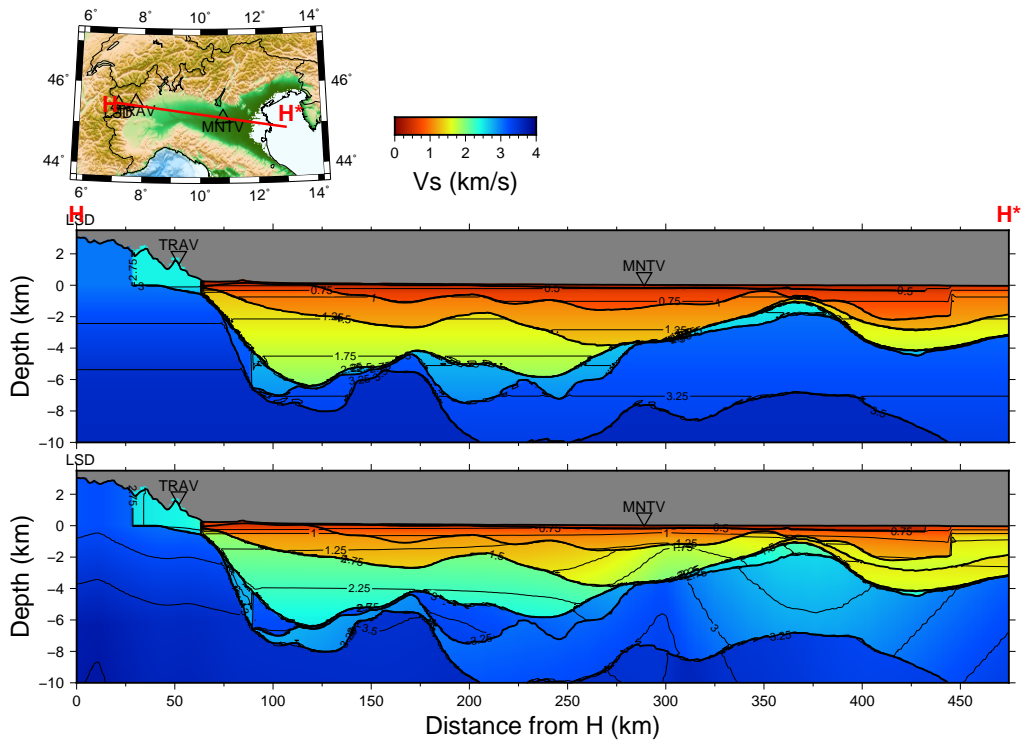


Figure 5.9: Section of model MAMBo (top) and MAMBo-E (bottom)

5.5.2 Depth sections

We show here a few sections, cut at constant depth, of v_S of both MAMBo and calibrated MAMBo-E. The same main features observed in the cross-sections are visible here. v_S is in general higher for model MAMBo-E than MAMBo and differences are much more evident for shallow depth in the plain. In all the depth sections we can notice the high-velocity zone in the western part of the Po Plain, around the point with coordinates $8.4^\circ\text{E} - 45^\circ\text{N}$. This corresponds to the Monferrato Arc. The other high-velocity zone is located in the south-eastern part of the plain, around the point with coordinates $11.5^\circ\text{E} - 44.5^\circ\text{N}$. This feature is visible at 4 km, 6 km and 8 km (figure 5.11, 5.12 and 5.13) and corresponds to the Eastern Ferrara-Romagna Arc. There are no reliable differences between MAMBo and MAMBo-E beneath the Alps at larger depth (e.g. 6 - 8 km).

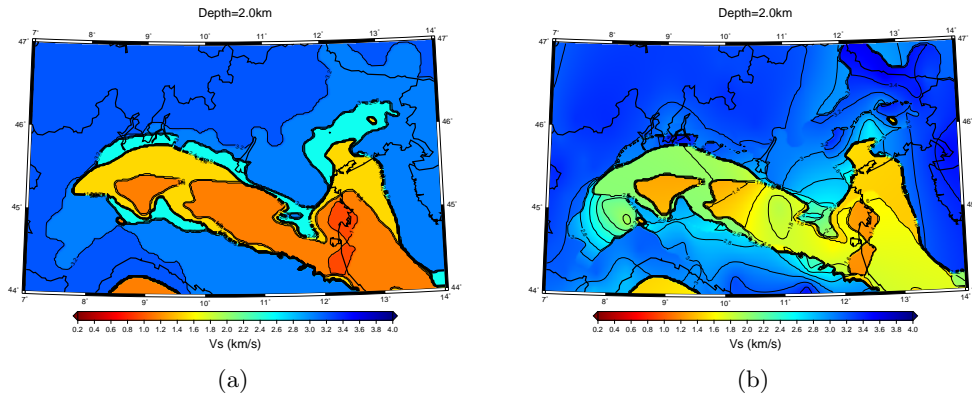


Figure 5.10: *Shear-velocity at 2 km of depth for MAMBo (a) and MAMBo-E (b)*

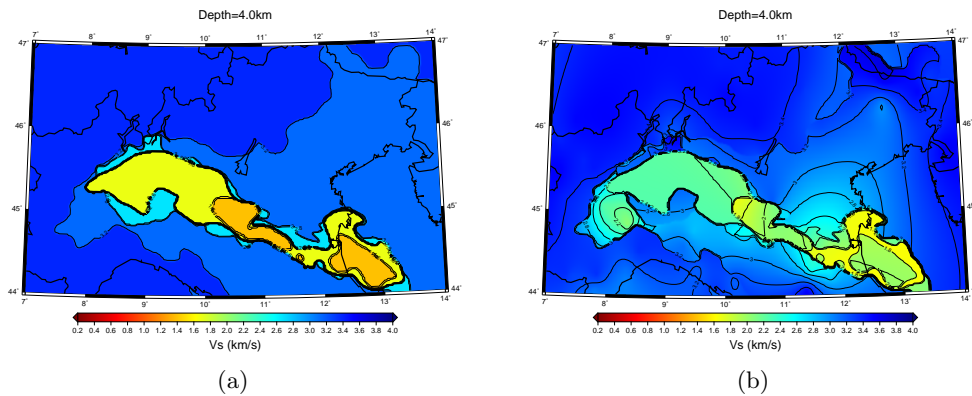


Figure 5.11: *Shear-velocity at 4 km of depth for MAMBo (a) and MAMBo-E (b)*

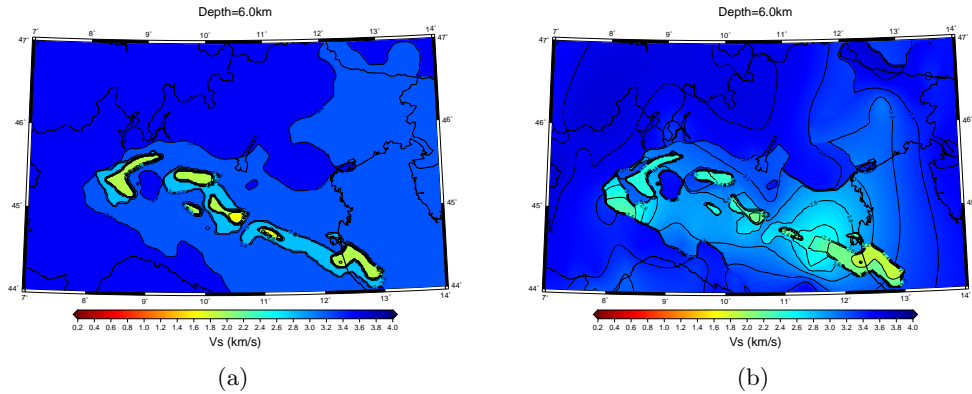


Figure 5.12: *Shear-velocity at 6 km of depth for MAMBo (a) and MAMBo-E (b)*

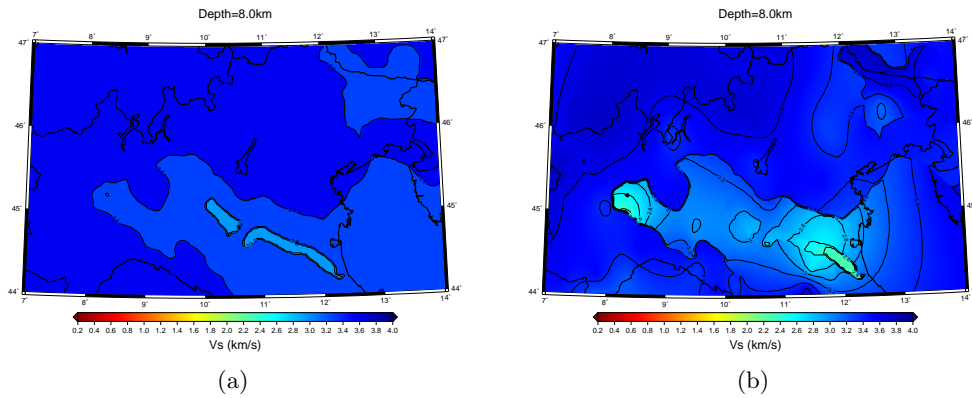


Figure 5.13: *Shear-velocity at 8 km of depth for MAMBo (a) and MAMBo-E (b)*

5.5.3 Ellipticity maps

We calculate by modal summation (Herrmann, 2013) the theoretical ellipticity from both MAMBo and calibrated MAMBo-E for four periods: 11 s, 16 s, 25 s and 38 s (figures 5.14, 5.15, 5.16 and 5.17) compared to real measurements of ellipticity.

Obviously MAMBo-E theoretical values show a good agreement with real data, since measurements have been used for retrieve the calibration of the model. Small discrepancies are still visible between observations and predictions, especially at shortest periods (e.g. stations CMPO and FAEN). This is possibly due to the Ordinary Kriging interpolation that smooths the model between the stations to obtain a realistic model.

For shortest periods (e.g. 11 s and 16 s) MAMBo produces very high and unrealistic H/V values that are not present any more in calibrated model MAMBo-E.

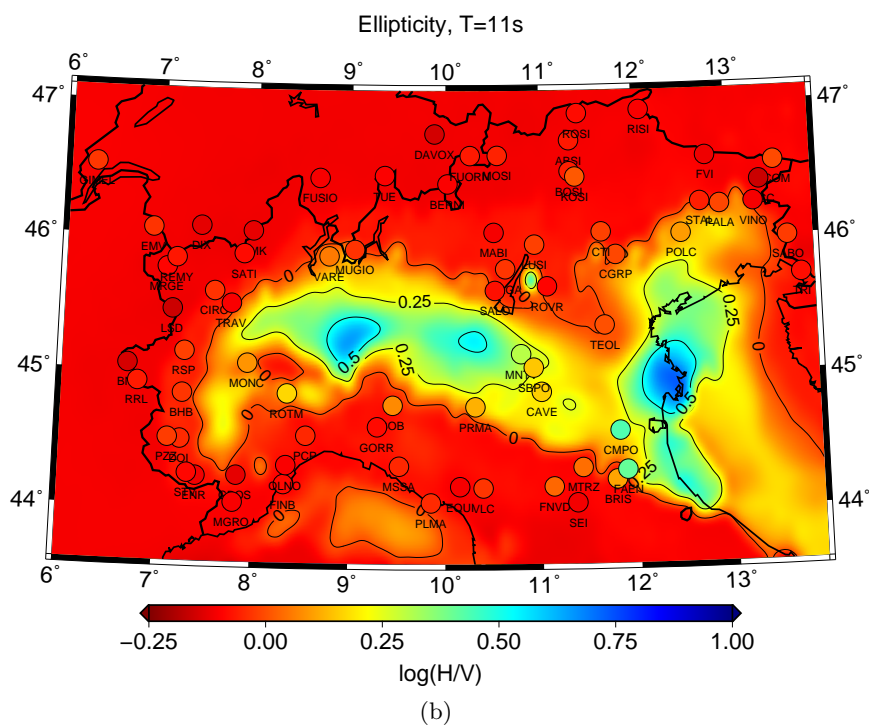
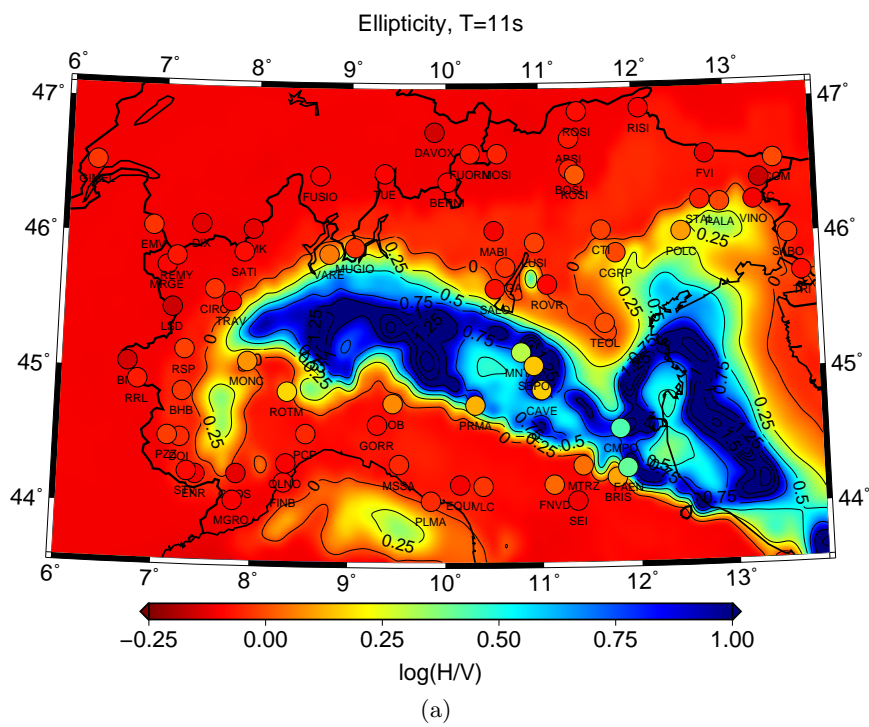
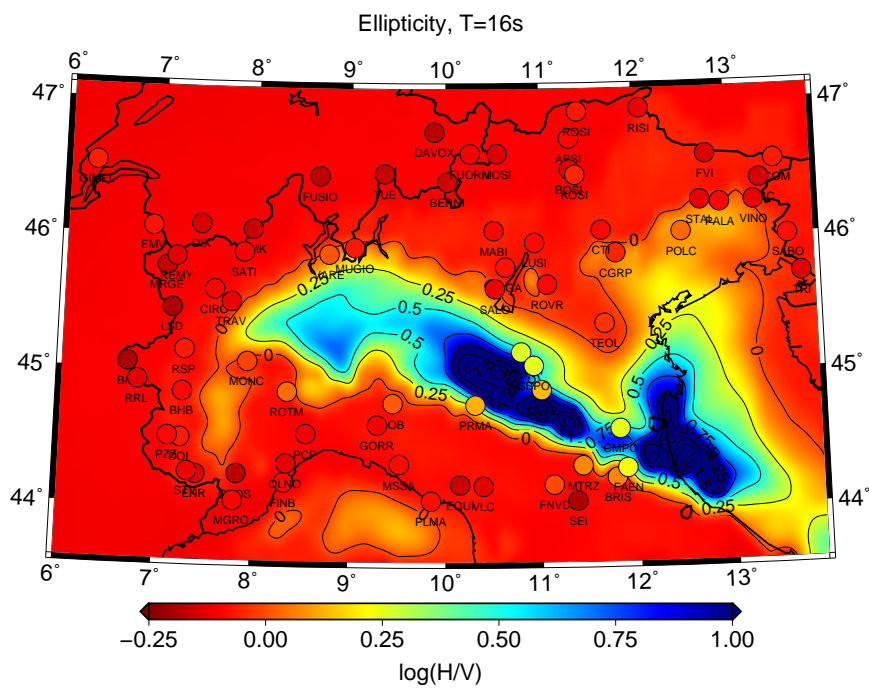
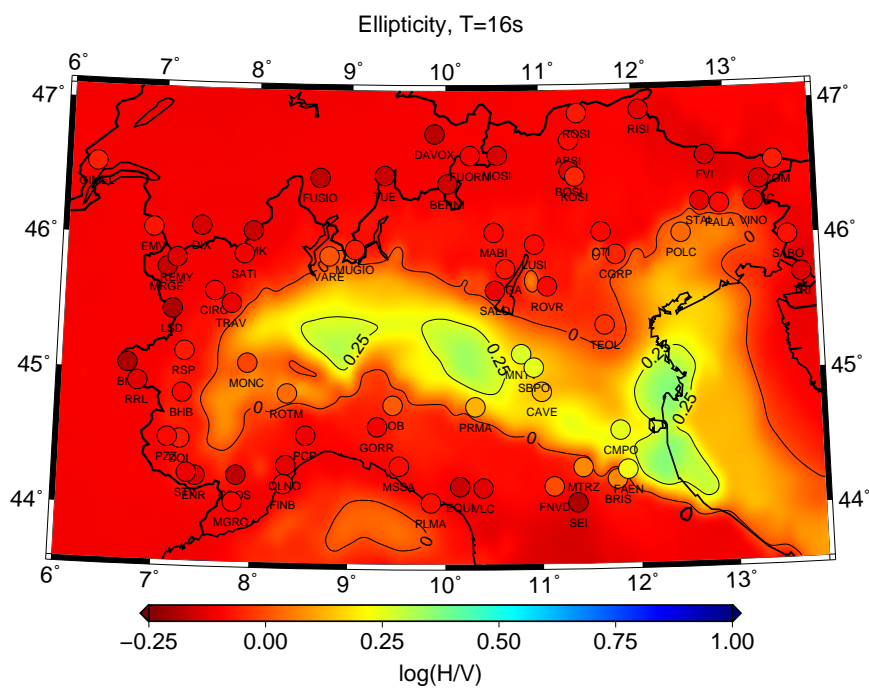


Figure 5.14: Ellipticity observed (circles) compared to expected values for MAMBo (a) and MAMBo-E (b) at 11s period.



(a)



(b)

Figure 5.15: Ellipticity observed (circles) compared to expected values for MAMBo (a) and MAMBo-E (b) at 16s period.

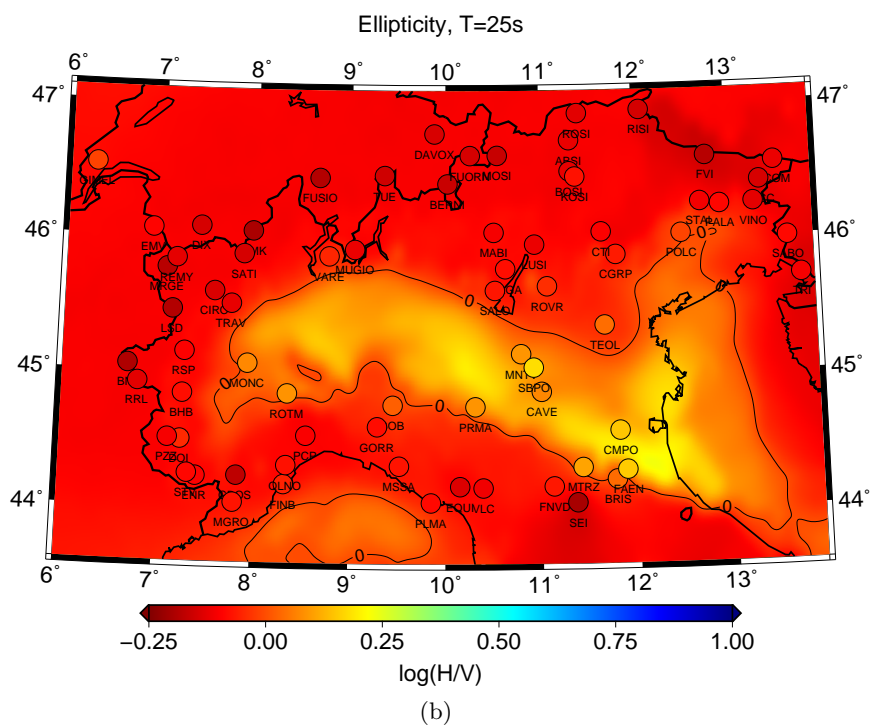
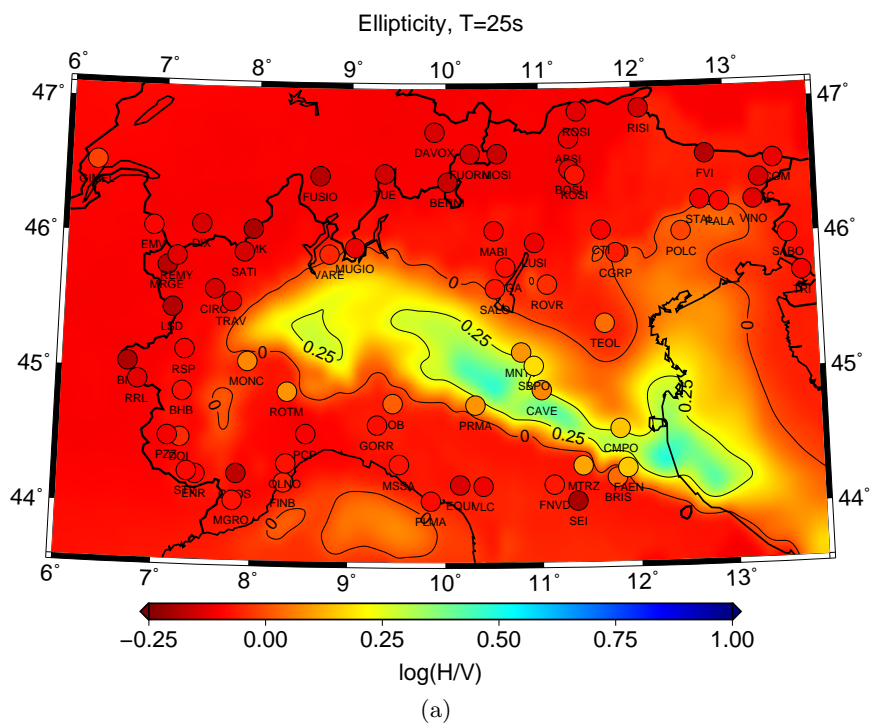


Figure 5.16: *Ellipticity observed (circles) compared to expected values for MAMBo (a) and MAMBo-E (b) at 25s period.*

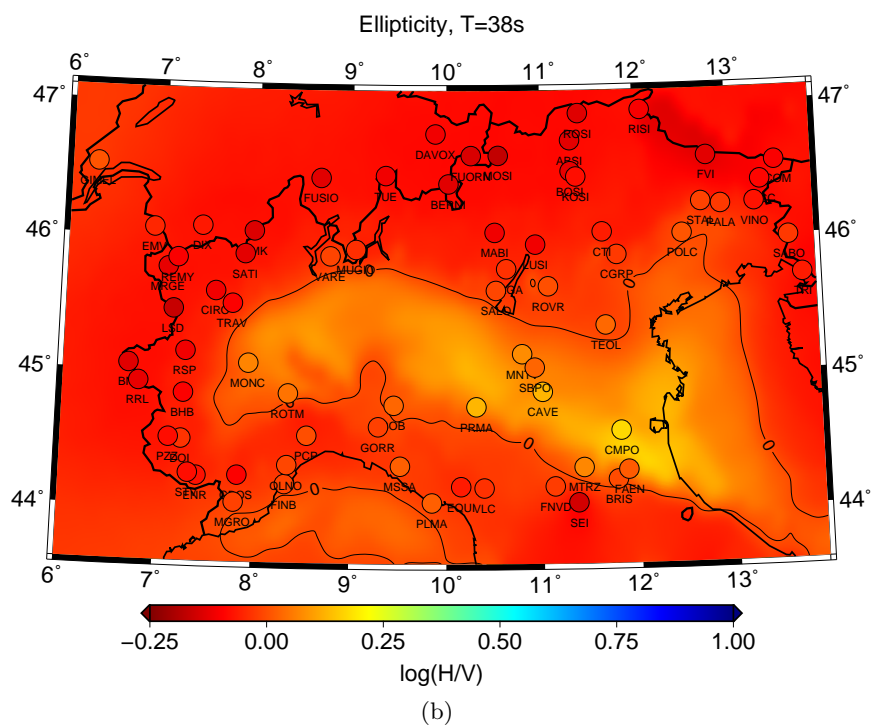
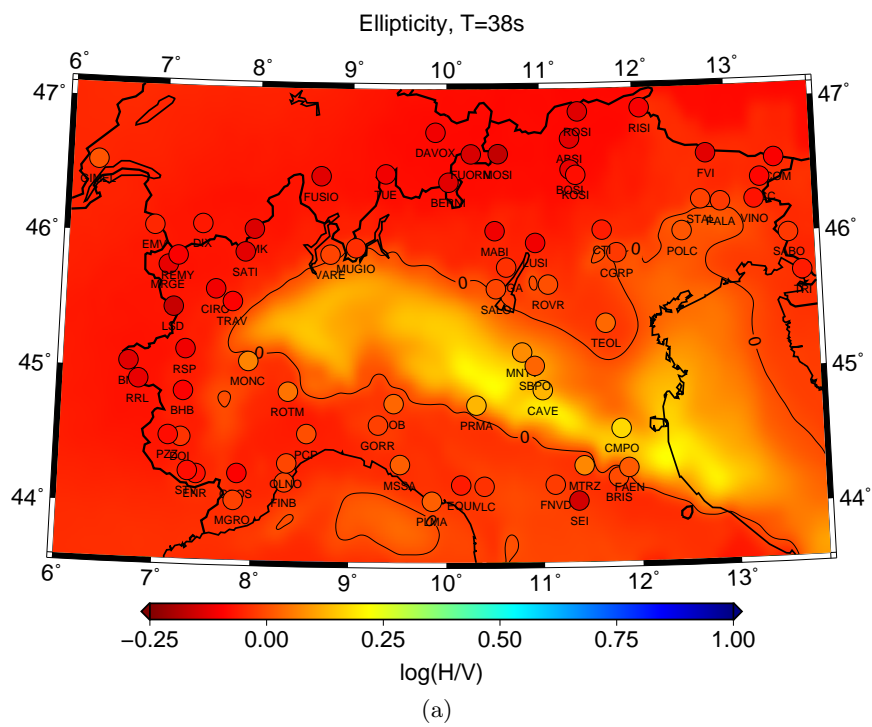


Figure 5.17: Ellipticity observed (circles) compared to expected values for MAMBo (a) and MAMBo-E (b) at 38s period.

5.5.4 Cross correlation

We compare here observed H/V ratios with theoretical values calculated by modal summation (Herrmann, 2013) from MAMBo (left panel) and MAMBo-E (right panel) at four periods: 11 s, 16 s, 25 s and 38 s (figures 5.18a,b,c and d). On the top of each panel there is the Pearson correlation coefficient between predictions and observations. As expected stations in the plain (blue dots) show the largest differences between MAMBo and MAMBo-E predictions. For all the periods the correlation for MAMBo-E is bigger than for MAMBo.

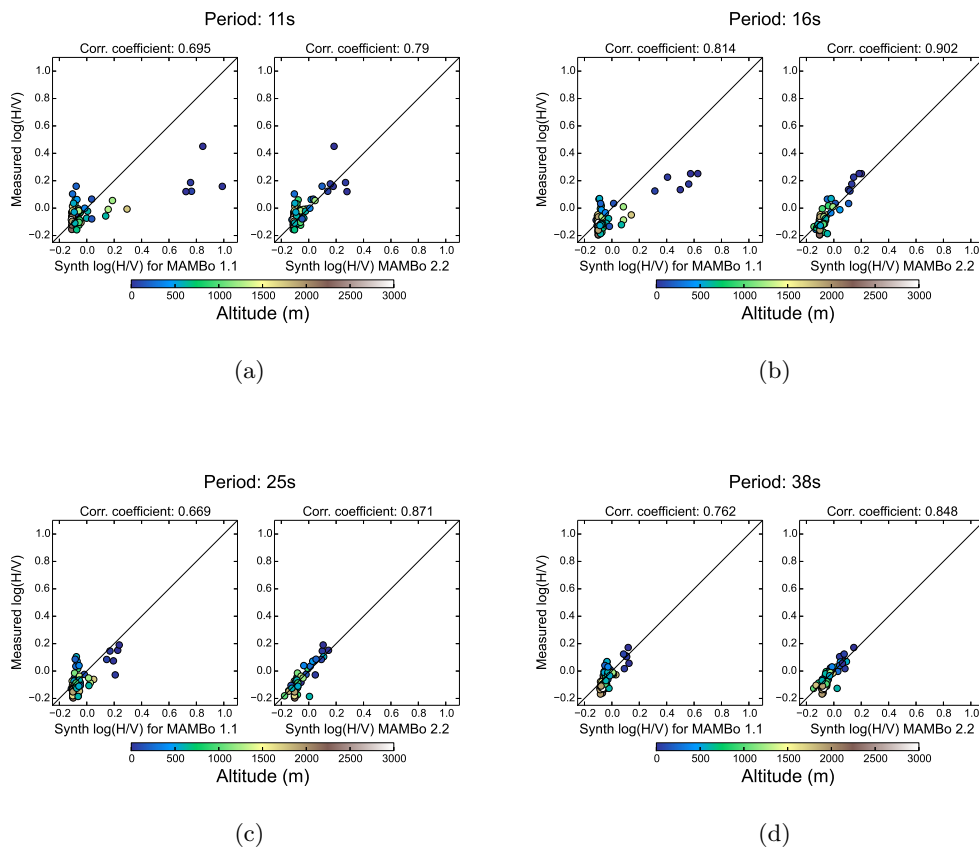


Figure 5.18: Comparison between observed ellipticity (y axes) and synthetic ellipticity calculated on MAMBo (on the left, x axis) and MAMBo-E (on the right, x axis) for 11 s (a), 16 s (b), 25 s (c), 38 s (d).

5.5.5 Phase and group velocities

Finally we plot the phase and group velocities computed by modal summation for model MAMBo and MAMBo-E for four periods: 6 s, 10 s, 16 s and 24 s. Seismic stations used in this study are plotted with black dots.

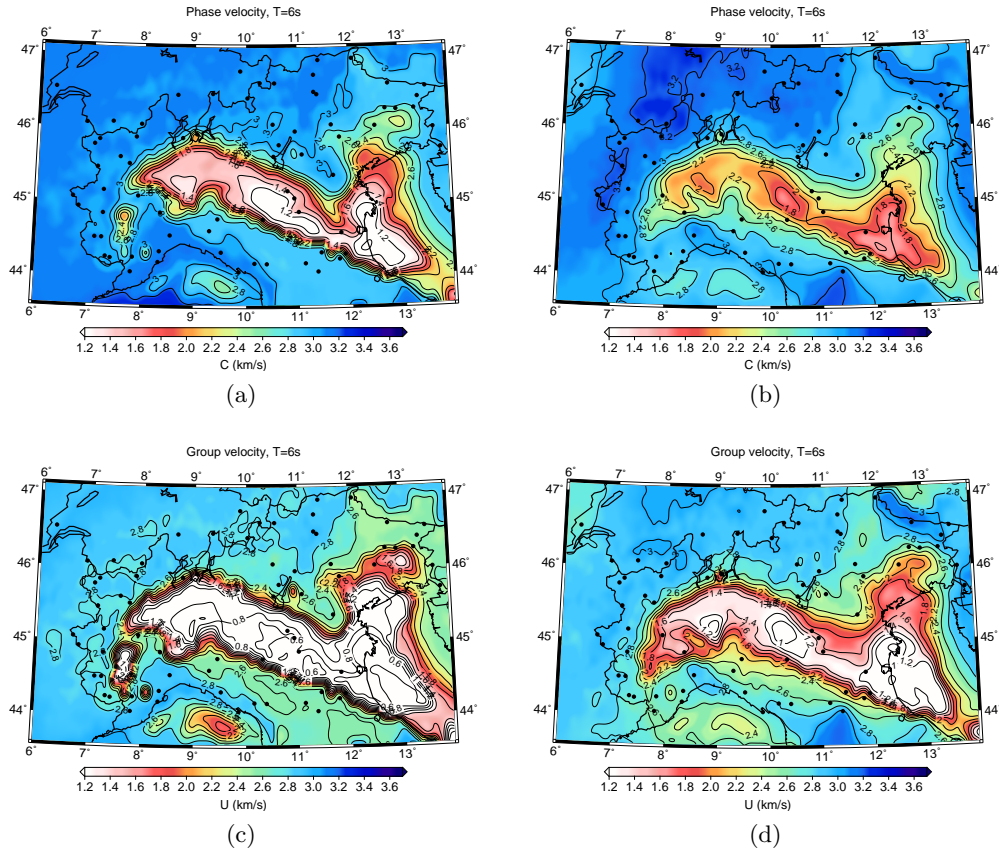


Figure 5.19: Phase velocity at period $T = 6$ s for model MAMBo (a) and MAMBo-E (b), group velocity for model MAMBo (c) and MAMBo-E (d). Black dots indicate the seismic stations used in this work.

We see that the features observed in the depth and cross sections are still visible, both in group and phase velocities maps. MAMBo-E has in general faster velocities. The same high-velocities zones seen in the section are visible here, especially at a period of 10 s. One is located in the south-eastern part of the plain, close to the Adriatic Sea and it is visible also at longer periods (16 and 24 s). The other is located in the western part of the plain, in the Monferrato Area, around the point with coordinates $8.4^\circ\text{E} - 45^\circ\text{N}$. Smaller discrepancies between MAMBo and MAMBo-E are visible on the Alps.

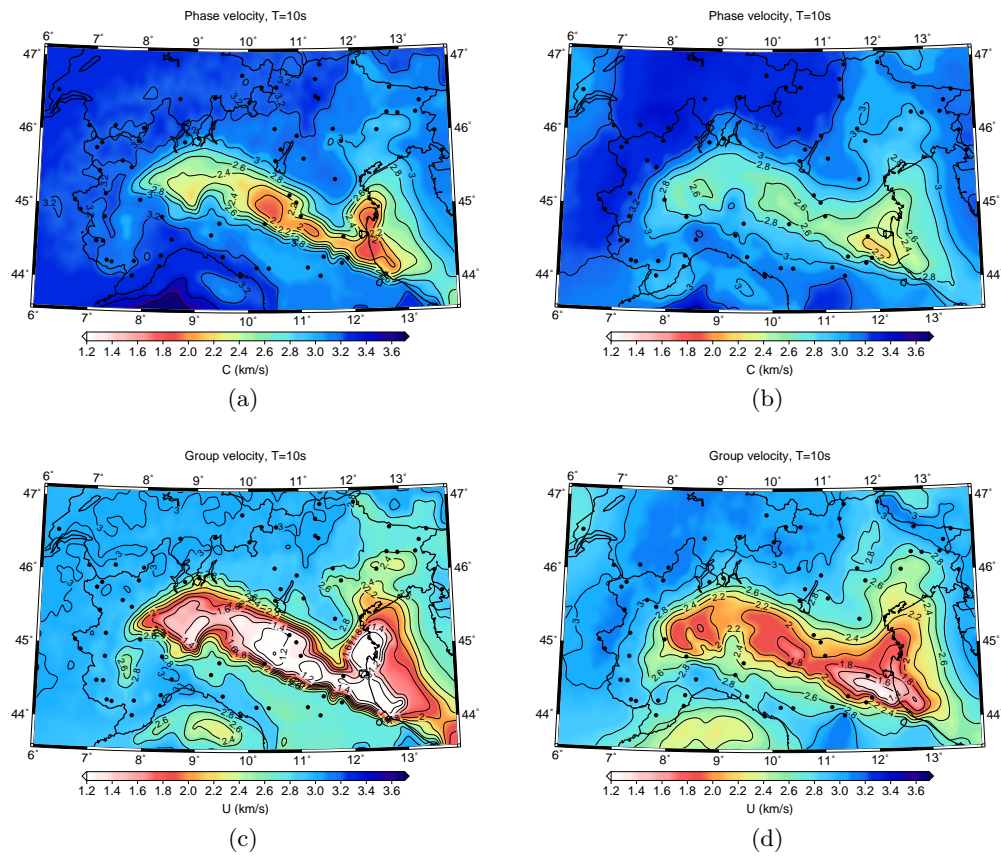


Figure 5.20: Phase velocity at period $T = 10$ s for model MAMBo (a) and MAMBo-E (b), group velocity for model MAMBo (c) and MAMBo-E (d). Black dots indicate the seismic stations used in this work.

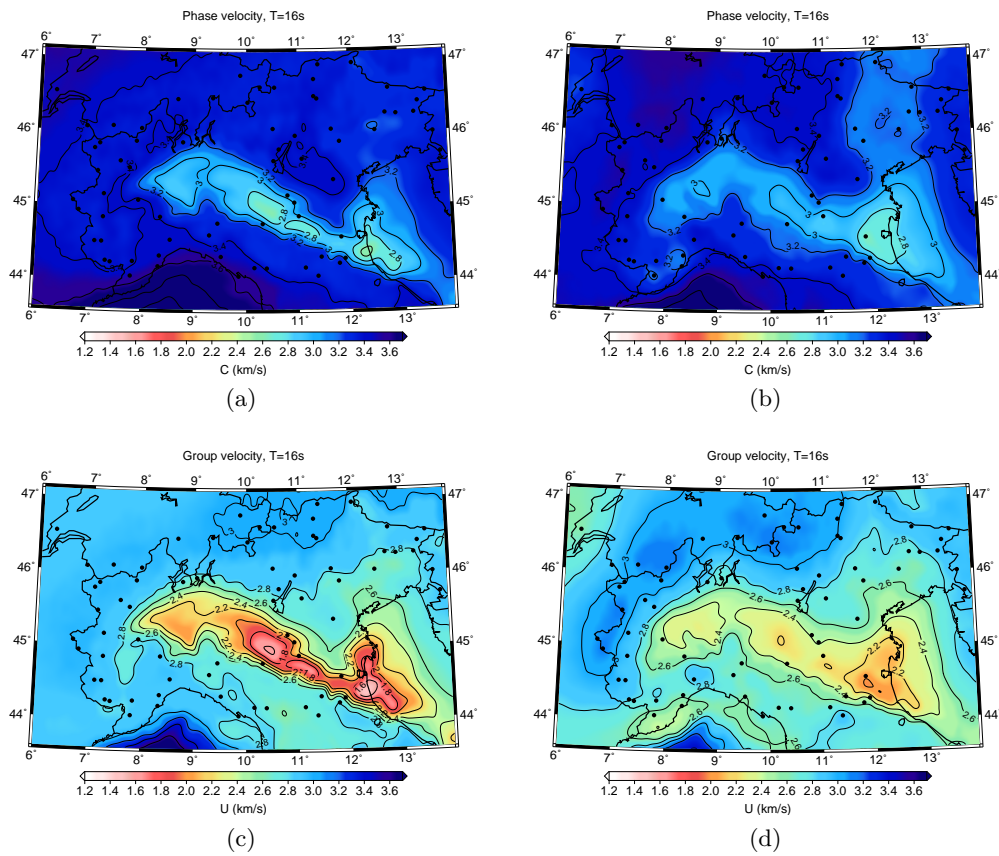


Figure 5.21: Phase velocity at period $T = 16$ s for model MAMBo (a) and MAMBo-E (b), group velocity for model MAMBo (c) and MAMBo-E (d). Black dots indicate the seismic stations used in this work.

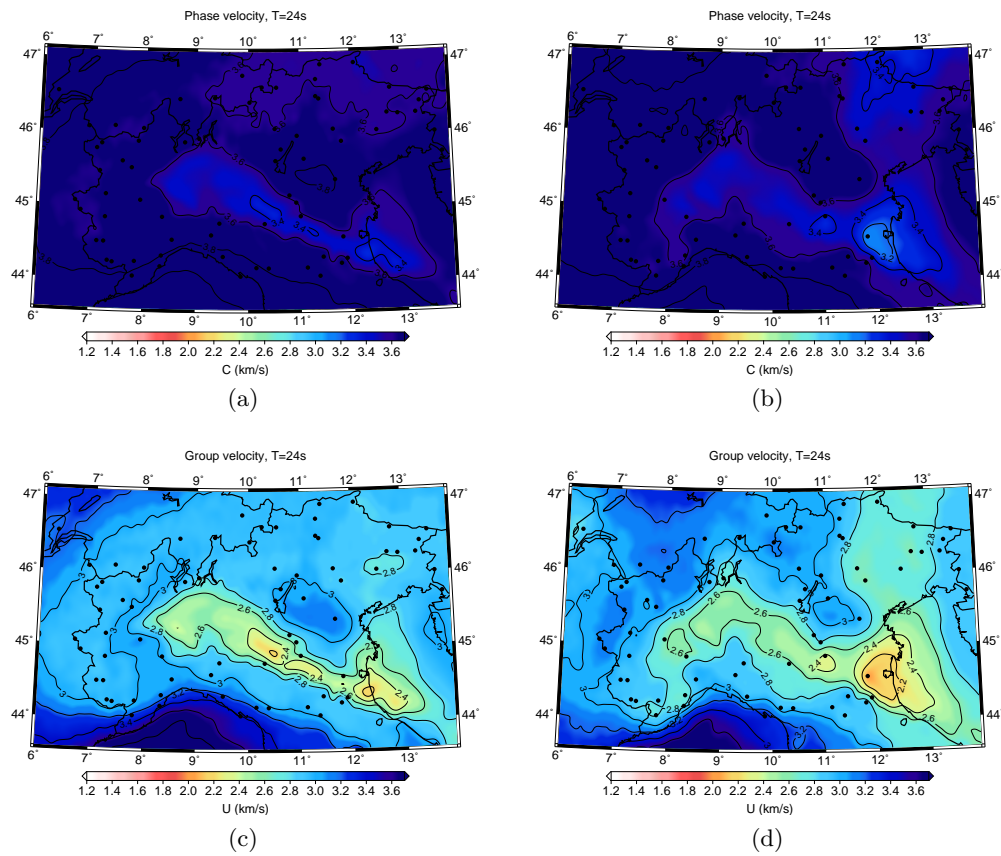


Figure 5.22: Phase velocity at period $T = 24$ s for model MAMBo (a) and MAMBo-E (b), group velocity for model MAMBo (c) and MAMBo-E (d). Black dots indicate the seismic stations used in this work.

5.6 Discussion

The inversion method proposed here showed a good ability of retrieve shear-wave profiles under the plain. We have obtained an updated version of MAMBo, MAMBo-E, that shows quite large discrepancies from the starting model especially in deep-sedimentary areas and small depth. This was expected since the depth sensitivity of ellipticity is concentrated in the first few kilometres. Because of this, this method was particularly reliable in this geological setting. Moreover the reliability of the updated model is not uniform: the distribution of the station network is not even so in some areas, like in the western Po Plain, the new model is not totally reliable. Ellipticity only gives information on the structure beneath the station, so no information is given in areas between to far stations. A joint inversion with phase and group velocity measurements from ambient noise can compensate the uneven station coverage and give a better illumination of the study area, both laterally and vertically, because of deeper sensitivity. The model MAMBo-E has to be validated by comparison with an independent dataset, like dispersion curves, to evaluate its resolution and ability of reproducing real data.

Conclusions

This study was aimed to set up a reliable system to use ellipticity of Rayleigh waves, a relatively little-known parameter of seismic surface waves, to improve the knowledge of the shallow crustal structure of northern Italy. A detailed knowledge of the shallowest part of the crust is indeed crucial for seismic hazard and ground-shaking prediction in sedimentary settings like Po Plain, the largest sedimentary basin in Italy. This became particularly clear after the 2012 Emilia sequence, that showed that even intermediate-magnitude events can impact seriously on the anthropic and economic infrastructure.

To achieve our purpose we firstly implemented a method for measuring ellipticity on teleseismic records based on a scheme originally proposed by Tanimoto & Rivera (2008). One of the main difficulties to overcome consists on how to separate the fundamental mode of Rayleigh waves from overtones and other arrivals in the wave train. We validated the method comparing the values measured on synthetics with theoretical expected values. The comparison showed a good capability of the method to separate and measure the ellipticity of Rayleigh waves for crustal earthquakes. Some discrepancy has been found for deeper earthquakes. The method is very selective so a large dataset is needed for coherent statistical analysis of the results. Noisy stations need at least 100-150 large events to yield a stable and reliable average of measurements.

We widely applied the measurement scheme to a total of 95 seismic stations in northern Italy located both on the valley and on the mountains. For each station we selected earthquakes with magnitude $M_W \geq 5.0$ and epicentral distance between 10 and 140 degrees that occurred from January 2008 to December 2014. We measured ellipticity on all available data in the period range between 10 s and 110 s. We found a clear correlation between higher values of ellipticity and shallow sedimentary structures, particularly evident at shorter periods. This confirms the hypothesis that H/V ratio is mostly sensitive to the shallowest part of the crust, as shown from the sensitivity kernels (figure 2.1).

We verify that ellipticity does not depend on the wave path or on the seismic source, as expected from ray-theory. We compared ellipticity values measured on

synthetics computed by numerical simulations done with a spectral-element code (SpecFem3D Globe, Komatitsch & Tromp, 2002; Peter et al. 2011) using the 3D global model SGLOBE-rani (Chang et al., 2015) with ellipticity measured on synthetics calculated by modal summation from 1D models computed at the receiver. We found no discrepancies between ellipticity from 3D and 1D models, showing that indeed only the structure at the receiver affects ellipticity measurements.

We then studied the phenomenon of the inversion of particle motion polarization of Rayleigh waves from retrograde (normal) motion to prograde motion. We calculated the transition period in the study area and we found values in the range 2 s – 16 s, compatible with the values found by Tanimoto & Rivera (2005) for the Los Angeles basin. We found a clear correlation between longer transition periods and thicker sedimentary layers. Direct observation of the polarity inversion on real data was difficult due to the low signal amplitude in earthquake recordings in this period range, together with higher level of ambient noise for stations located on the plane, where the inversion is expected.

We then inverted the ellipticity curves as a function of period to obtain a v_S profile for the crust beneath each station. We used a completely non-linear inversion technique (the Neighbourhood Algorithm by Sambridge 1999) because of the high non-linearity of the problem, shown by the sensitivity kernels (figure 2.1). Parametrization of the crust has been a particularly critical issue because of the non-linearity of ellipticity. We followed two approaches.

First, we used a simple 4-layers parametrization, the same for all the stations, with Moho depth fixed to values from previous studies (EPCrust by Molinari & Morelli 2011). The profiles obtained show a general good agreement with previous results like MAMBo and phase and group velocity tomography from ambient noise measurements. However, these results cannot be directly and optimally used for constructing a new 3D model of the whole area, as such an endeavour would involve wide interpolation between stations. We recall here that the information we have derived, are to be referred as profiles beneath stations, geographically point-like in their nature (or relative to, say, areas one wavelength wide). To fill an entire 3D volume thus entails interpolation in regions with no stations – of which unfortunately there are wide expanses in the inner plain.

We then followed a different approach: we kept the same layer structure of MAMBo (Molinari et al., 2015) and we inverted for v_S inside each geological layer. The parameterisation was then different for each station, both for layer thickness and the number of layers. We used the results to update the MAMBo model and obtain a new model that better reproduces ellipticity measurements.

The results obtained demonstrated that ellipticity of Rayleigh waves is an important tool for the study of the shallowest part of the crust, particularly useful in

sedimentary terrains.

The inversion of ellipticity alone showed a good capability to yield a profile for v_S . A joint inversion of ellipticity with phase and group velocity could improve the sensitivity in depth, illuminating the whole crust down to the Moho. Such a joint inversion on the other hand will lose the advantage of using a totally single-station technique.

There are still some open issues: The new model obtained, MAMBo-E, is indeed successful in better reproducing ellipticity. However, it still awaits a wider validation using propagating surface waves, i.e. group and/or phase velocity measurements, to investigate its ability to fit other independent data. This may efficiently be done using ambient noise correlation, but such an analysis is beyond the scope of the present study.

The lateral resolution of ellipticity is still an open issue: we point out that H/V depends only on the structure beneath each receiver station. This is shown by ray theory. However, once we look at finite-frequency effects we expect that a lateral area of sensitivity – in fact, a Fresnel zone – should be involved. These details need further significant efforts to be clarified. In preliminary numerical simulations, we found that a region of influence indeed exists, where a sharp perturbation of structure shows its effects, but such exploratory results need extensive work to be put in a clear and consistent picture. Such an investigation, also, is well beyond the scope of the present study.

The elongation ratio of elliptically-polarised Rayleigh-wave particle motion is a little-known, and hence seldom used, observable sensitive to shallow earth structure. Its measurement can be done in a reliable and robust way, without large difficulties. Measured values can then be efficiently used to retrieve information, mainly about shear-wave velocity, beneath each station, with a depth that of course depends on the specific frequency band of each measurement. Sensitivity of ellipticity is shallower, and hence complementary, to that of phase or group velocity. We think therefore that ellipticity has excellent prospects for wider use for retrieval of crustal structure, especially in sedimentary basin environments.

Bibliography

Aagaard, B. T., T. M. Brocher, D. Dolenc, D. Dreger, R. W. Graves, S. Harmsen, S., Hartzell, S. Larsen, K. McCandless, S. Nilsson, N. A. Petersson, A. Rogers, B. Sjorreen and M. L. Zoback (2008). Ground-Motion Modeling of the 1906 San Francisco Earthquake, Part II: Ground-Motion Estimates for the 1906 Earthquake and Scenario Events, *Bull. Seism. Soc. Am.* 98 1012–1046.

Abraham, R. J., Lai, C.G., Papageorgiou, A., 2015. Basin-effects observed during the 2012 Emilia earthquake sequence in Northern Italy, *Soil Dynamics and Earthquake Engineering*, 78, 230-242, doi: <http://dx.doi.org/10.1016/j.soildyn.2015.08.007s>

Anderson, H., and Jackson, J., 1987. Active tectonics of the Adriatic region, *Geophys. J. R. Astron. Soc.* 91, 937–983.

Bard PY, Campillo M, Sánchez-Sesma F, Chávez Garcia FJ, 1998. The mexico earthquake of september 19, 1985-a theoretical investigation of large-and small scale amplification effects in the mexico city valley. *Earthq Spectra*;4 (6):609–33.

Bradley BA, 2012. Strong ground motion characteristics observed in the 4 September Darfield, New Zealand earthquake. *Soil Dyn Earthq Eng*;42:32–46.

Beyreuther, M., Barsch, R., Krischer, L., Megies, T., Behr, Y. and Wassermann, J., 2010, *ObsPy: A Python Toolbox for Seismology* SRL, **81(3)**, 530-533 DOI:10.1785/gssrl.81.3.530

Boccaletti , M., Coli , M., Eva , C., Ferrari , G., Giglia , G., Lazzarotto , A., Merlanti , F., Nicolich , R., Papani , G., and Postpischl, D. 1985. Considerations on the seismotectonics of the Northern Apennines, *Tectonophysics* 117, 7–38.

Bommer, J. J., & Martinez-Perreira , A. (1999). The effective duration of earthquake strong motion. *Journal of Earthquake Engineering*, 3(2), 127–172.

Bommer, J. J., Stafford, P. J., & Alarcon , J. E. (2009). Empirical equations for the prediction of the significant, bracketed, and uniform duration of earthquake ground motion. *Bulletin of the Seismological Society of America*, 99(6), 3217–3233.

- Boore D., Nafi Toksöz M., 1969. *Rayleigh wave particle motion and crustal structure*, *Bull. seism. Soc. Am.*, **59**, 331–346.
- Bragato, P., M. Sugan, P. Augliera, M. Massa and A. Vuan (2011). Moho reflection effects in the Po Plain (northern Italy) observed from instrumental and intensity data, *Bull. Seism. Soc. Am.* 101 20142–2152.
- Brocher, T. M., 2005. Empirical relations between elastic wavespeeds and density in the Earth’s crust, *Bull. Seism. Soc. Am.* 95 2081–2092.
- Carafa, M.M.C., and S. Barba, 2013. The stress field in Europe: optimal orientations with confidence limits, *Geophys. J. Int.*, 193, 531–548, doi:10.1093/gji/ggt024.
- Carminati, E., and Doglioni, C., 2012, Alps Vs. Apennines: the paradigm of a tectonically asymmetric Earth, *Earth-Sci. Rev.* 112, 67–96, doi:10.1016/j.earscirev.2012.02.004.
- Castellarin, A., and Cantelli, L., 2000. Neo-Alpine evolution of the Southern Eastern Alps, *J. Geodyn.* 30, 251–274.
- Chaljub, E., P. Moczo, S. Tsuno, P.-Y. Bard, J. Kristek, M. Káser, M. Stupazzini and M. Kristekova (2010). Quantitative comparison of four numerical predictions of 3D ground motion in the Grenoble valley, France, *Bull. Seism. Soc. Am.* 100 1427–1455.
- Chang, S.-J., Ferreira, A.M.G., Ritsema, J., van Heijst, H. J., & Woodhouse, J. H. 2015. Joint Inversion for Global Isotropic and Radially Anisotropic Mantle Structure Including Crustal Thickness Perturbations. *Journal of Geophysical Research*. Approved for publication.
- Constable, S. C., Parker, R. L. and Constable, C. G., 1987. Occam’s inversion: A practical algorithm for generating smooth models from electromagnetic sounding data, *Geophysics*, 52, 3, 289-300.
- Dhakal, Y. D. and H. Yamanaka (2013). An evaluation of 3D velocity models of the Kanto basin for long-period ground motion simulations, *J. Seismol.* 17 1073–1102.
- Diehl, T., S. Husen, E. Kissling, and N. Deichmann, 2009, High-resolution 3-D P-wave model of the alpine crust, *Geophys. J. Int.*, 179(2), 1133–1147.
- Dolce, M., & Di Bucci, D., 2014. National Civil Protection Organization and technical activities in the 2012 Emilia earthquakes (Italy). *Bulletin of Earthquake Engineering*, 1–23.

- Dujardin, A., Causse, M., Courboux, F. and Traversa, P., 2016. Simulation of the basin effects in the Po Plain during the Emilia-Romagna seismic sequence (2012) using empirical Green's functions, *Pure and applied geophysics*, doi: 10.1007/s00024-015-1233-4
- Dziewonski, A.M., Anderson, D.L., 1981. Preliminary reference Earth model, *Physics of the Earth and Planetary Interiors*, **25**, 4, 297-356.
- Dziewonski, A.M., Chou, T.A. & Woodhouse, J.H., 1981. Determination of earthquake source parameters from waveform data for studies of global and regional seismicity, *J. Geophys. Res.*, **86** (B4), 2825–2852.
- Di Giulio, G., C. Cornou, M. Ohrnberger, M. Wathelet, and A. Rovelli, 2006. Deriving Wavefield Characteristics and Shear-Velocity Profiles from Two-Dimensional Small-Aperture Arrays Analysis of Ambient Vibrations in a Small-Size Alluvial Basin, Colfiorito, Italy. *Bull. Seism. Soc. Am.*, **96**, 1915–1933.
- Ekström, G. & Busby, R.W., 2008. Measurements of seismic orientation at US-Array transportable array and backbone stations, *Seismological Research Letters*, Vol. 79 N. 4, 554-561.
- Ekström, G., Nettles, M. & Dziewonski, A.M., 2012. The global CMT Project 2004–2010: centroid-moment tensors for 13,017 earthquakes, *Phys. Earth planet. Int.*, 200–201, 1–9.
- Emergeo Working Group (2013). Coseismic geological effects associated with the Emilia earthquake sequence of May-June 2012 (Northern Italy), *Nat. Hazards Earth Syst. Sci.*, 13, 1–13, doi:10.5194/nhess-13-1-2013
- Faccioli, E., 2013. Recent evolution and challenges in the Seismic Hazard Analysis of the Po Plain region, *Northern Italy*, *Bull. Earthquake Eng.* 11, 5–33, doi:10.1007/s10518-012-9416-1.
- Ferreira, A.M.G. & Woodhouse, J.H. 2007. Source, path and receiver effects on seismic surface waves, *Geophys. J. Int.*, **168**, 109-132.
- Ferreira, A.M.G. & Woodhouse, J.H. 2007. Observations of long period Rayleigh wave ellipticity, *Geophys. J. Int.*, **169**, 161-169.
- Gilbert, F., 1970. Excitation of normal modes of the earth by earthquake sources, *Geophys. J. R. Astron. Soc.*, **22**, 223-226.
- Gualtieri L., P. Serretti, and A. Morelli, 2014. Finite-difference P-wave travel time seismic tomography of the crust and uppermost mantle in the Italian region, *Geochem. Geophys. Geosyst.*, **15**, 69-88, DOI: 10.1002/2013GC004988.

- Heidbach, O., Tingay, M., Barth, A., Reineker, J., Kurfeß, D. and Müller, B., 2008. The World Stress Map database release 2008, doi:10.1594/GFZ.WSM.Rel2008.
- Herrmann, R.B., 2013. Computer programs in seismology: An evolving tool for instruction and research, *Seismological Research Letters*, **84** (6), 1081-1088.
- ISIDE Working Group, 2010. Italian seismological instrumental and parametric database: <http://iside.rm.ingv.it>.
- Kagawa, T., B. Zhao, K. Miyakoshi and K. Irikura (2004), Modeling of 3D basin structures for seismic wave simulations based on available information on the target area: Case study of the Osaka basin, Japan, *Bull. Seism. Soc. Am.* 94, 1353–1368.
- Koketsu, K. and M. Kikuchi (2000). Propagation of seismic ground motion in the Kanto basin, *Science* 228 1237–1239.
- Komatitsch, D. and Tromp, J., 2002. Spectral-element simulations of global seismic wave propagation: I. validation, *Geophys. J. Int.*, **149** 390-412
- Krischer, L., Megies, T., Barsch, R., Beyreuther, M., Lecocq, T., Caudron, C., Wassermann, J., 2015 *ObsPy: a bridge for seismology into the scientific Python ecosystem*, *Computational Science & Discovery*, **8**(1), 014003 DOI: 10.1088/1749-4699/8/1/014003
- Lai, C. G., Bozzoni, F., Mangriotis, M. D., & Martinelli, M., 2015. Soil liquefaction during the May 20, 2012 M5. 9 Emilia earthquake, Northern Italy: field reconnaissance and post-event assessment. *Earthquake Spectra*, Vol. 31, No. 4, pp. 2351-2373. doi:<http://dx.doi.org/10.1193/011313EQS002M>
- Laske, G., Masters, G. and Reif, C., 2012. CRUST 2.0: A New Global Crustal Model at 2x2 Degrees. <http://igppweb.ucsd.edu/~gabi/crust2.html>.
- Lin, F-C., Schmandt, B., Tsai, V.C., 2012. Joint inversion of Rayleigh wave phase velocity and ellipticity using USArray: Constraining velocity and density structure in the upper crust, *Geophys. Res. Letters*, **39**, L12303, doi:10.1029/2012GL052196.
- Lin, F-C., Tsai, V.C., Schmandt, B., 2014. 3-D crustal structure of the western United States: application of Rayleigh-wave ellipticity extracted from noise cross-correlations *Geophys. J. Int.*, doi: 10.1093/gji/ggu160.
- Luzi, L., Pacor, F., Ameri, G., Puglia, R., Burrato, P., Massa, M. and Castro, R., 2013. Overview on the Strong-Motion Data Recorded during the May–June 2012 Emilia Seismic Sequence. *Seismological Research Letters*, 84(4), 629–644.

- Malagnini, L., Herrmann, R.B., Munafò, I., Buttinelli, M., Anselmi, M., Akinci, A., and Boschi, E. , 2012. The 2012 Ferrara seismic sequence: Regional crustal structure, earthquake sources, and seismic hazard, *Geophys. Res. Lett.* 39, L19302, doi:10.1029/2012GL053214.
- Massa, M., P. Augliera, G. Franceschina, S. Lovati, and M. Zupo (2012). The July 17, 2011, ML 4.7 Po Plain (northern Italy) earthquake: strong-motion observations from the RAIS network. *Ann. Geophys.* 55 309–321.
- Massironi, M., Zampieri, D., and Caporali, A., 2006. Miocene to present major fault linkages through the Adriatic indenter and the Austroalpine-Penninic collisional wedge (Alps of NE Italy). In: Moratti, G., and Chalouan, A. (Eds.), *Active Tectonics of the Western Mediterranean Region and North Africa*, Special Publications, 262, Geological Society, London, 245–258.
- Megies, T., Beyreuther, M., Barsch, R., Krischer, L., Wassermann, J., 2011, *ObsPy - What can it do for data centers and observatories?*, *Annals Of Geophysics*, **54(1)**, 47-58 DOI: 10.4401/ag-4838
- Molinari, I. and A. Morelli, 2011. EPcrust: A reference crustal model for the european plate, *Geophys. J. Int.* 185 352–364.
- Molinari, I. Argnani A., Morelli A., Basini, P., 2015. Development and testing of a 3D seismic 2 velocity model of the Po Plain sedimentary basin, Italy., *Bulletin of the Seismological Society of America*, **105**, No.2a, doi: 10.1785/0120140204
- Molinari, I., J. Verbeke, L. Boschi, E. Kissling, and A. Morelli, 2015. Italian and Alpine three-dimensional crustal structure imaged by ambient-noise surface-wave dispersion, *Geochem. Geophys. Geosyst.*, **16**, doi:10.1002/ 2015GC006176.
- Montone, P., Mariucci, M.T., and Pierdomenici, S., 2012. The Italian present-day stress map, *Geophys. J. Int.* 189, 705–716, doi:10.1111/j.1365-246X.2012.05391.x.
- Nakamura, Y., 1989. A method for dynamic characteristics estimation of subsurface using microtremor on the ground surface. *Quarterly Report of the Railway Technical Research Institute* **30** (1), 25-30.
- Nogoshi M. & Igarashi T., 1971. On the amplitude characteristics of microtremor (part 2) (in Japanese with english abstract). *Journal of seismological Society of Japan*, **24**, 26-40.
- OGS (Istituto Nazionale di Oceanografia e di Geofisica Sperimentale) and University of Trieste (2002): North-East Italy Broadband Network. International Federation of Digital Seismograph Networks. Other/Seismic Network. doi:10.7914/SN/NI

- Peter, D., Komatitsch, Y., Luo, Y., Martin, R., Goff, N.L., Casarotti, E., Loher, P.L., Magnoni, F., Liu, Q., Blitz, C., Nissen-Meyer, T., Basini, P. & Tromp, J., 2011. Forward and adjoint simulations of seismic wave propagation on fully unstructured hexahedral meshes, *Geophys. J. Int.*, **186** 712-739.
- Picotti, V., and Pazzaglia, F.J., 2008. A new active tectonic model for the construction of the Northern Apennines mountain front near Bologna (Italy), *J. Geophys. Res.* 113, B8, doi:10.1029/2007JB005307.
- Pondrelli, S., A. Morelli, G. Ekström, S. Mazza, E. Boschi, and A. M. Dziewon-ski, 2002, European-Mediterranean regional centroid-moment tensors: 1997-2000, *Phys. Earth Planet. Int.*, 130, 71-101, 2002
- Pondrelli S., A. Morelli, and G. Ekström, European-Mediterranean Regional Cen-troid Moment Tensor catalog: solutions for years 2001 and 2002, *Phys. Earth Planet. Int.*, 145, 1-4, 127-147, 2004.
- Pondrelli, S., S. Salimbeni, G. Ekström, A. Morelli, P. Gasperini and G. Vannucci, The Italian CMT dataset from 1977 to the present, *Phys. Earth Planet. Int.*, doi:10.1016/j.pepi.2006.07.008, 159/3-4, pp. 286-303, 2006
- Pondrelli S., Salimbeni S., A. Morelli, G. Ekström and Boschi E., European-Mediterranean Regional Centroid Moment Tensor catalog: Solutions for years 2003 and 2004, *Phys. Earth Planet. Int.*, 164, 1-2, 90-112, 2007.
- Pondrelli S., Salimbeni S., Morelli A., Ekström G., Postpischl L., Vannucci G. and Boschi E., European-Mediterranean Regional Centroid Moment Tensor Catalog: solutions for 2005-2008, *Phys. Earth Planet. Int.*, 185(3), 74-81, 2011.
- Pondrelli S. and Salimbeni S., Regional Moment Tensor Review: An Example from the European Mediterranean Region. In *Encyclopedia of Earthquake En-gineering* (pp. 1-15), <http://link.springer.com/referenceworkentry/10.1007/978-3-642-36197-5-301-1>, Springer Berlin Heidelberg, 2015.
- Sambridge, M., 1999. Geophysical Inversion with a Neighbourhood Algorithm - Searching a parameter space, *Geophys. J. Int.*, 138 , 479-494.
- Saraò, A., and Peruzza, L., 2012. Fault-plane solutions from moment-tensor inver-sion and preliminary Coulomb stress analysis for the Emilia Plain, *Ann. Geophys.* 55, 4, doi:10.4401/ag-6134.
- Schivardi R., and A. Morelli, 2011, EPmantle: a three-dimensional transversely isotropic model of the upper mantle under the European Plate, *Geophys. J. Int.*, **185** 469-484, doi: 10.1111/j.1365-246X.2011.04953.x

- Serpelloni, E., Vannucci, G., Pondrelli, S., Argnani, A., Casula, G., Anzidei, M., Baldi, P., and Gasperini, P., 2007. Kinematics of the Western Africa-Eurasia plate boundary from focal mechanisms and GPS data, *Geophys. J. Int.* 169, 1180–1200, doi:10.1111/j.1365-246X.2007.03367.x.
- Stein, S. and Wysession, M.E., 2003. An introduction to seismology, earthquakes, and earth structure. Wiley Blackwell. ISBN 0-86542-078-5.
- Stich, D. & A., Morelli, 2007. Reflection of seismic surface waves at the northern Apennines, *Earth Planet. Sci. Let.*, **259**, 149, doi:10.1016/j.epsl.2007.04.036.
- Stich, D., P. Danecek, A. Morelli and J. Tromp, 2009. Imaging lateral heterogeneity in the northern Apennines from time reversal of reflected surface waves, *Geophys. J. Int.*, **177**, 543-554, doi: 10.1111/j.1365-246X.2008.04044.x
- Stupazzini, M., R. Paolucci and H. Igel, 2009. Near-fault earthquake ground-motion simulation in the Grenoble valley by a high-performance spectral element code, *Bull. Seism. Soc. Am.* 99 286–301.
- Tanimoto, T. & Rivera L., 2005. Prograde Rayleigh wave particle motion, *Geophys. J. Int.*, **162**, 399-405.
- Tanimoto, T. & Rivera L., 2008. The ZH ratio method for long-period seismic data: sensitivity kernels and observational techniques, *Geophys. J. Int.*, **172**, 187-198.
- Tarantola, A., 2005. Inverse Problem Theory and Model Parameter Estimation, SIAM, Philadelphia.
- University of Genova (1967): Regional Seismic Network of North Western Italy. International Federation of Digital Seismograph Networks. Other/Seismic Network. doi:10.7914/SN/GU
- Vannoli, P., Burrato, P. and Valensise, G., 2015. The Seismotectonics of the Po Plain (Northern Italy): Tectonic Diversity in a Blind Faulting Domain. *Pure and applied geophysics*. 172, 1105-1142. doi: 10.1007/s00024-014-0873-0
- Verbeke, J., L. Boschi, L. Stehly, E. Kissling, and A. Michelini, 2012. High-resolution Rayleigh-wave velocity maps of central Europe from a dense ambient noise dataset, *Geophys. J. Int.*, 188(3), 1173–1187.
- Wagner, M., E. Kissling, and S. Husen, 2012. Combining controlled-source seismology and local earthquake tomography to derive a 3-D crustal model of the western Alpine region, *Geophys. J. Int.*, 191(2), 789–802.

Wathelet, M., D. Jongmans, M. Ohrnberger, and S. Bonnefoy-Claudet, 2008. Array performances for ambient vibrations on a shallow structure and consequences over Vs inversion. *Journal of Seismology*, **12**, 1-19.

Weber, J., Vrabec, M., Pavlovčič-Preseren, P., Dixon, T., Jiang, Y., and Stopar, B., 2010. GPS derived motion of the Adriatic microplate from Istria Peninsula and Po Plain sites, and geodynamic implications, *Tectonophysics* 483, 213–222, doi:10.1016/j.tecto.2009.09.001.

Woodhouse, J.H., 1974., Surface waves in a laterally varying layered structure, *Geophys. J.R. Astron. Soc.*, **37**, 461-490.

Yano, T., Tanimoto, T. & Rivera, L., 2009. The ZH ratio method for long-period seismic data: inversion for S-wave velocity structure, *Geophys. J. Int.*, **179**, 413-424.